



**HAL**  
open science

# Development of quantitative methods for the following of tumoral angiogenesis with dynamic contrast-enhanced ultrasound

Guillaume Barrois

► **To cite this version:**

Guillaume Barrois. Development of quantitative methods for the following of tumoral angiogenesis with dynamic contrast-enhanced ultrasound. Bioinformatics [q-bio.QM]. Université Pierre et Marie Curie - Paris VI, 2014. English. NNT : 2014PA066180 . tel-01079943

**HAL Id: tel-01079943**

**<https://theses.hal.science/tel-01079943>**

Submitted on 4 Nov 2014

**HAL** is a multi-disciplinary open access archive for the deposit and dissemination of scientific research documents, whether they are published or not. The documents may come from teaching and research institutions in France or abroad, or from public or private research centers.

L'archive ouverte pluridisciplinaire **HAL**, est destinée au dépôt et à la diffusion de documents scientifiques de niveau recherche, publiés ou non, émanant des établissements d'enseignement et de recherche français ou étrangers, des laboratoires publics ou privés.



THÈSE DE DOCTORAT DE L'UNIVERSITÉ PIERRE ET MARIE CURIE

Spécialité

**Informatique Biomédical - Imagerie Biomédicale**

École doctorale Pierre Louis de santé publique à Paris : Épidémiologie et Science de l'Information  
Biomédicale

Présentée par

**Guillaume BARROIS**

Pour obtenir le grade de

**DOCTEUR de l'UNIVERSITÉ PIERRE ET MARIE CURIE**

Sujet de la thèse:

---

**Development of quantitative methods for the  
following of tumoral angiogenesis with dynamic  
contrast-enhanced ultrasound**

---

Soutenue le 30 Septembre 2014 devant le jury composé de :

M. Christian CACHARD	Rapporteur
M. Massimo MISCHI	Rapporteur
Mme. Severine DUBUISSON	Examineur
M. Robert ECKERSLEY	Examineur
M. Alain CORON	Examineur
Mme. Lori BRIDAL	Directeur de thèse

Laboratoire d'imagerie biomédicale  
15 rue de l'école de médecine  
75006 Paris

UPMC  
École doctorale Pierre Louis de santé  
publique à Paris : Epidémiologie et Science  
de l'Information Biomédicale  
15 rue de l'école de médecine  
75006 Paris

# Summary

Dynamic contrast-enhanced ultrasound (DCE-US) is an imaging modality used in clinical and pre-clinical studies to evaluate the functional flow in a tissue using an ultrasonic contrast agent made of coated microbubbles. Because the microbubbles have a strictly intravascular distribution and a non-linear response to ultrasound, sequences imaging the passage of the contrast agent in the tissue can provide information about functional microvascular flow.

The aim of this work was to develop new methods to achieve a more robust, in vivo evaluation of the functional flow within the tumor vascular network with DCE-US. Three specific aspects of data analysis were addressed: 1) insuring best fit between parametric flow models and the experimentally acquired contrast-enhanced echo-power curves, 2) compensating sequences for movement occurring during data acquisition and 3) evaluating a new method to discriminate between tissues with different functional flow.

A multiplicative model is proposed to better describe the dynamic contrast-enhanced ultrasound signal. Based on this multiplicative model, a new parametric regression method of the signal is derived. Characterization of the statistical properties of the noise and signal is also used to develop a new method simulating contrast-enhanced ultrasound 2D+t sequences. The signal samples (or pixels) in these simulations present spatial correlation and statistical distribution properties that well approximate those in experimentally-acquired contrast image sequences. A significant decrease (between 25 and 60%,  $p < 0.05$ ) in the variability of the functional flow parameters extracted according to the new multiplicative-noise fitting method is demonstrated using both simulated and experimentally-acquired sequences.

The new sequence simulations are then applied to test a method combining motion estimation and flow-parameter estimation within a single mathematical framework. Because this new method does not require the selection of a reference image, it reduces operator intervention. Tests of the method on both simulations and clinical data and demonstrate significantly in a majority of sequences a more accurate motion estimation than the commonly used, mutual-information-based image registration method.

Finally, a non-parametric method, developed by Yves Rozenholc, for perfusion curve clustering is evaluated on 2D+t sequences. The aim of this method is to regroup similar filling patterns without a priori knowledge about the patterns. The method is tested on simulated and on pre-clinical data.

The methods developed improve robustness of DCE-US evaluations through more rigorous signal analysis, reduction of operator-dependent intervention and consideration of the spatial heterogeneity of microvascular flow patterns. In the future, effect such as attenuation could be also considered and these methods could also be applied to other ultrasound imaging configurations such as targeted DCE-US or 3D+t sequences.

# List of publications and communications

## Publications

- **Guillaume Barrois**, Alain Coron, and Lori Bridal. Simulation of dynamic contrast-enhanced ultrasound sequences using example-based texture generation. *IRBM*, Accepted in May 2014.
- **Guillaume Barrois**, Alain Coron, Thomas Payen, Alexandre Dizeux, and Lori Bridal. A multiplicative model for improving microvascular flow estimation in dynamic contrast-enhanced ultrasound (DCE-US): theory and experimental validation. *IEEE transactions on ultrasonics, ferro-electrics, and frequency control*, 60(11):2284–94, November 2013.
- Nizar Bouhleh, Alain Coron, **Guillaume Barrois**, Olivier Lucidarme, and Lori Bridal. Dual-mode registration of dynamic contrast-enhanced ultrasound combining tissue and contrast sequences. *Ultrasonics*, pages 1–11, January 2014.

## Communications

### Oral presentation

- **Guillaume Barrois**, Alain Coron, Thomas Payen, Alexandre Dizeux, and Lori Bridal (2013). A multiplicative model to improve microvascular flow evaluation in the context of dynamic contrast-enhanced ultrasound (DCE-US). *IEEE International Symposium on Biomedical Imaging, April 2013, San Francisco, USA. Proceeding available*

### Poster presentations

- **Guillaume Barrois**, Alain Coron, and Lori Bridal. New reference-free, simultaneous motion-correction and quantification in dynamic contrast-enhanced ultrasound. *IEEE International Ultrasonic Symposium, September 2014, Chicago, USA*.
- **Guillaume Barrois**, Alain Coron, and Lori Bridal. Detection of early therapeutic response with dynamic contrast enhanced ultrasound (DCE-US) using a perfusion clustering algorithm. *IEEE International Ultrasonic Symposium, September 2014, Chicago, USA*.

- Michele Lamuraglia, **Guillaume Barrois**, Mathieu Santin, Delphine Le Guillou Buffelo, Lori Bridal, Olivier Lucidarme. Dynamic Contrast-Enhanced Ultrasound Monitoring of Tumor Perfusion in a Murine Pancreatic Tumor Model to Assess the Effect of (Ziv)-Aflibercept and Sorafenib, Two Anti-angiogenic Drugs *American Association for Cancer Research Annual Meeting, April 2013, Washington, USA*.
- **Guillaume Barrois**, Alain Coron, Thomas Payen, Alexandre Dizeux, and Lori Bridal. Une nouvelle modélisation du signal en imagerie de contraste ultrasonore conduisant à une meilleure estimation des paramètres de microvascularisation *Scientific Days of the New in vivo Imaging Methods, December 2012, Lyon, France*.
- Alexandre Dizeux, **Guillaume Barrois**, Thomas Payen, Capucine Baldini, Delphine Le Guillou Buffelo, Eva Comperat and Lori Bridal. Differentiation of vascular distribution and flow patterns in tumors with Dynamic Contrast-Enhanced Ultrasound (DCE-US) perfusion maps *IEEE International Ultrasonic Symposium, October 2012, Dresde, Germany*.

# Notations

Recurrent notations:

- Region of interest : ROI
- Region of analysis : ROA
- Transit time distribution probability density function:  $Tr(t)$
- Transit time distribution cumulative density function:  $Tr_{cdf}(t)$
- Measured signal,contrast echo-power data curves :  $f(t)$
- Concentration :  $C(t)$
- Input function:  $I(t)$
- Echelon function :  $U(t)$
- Parametric model of signal :  $u(\theta, t)$
- Vector of parameters :  $\theta$
- Motion :  $T$
- Electronic noise :  $\epsilon$
- Speckle noise :  $v$

# Chapter 1

## Introduction

### 1.1 Context

With 355 354 cases and 148 378 deaths in 2012, cancer is one of the most prevalent diseases in France. It is the first cause of mortality [1], and is therefore a major concern in public health policy. Between 1980 and 2012, cancer incidence (assessed based on the number of new cases normalized with respect to the population) has increased by 39% while the mortality has decreased by 1.3% [2]. Several factors contribute in different ways to these figures. Improved therapeutic care, such as that due to advances in chemotherapy and the development of targeted therapy, has led to a decrease in mortality. At the same time, the development of better detection and monitoring tools has enabled earlier diagnosis and even, in some cases, overdiagnosis (detection of disease that will never cause symptoms or death).

In this context, medical imaging is an indispensable tool for radiologists. There is a need for medical imaging techniques that can go beyond the bounds used currently for diagnosis and therapeutic follow-up. Imaging techniques able to more precisely characterize the effect of treatments on tumors in pre-clinical or clinical studies could have a major impact both on cancer detection and on individualized therapy and drug development[3]. The development of imaging modalities able to capture subtle functional information in an accurate and robust way is, therefore, one of the essential elements in the fight against cancer.

#### 1.1.1 Therapeutic options

In France, patients are treated using three main types of therapy: radiotherapy (176 000 patients in 2011), chemotherapy (269 000 patients) and surgery (376 000 patients) [1]. Radiotherapy consists in irradiating tumours using X-rays to kill tumorous cells. However, the dose of ionizing radiation a patient can receive is limited, and radiotherapy can damage surrounding tissues. Moreover, radiotherapy is less effective when tumours are hypoxic because oxygen is an efficient radio-sensitizer [6]. Surgery consists in removing the tumour. Its main drawbacks are that it is highly invasive and often a source of anxiety for the patient. Moreover, some tumour sites are not surgically accessible, and surgery can miss cells or metastases that have spread from the primary tumour. Radiotherapy and surgery are efficient when the tumorous cells are localised in an identified part of the body. When they are dispersed, chemotherapy is typically applied in conjunction with radiotherapy or surgery to pursue tumorous cells that may have

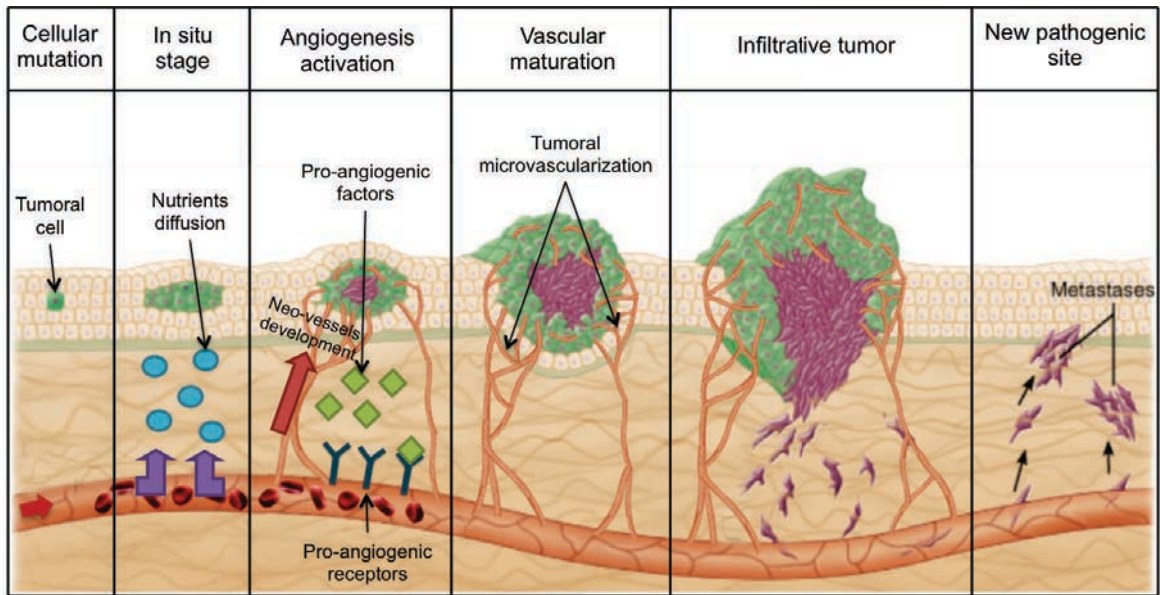


Figure 1.1: Illustration of the role of angiogenesis in tumoral development (adapted from Bergers and Benjamin [4])

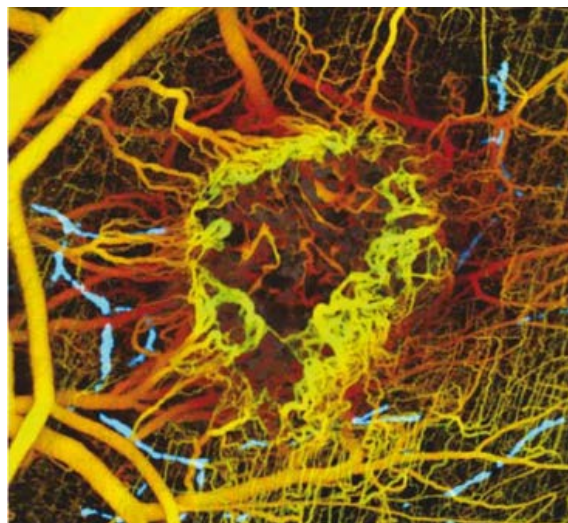


Figure 1.2: Image acquired using optical frequency domain imaging. At the center of the image, MCAIV tumor transplanted in the left hemisphere of a mouse brain (from Vakoc et al. [5]).

spread throughout the body. It consists in the administration of cytotoxic molecules through the vascular network to kill the tumorous cells. However, during chemotherapy, toxicity to healthy tissues also occurs and tumours can develop resistance to the therapeutic effects.

More recently, anti-angiogenic and antivascular drugs have been developed to target the vascular system that develops to support tumors. Angiogenesis is the process by which tissues create new vessels from pre-existing ones in order to provide their metabolism with enough nutrients and oxygen. Angiogenesis plays a major role in tumour growth beyond a few millimetres and to metastatic dissemination ([7], Figure 1.1). Tumours induce a shift in the balance between pro and anti-angiogenic factors in tumoural angiogenesis which leads to a disorganised growth of the vessels surrounding the tumour. Figure 1.2 illustrates the heterogeneous and chaotic characteristics of the tumoural vascularization.

Because angiogenesis is critical for tumour development, therapies capable of regulating it have been the subject of growing interest. Anti-angiogenic therapies have been shown to lead to a reduction of tumoural blood flow [8, 9, 10]. The chaotic characteristics of the tumoural vascular network are also believed to prevent efficient targeting of the tumour with cytotoxic therapies [11]. New therapeutic strategies have entered trials to investigate use of anti-angiogenic in conjunction with chemotherapy to normalize the tumour vasculature and to enhance delivery of cytotoxic molecules [12]. However, due to the very large number of pro and anti-angiogenic pathways, patients can develop resistance to anti-angiogenic therapy, by bypassing the targeted pathway [13]. Indicators of the microvascular network structure of the tumour can play a central role to evaluate more precisely the effects of anti-angiogenic therapies on the vascular network and to detect the development of drug resistance.

### 1.1.2 Role of detection and monitoring techniques

Each therapeutic option has specific targets, limitations and undesirable side effects. Therefore, therapeutic choice must be based on accurate diagnosis and sensitive monitoring to guard against inefficient or unnecessary therapy. Tumour monitoring and characterization can also play a central role in therapy development. Pre-clinical studies which aim at appreciating the efficiency of a new drug also require accurate tumour characterization and monitoring techniques. Imaging methods able to detect early response (or non-response) to therapy can provide early stage end-points for pre-clinical evaluations of new drugs. This could both accelerate drug development and reduce its cost. Accurate characterization and monitoring requires techniques able to assess morphological, molecular or functional indicators specific and predictive of tumour state.

### 1.1.3 Indexes used to follow cancer therapy

#### Morphological

Morphological indicators are widely used in clinical practice. Tumour size has been shown to be an indicator of the tumour's therapeutic sensitivity [14] or of the metastasis probability [15]. The current clinical standard for the evaluation of cancer therapy is based on a set of recommendations toward classification of a tumor as "stable", "in regression" or 'in progression", known as the RECIST criteria [16]. However, by definition, these criteria do not provide information about the functional state of a tumor. For instance according to this criteria, a tumour with a large necrotic core would be assessed to

be of equal risk as a highly vascularized tumor of the same size.

### **Molecular**

Because tumour growth or functional modifications lead to the release of specific molecules, being able to follow the evolution of the concentration of those molecules can provide valuable information about the type, the stage or the grade of the disease [17]. The development of new technologies that are able to simultaneously assess the concentration of thousands proteins has permitted great progresses in diagnosis and tumour classifications [18].

### **Functional**

Functional indicators provide information about the physiological activity of the tumour and can therefore allow a more precise monitoring of cancer. In particular, microvascularization is a good index for the assessment of tumour angiogenesis. Microvascularization designates the blood circulation in capillaries having diameters between 5 and 25  $\mu\text{m}$ . The velocity of blood in capillaries is on the order of 0.7 mm/s [19]. Doppler ultrasound can provide information about the flow speed and direction, however its resolution is limited to vessels with a size greater than 200  $\mu\text{m}$  [20]. Developments such as Power Doppler or, more recently, ultrafast Doppler [21] have significantly improved the resolution down to approximately 100  $\mu\text{m}$ , but the resolution is still too low to fully assess the microvascular structure in tumours. Because contrast agent uptake in a microvascular network can provide functional information about the microvascular flow, dynamic contrast-enhanced (DCE) imaging modalities, where a contrast agent enhancing signal is injected in the vascular network of the patient, have been used to follow tumoral angiogenesis [22, 23, 24]. The choice of the imaging modality between DCE-MRI, DCE-CT and DCE-US is made according to the location of the tumour, its characteristics, and the information to retrieve. Compared to the other modalities, DCE-US presents several advantages: it is a non-toxic modality, that can be brought directly to the patient, with a relatively low cost. Moreover, ultrasound contrast agent is strictly intravascular which allows to investigate tumours vascular bed with model that are simpler than in MRI or CT.

## **1.2 Dynamic contrast-enhanced ultrasound**

### **1.2.1 Ultrasound contrast agent**

Ultrasonic contrast agents are microbubbles of gas, encapsulated in a lipidic or another type of coating. The gas used in the first, commercially available contrast agents was air (for instance Echovist<sup>®</sup> from Bayer or Albunex<sup>®</sup> from Molecular Biosystems), but this formulation has been progressively replaced by gasses that are less soluble in plasma such as perfluorocarbons (PFCs), to improve their stability in blood. Microbubbles coatings (e.g. albumin, phospholipids) have been developed to make microbubbles more resistant and increase their circulatory lifetime [25].

More recently, targeted microbubbles have emerged [26]: the surface of these microbubbles is linked to peptides or ligands that specifically associate with the targeted biomolecules. Therefore, they attach at sites where the targeted-molecule is expressed.

Because of the difference in density between their gaseous core and blood, microbubbles have a high compressibility. This, coupled with their capacity for asymmetric oscillation in the acoustic field, confer

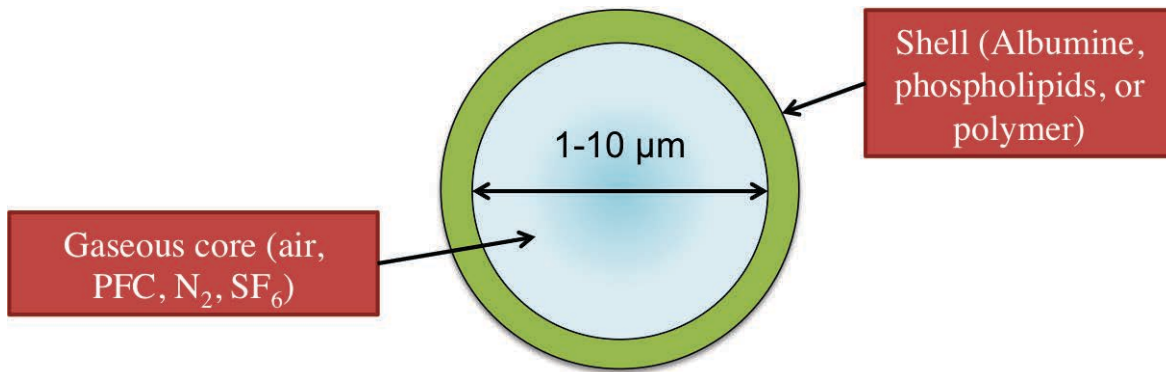


Figure 1.3: Schematic diagram of a microbubbles and of its structure.

to microbubbles a strong and specific non-linear acoustic response [27, 28]. This non-linear response can be exploited to enhance contrast of vessels relative to the surrounding tissues using specific ultrasound sequences. Their sub-micrometric size gives them a resonance frequency in the range of frequencies used in medical ultrasonics (1-10 MHz).

The small size of microbubbles also provides them with the ability to circulate in the whole vascular and microvascular network, while remaining strictly intravascular (as opposed to CT or MRI contrast agents that extravasate). Due to this, DCE-US can be used as blood flow tracers to evaluate the vascular volume and microvascular flow. To reliably make such evaluations with ultrasound contrast agents, specifically adapted data acquisition techniques are necessary.

### Contrast ultrasound image formation

In classical B-mode imaging, the envelope of the received pulses (RF signal) is computed and used to form an image. In DCE-US imaging, contrast sequences exploiting the strong non-linear component of the microbubbles' acoustic responses have been developed to improve contrast between the microvascular network and other tissues. In particular, harmonic imaging, aiming at forming an image with the backscattered signal at  $2f$  when the transmitted signal has a fundamental frequency of  $f$ , have been highly popular in DCE-US due to strong non-linear response of microbubbles. Several harmonic imaging sequences have been proposed, consisting in emitting several pulses with different characteristics and then processing the received echoes to predominately retain harmonic components due to the microbubble response. The first and most common sequence is pulse inversion [29]. It consists in summing the response to two out-of-phase pulses to suppress echoes from linear scattering structures. Other techniques such as contrast pulse sequence (CPS) [30], exploit phase and amplitude modulation to extract the non-linear component of the returning echoes. Beside harmonic imaging, sub-harmonic imaging has also been proposed to improve detection of microbubbles using their unique sub-harmonic response [31]. It presents the advantage to allow a better suppression of the surrounding tissue than harmonic imaging [32], because sub-harmonic response of tissue is generally a lot weaker than their harmonic response. All these technique aim at suppressing signal components that do not come from microbubbles. After non-linear signal processing has been applied to detect the microbubble response, this signal must be processed to form an image.

### 1.3 Objectives of this thesis

Angiogenesis plays a key role in tumour development. DCE-US can potentially be used to follow modifications in the microenvironment and the microvascular network of tumour during development and therapy. However, the capacity of DCE-US to fulfil this potential is still limited by several factors. Variability in DCE-US data due to factors such as injection profile, image-plane selection or physiological variations limits the repeatability of measurements. The development of repeatable *in vivo* acquisition protocols and of robust and easy-to-interpret biomarkers are, therefore, keys to make DCE-US more efficient and more widely applicable in pre-clinical and clinical studies. This thesis is focused on a better characterization of the quantification process in DCE-US, and the development of new processing techniques based on this characterization. By developing better techniques for the analysis of DCE-US sequences, a more precise and accurate indication of microvascular flow modifications during therapy will be achieved.

In Chapter 2, the microvascular flow quantification process using DCE-US is described in detail using a linear system formalism. Each step that composes the process is identified, examples from the literature showing the state of the art for each step in the DCE-US quantification process are described. The sources of variability in the process are highlighted so that they can better be addressed in the subsequent chapters of this thesis.

## Chapter 2

# Linear system formalism for flow quantification using dynamic contrast-enhanced ultrasound

### 2.1 Overview of flow quantification in DCE-US

As presented in the introduction, the aim of flow quantification techniques in the context of angiogenesis monitoring is to follow modifications of the microvascular network of a tumour, in order to evaluate and quantify its response to therapy. This vascular network can be locally characterized by its transit time distribution  $Tr_x(t)$  in a region of analysis (ROA)  $x$ , or its cumulative density function  $Tr_{x,cdf}(t)$ . The transit time designates the time the contrast agent stays in the ROA which is a quantity of clinical interest because it is related to the tortuousness of the vascular network, its homogeneity and its density [33]. The ROA designates the area from which the signal to analyse is extracted. ROAs are included in the region of interest (ROI), which is the area of interest for angiogenesis monitoring (typically drawn around the whole tumour). Flow quantification techniques using contrast-enhanced imaging aim to provide quantitative flow parameters that correlate with the properties of  $Tr_x(t)$ . However, those flow parameters are estimated via an imaging process made of several steps which introduce sources of variability.

Figure 2.1 schematically summarizes the succession of steps (represented by boxes) for the process of flow quantification using DCE-US: from the contrast agent injection to the extraction of quantitative flow parameters. The input and output at each step are represented by arrows while the parameters and the external conditions that effect each step are described above each box. In the following sections of this chapter, a general formalism using linear systems is proposed to model flow quantification using DCE-US. The important steps of flow quantification are then explained based on this formalism to better identify the sources of variability. The main approaches that have been proposed in the literature to reduce parameter estimation variability are summarized in each section.

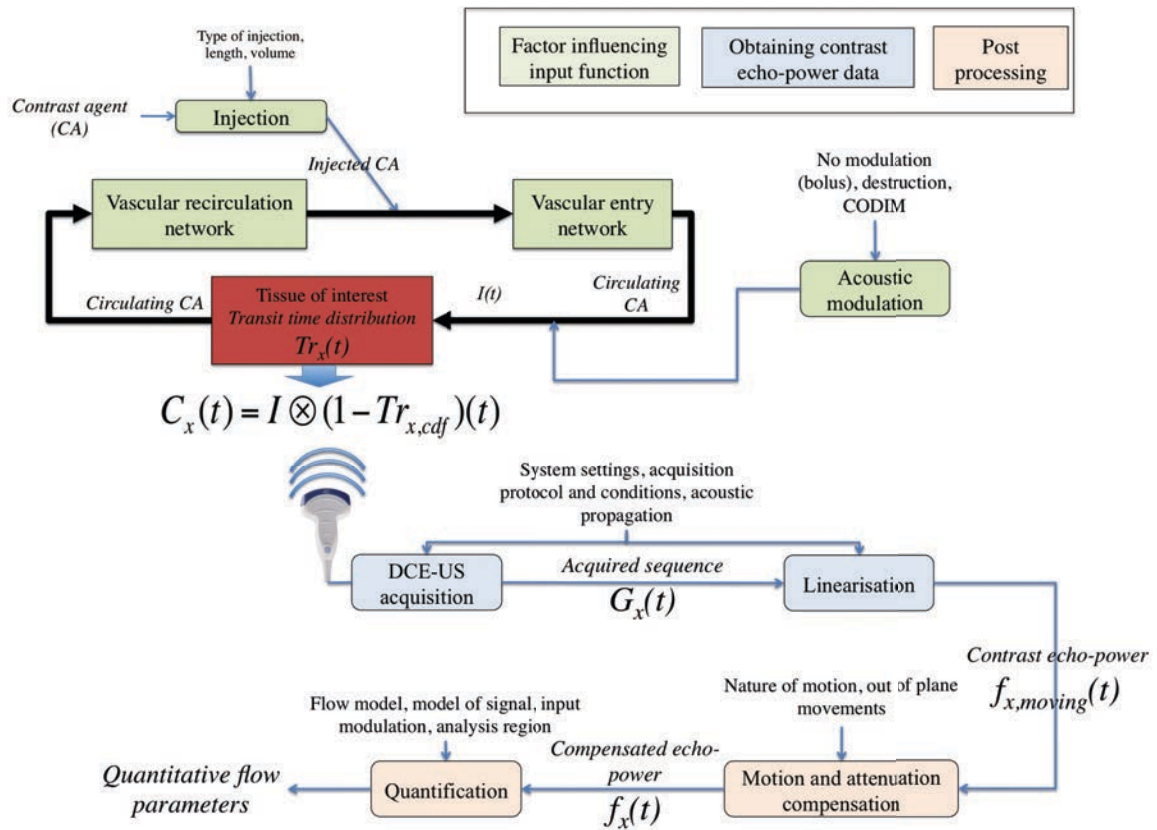


Figure 2.1: Schematic diagram of the main steps of flow quantification in a given tissue using DCE-US. Blue arrows represent input and output, boxes represent processing, and quantities above boxes are parameters or external elements that effect the processing.

## 2.2 Linear system formalism relating microvascular flow to DCE-US data analysis

The linear system formalism is a widely used formalism to describe electronic circuits or mechanical systems. It has also been used in the development of quantification techniques for imaging modalities such as Dynamic Contrast-Enhanced Magnetic Resonance Imaging (DCE-MRI) and Computed Tomography (DCE-CT). Linear system formalism offers a useful approach to describe and better understand the influence of individual steps in a quantification process on the measured output. However, only a few groups developing deconvolution methods have applied it to the problem of quantification in DCE-US[34, 35, 36].

Mathematically, a linear time-invariant system satisfies the properties of superposition and scaling [37]. Under these conditions, the output of the system  $f(t)$  can be calculated as the convolution of an input function  $I(t)$  with the impulse response of the system  $h(t)$ :

$$f(t) = \int_0^t I(t - \tau)h(\tau)d\tau = I * h(t) \quad (2.1)$$

In the context of DCE-US, the input function  $I(t)$  represents the concentration of contrast agent that arrives in the ROA at a time  $t$ .  $h_x(t)$  is the impulse response of the microvascular network in the ROA around position  $x$ . It is related to the transit time of the contrast agent in the analysis region:  $h_x(t)$  represents the proportion of contrast agent that stays, at most,  $t$  seconds in the analysis region. Therefore,  $h(0) = 1$  and  $h(\infty) = 0$ . This function is related to the cumulative density function of the transit time distribution  $h_x(t) = 1 - Tr_{x,cdf}(t)$ . The output function  $f(t)$  is the function  $C_x(t)$ , which represents the concentration of contrast agent in the ROA centered on  $x$  at time  $t$ .

The function  $C_x(t)$  is never directly measured: it is evaluated via the signal  $f_x(t)$  acquired using an imaging modality. The relationship between  $f_x(t)$  and  $C_x(t)$  depends on the modality, the imaging conditions and the acoustic properties of the imaged medium (e.g. scattering cross section, attenuation in the medium). In DCE-US, one fundamental assumption is that the relationship between contrast agent concentration and average, measured contrast echo-power can be considered linear throughout a certain range of agent concentrations. Beyond an agent and system-dependent threshold, this relationship no longer holds and  $f_x(t)$  remains constant as the contrast concentration increases [38, 39], and can even decrease due to multiple scattering and attenuation effects from contrast agent microbubbles. Within the range of concentrations commonly used when quantifying DCE-US, it can be assumed that the expected value of  $f_x(t)$  follows the relationship:

$$E[f_x(t)] = aC_x(t) + f_{x0} \quad (2.2)$$

with  $a$  a constant and  $f_{x0}$  the level of signal without contrast agent. This linear relationship between signal and concentration can only be written via the expected value of the signal: random processes make the direct relationship between  $f_x$  et  $C_x$  non-deterministic.

## 2.3 Factors influencing the input function

### 2.3.1 Injection

Because it has a strong influence on  $I(t)$  in Eq. (2.1), the injection of contrast agent is an important source of variability for DCE-US, in particular for bolus injection. Injections are generally performed manually.

To give an order of magnitude of the variations introduced by the injection phase, Dizeux et al. estimated the coefficients of variation (CV) for flow parameters assessed in an *in vitro* flow phantom and in the renal cortex of mice for manual and controlled-injections. Lognormal curves fits to data from seven repeated *in vitro* injections are presented in Figure 2.2. Manual vs controlled injection CVs were 79% and 40%, respectively, for mean transit time (MTT) and 13% and 10% for peak enhancement (PE) assessed in the renal cortex of mice<sup>1</sup>. These results demonstrate that injection of the contrast agent is an important part of the DCE-US imaging process and that it contributes to its variability, in particular, when no modulation of the entry function is performed after the injection.

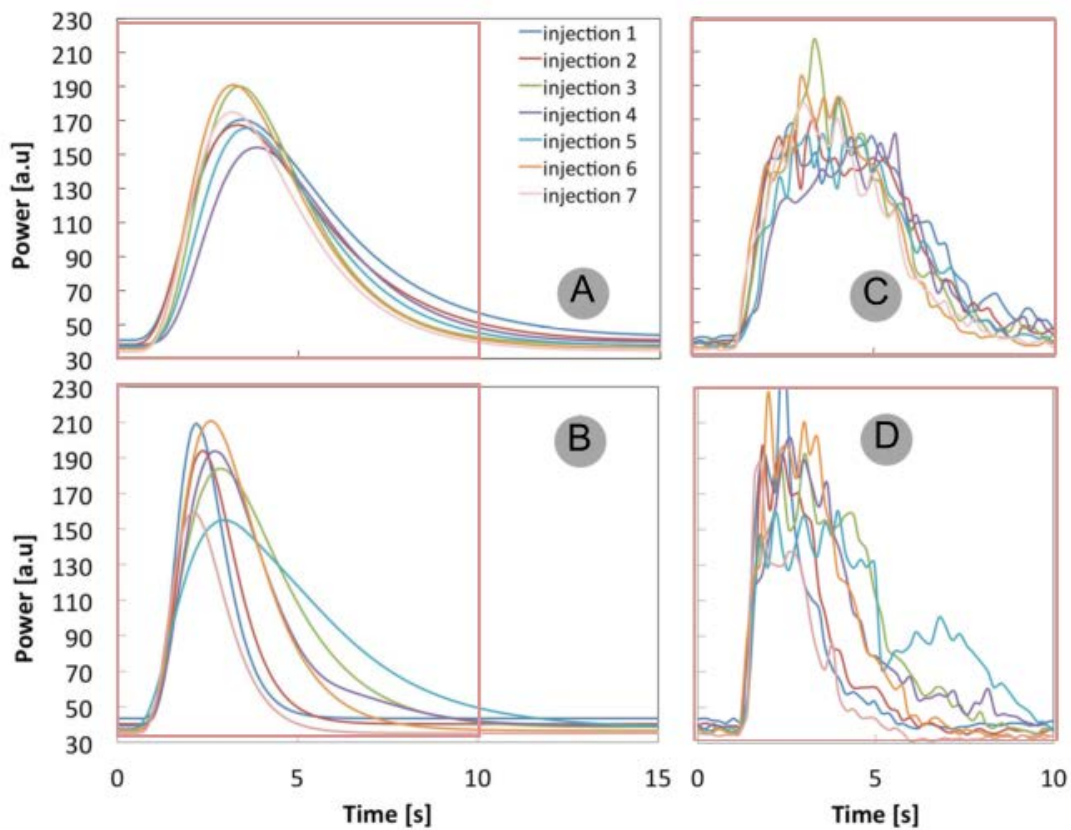


Figure 2.2: (A, B) - Fitted curves from experimentally acquired data using a lognormal model obtained from *in vitro* experiments using, respectively, controlled injection and manual injection. (C, D) - Unprocessed data (from Dizeux et al. [40])

<sup>1</sup>The flow parameters, MTT and PE, are described in detail in Section 2.5.6

### 2.3.2 Input function modulation

After injection, contrast agent flows through the vascular network and through different tissues until it reaches the tissue of interest. The shape of the bolus concentration vs. time curve describing the arrival of microbubbles in the ROA, characterizes the function  $I(t)$ . In the case of bolus injection, the agent concentration entering the tissue of interest is unknown and influenced by both injection variability and the tissues it has traversed before reaching the tissue of interest. It is generally assumed that the input function is identical for the entire analysis region. This is a strong hypothesis that is probably quite far from the reality. However, in the absence of 3D data acquisition, it cannot be more precisely characterized.

Microbubbles respond to moderate ultrasonic excitation by oscillating, but when the mechanical index of ultrasound pulses is strong enough, it can lead to the rupture of the microbubble shell and to partial or total destruction of the contrast agent microbubbles. This property can, therefore, be used to locally modulate the input function  $I(t)$ .

The destruction-replenishment (DR) method, proposed for the first time in [41] uses this property. It consists in destroying the contrast agent using a series of high MI pulses and observing the kinetics of the replenishment to extract flow parameters. Mathematically, if the destruction is total and if the imaged plane is the same as the destruction plane, this is equivalent to having a step function as an input  $I(t) = U(t)$ . In the framework of Eq (2.1), this means that  $C_x(t) = \int_0^t h(\tau)d\tau$ :  $C_x$  is the integral over time of  $h_x(t)$ . However, studies [42] have demonstrated that this is only an approximation, because the beam profile does not act like a step but rather as a Gaussian-shaped function. The DR approach can nonetheless decrease the variability of the input function by reducing the influence of the vascular entry network. In order to limit the destruction of contrast agent due to the imaging pulse, intermittent imaging technique have been proposed in conjunction with DR method [43, 44]. It consists in decreasing the imaging frame rate to decrease the exposure of microbubbles to ultrasound.

Another method known as contrast depletion burst imaging (CODIM) was proposed in 2002 by Eyding et al. [45]. It is based on successive insonations of the contrast agent which lead to partial destruction of the contrast agent. The concentration decreases until an equilibrium is reached between the partial destruction and the region refill by the wash-in of new microbubbles. This technique offers higher SNR than the DR technique. The fitting of an adapted parametric model allows estimation of the flow rate in the tissue.

Recently, a method that combines bolus injection and destruction replenishment has been proposed by Jirik et al. [36]. It consists in imaging the passage of the bolus of contrast agent followed by a destruction with a high mechanical index pulse. Because with DR, the input function  $I(t)$  is assumed to be known, it can improve the deconvolution of  $C_x(t)$  to the bolus input. Mathematically, this is equivalent to having, in the same echo-power data curve, the response of the vascular network (characterized by its impulse response  $h(t)$ ) to an unknown bolus input injection  $I_{bolus}(t)$  and to a destruction-replenishment input ( $I(t) = U(t)$ ).

All the techniques presented above aim to estimate flow parameters with the least possible dependence on the injection function and the vascular entry network. Each method for acoustic modulation of the input function has advantages and limitations. The destruction replenishment method leads to a response that is approximately the integral of the impulse function  $h_x(t)$ . This integration acts like a low pass

filter on the data and leads to a loss of temporal resolution. The DR approach is thus well adapted for the estimation of parameters related to the total quantity of microbubbles flowing through the ROA but is less efficient for estimation of parameters related to the flow dynamics. The same is also true for CODIM. Additionally, when using the CODIM approach, depth and region-dependent attenuation can make it difficult to optimize the MI so that the equilibrium level between microbubble destruction and refill is reached on a time-scale allowing sensitive evaluation of the flow. Finally, the technique developed by Jirik et al. is promising but requires a complex acquisition protocol and processing.

## 2.4 Obtaining contrast echo-power data

### 2.4.1 Imaging settings

Once the contrast agent has been injected and, if required by the selected contrast-imaging method, the input function has been acoustically modulated, the microbubbles arrive in the imaging plane according to the input function  $I(t)$ . The image acquisition phase consists in acquiring a set of signals  $G_x(t)$  in the region of analysis  $x$ .

Because microbubbles are sensitive to acoustic destruction, the mechanical index must be set to a relatively low value (generally between 0.02 and 0.25) in order to minimize microbubble destruction. Because even at low MI some microbubbles are destroyed by the insonification used to acquire each imaged frame, a compromise has to be found between frame rate and microbubble destruction. Frame rate is typically set to values between 2 and 10 Hz, depending on the tissue to image. The destruction of microbubbles resulting from imaging is generally neglected, except when using the CODIM approach which is based on acoustic destruction of some percent of the contrast microbubbles. The center frequency of the acoustic pulse is chosen based on the contrast agent and ultrasonic transducer used as well as the spatial resolution required for the examination. It is typically between between 1.5 MHz to 7 MHz.

Gauthier et al. [46] and Stride et al. [47] studied the effect of several scanner settings (acoustic gain, mechanical index, focal depth, acoustic pulse center frequency) on the extracted values of flow parameters. They demonstrated that scanner settings significantly effect estimated parameter values. To minimize variability in estimations from these effects, image settings are kept as fixed as possible in DCE-US studies.

### 2.4.2 Extraction of linear echo-power from images or radio-frequency data

To extract information from DCE-US data about the vascular network, it is necessary to know the nature of the relationship between the image intensity and the concentration in contrast agent. As explained in Section 2.2, there is an assumed linear relationship between concentration and contrast echo-power throughout the range of concentrations encountered in diagnostic contrast-ultrasonography. However, echo-power  $f_x(t)$  must be recovered from the information recorded by the imaging system. Several cases can be encountered, depending on the operating context.

When the ultrasound imaging system provides access to the radio frequency (RF) data, the contrast echo-power can be directly estimated. Some imaging-system manufacturers provide access, via a proprietary software, to a "DICOM Raw data" format that has undergone fewer display processing steps than the images displayed on the imaging system screen (spatial interpolation, application of a colormap...)

[48, 49]. Moreover, this format presents the advantage to be represented with a number of bits which is higher than the number of bits used to represent false color images displayed by the ultrasound imaging systems. However, this format is not available with all ultrasonic imaging systems, and it requires the use of specific software that may not be sufficiently flexible for specific applications in terms of the selection of regions of interest and analysis models [50].

Finally, when only compressed-video images in JPEG files (DICOM JPEG) are available, algorithms to approximate contrast echo-power from JPEG pixels intensity must be used. Recent publications [50] and software have demonstrated techniques to estimate contrast echo-power from pixel intensity and the limits for the validity of such estimations.

## 2.5 Post-processing

### 2.5.1 Attenuation compensation

Due to the physical nature of the ultrasonic waves and the properties of biological media, it is well known that ultrasonic imaging is effected by attenuation. This attenuation is typically compensated for image visualisation using Time Gain Compensation (TGC), but this technique assumes that the attenuation is only a function of depth.

In the case of harmonic imaging and in particular of DCE-US, more sophisticated methods need to be developed because time-variable microbubble concentrations and their nonlinear acoustic response can modify the temporal and frequency-dependent nature of the attenuation. Microbubble attenuation has been investigated and shown to be dependent on concentration, frequency, and acoustic pressure [47].

The presence of attenuation can affect the quantification. In practice, that means that the relationship between  $f_x(t)$  and  $C_x(t)$  in Eq(2.2) is not constant throughout the whole image. Attenuation can, therefore, modify the values of the flow parameters that are related to the amplitude of the signal. Attenuation compensation methods, taking into account non-linear attenuation, scattering [51] or local *in vivo* concentration of contrast agent [52] have therefore been proposed to address the specificities of attenuation in DCE-US.

### 2.5.2 Motion compensation

Motion is almost systematically present in acquired *in vivo* DCE-US sequences because of breathing, cardiac and probe motions. Fig. 2.3 shows echo-power data curves extracted from a ROA selected as the whole ROI delimiting a hepatocellular carcinoma selected on a sequence acquired *in vivo* in a human patient. Fig. (a) and (b) present images of the sequences between which the patients has moved. As a consequence in (b) the ROA does not correspond to the tumour any more. Fig. 2.3 (c) presents the echo-power data curves extracted from the ROAs with and without motion compensation and the corresponding lognormal flow-model fitting the curves. This example demonstrates how motion can introduce large variations in the echo-power data curves and significantly modify fitting. The practical importance of this in preclinical and clinical follow-up studies is significant. In the case it is not possible to robustly correct for motion, motion degrades the spatial resolution of the estimated flow and some sequences or ROAs have to be excluded from final analysis [74].

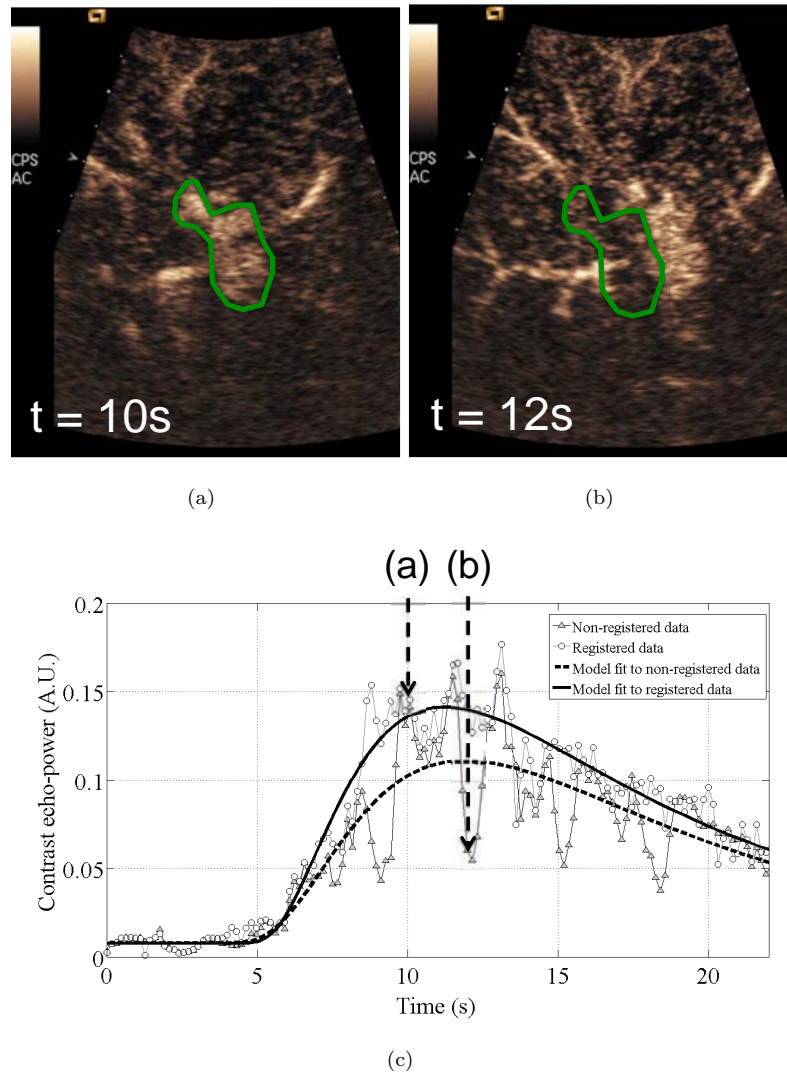


Figure 2.3: (a)-(b) DCE-US sequence acquired in a human hepatocellular carcinoma, at  $t=10\text{ s}$  and  $t=12\text{ s}$ . The ROA is marked in green. The patient clearly moved between the two images. (c) Echo-power data curves extracted from the green ROA with and without registration. A lognormal parametric flow model has been fit to each curve. The times at which images (a) and (b) have been extracted are indicated with arrows.

To limit the effects of motion on quantification, several approaches are possible. The simplest is to ask the patient to hold his breath during the exam. However, this can be problematic for acquisitions of more than 30 seconds, and it is not applicable in animal studies. It is also possible to select regions of interest that are far from the limit of the tissue and homogeneous. However, this limits the possibility of quantification in small lesions or peripheral zones.

Another strategy is to use gating techniques: this consists in selecting and estimating flow parameters only on frames where anatomical structures are located at the same position. Mule et al. [53] proposed an approach based on the analysis of local contrast echo-power variations and principle component analysis. With this approach, images in the sequence with the same phase of the breathing cycle were extracted to obtain a sub-set of images from approximately the same position. A more recent publication by Christofides et al. [54] proposed another gating approach: the position of the largest moving structure of the sequence was detected for each frame. An echo-power data curve could then be extracted from this structure, and the frequency corresponding to breathing was extracted from it. Again, only frames corresponding to the same breathing phase were used for final analysis. Gating methods are robust to out-of-plane motion and provide a rapid means to handle motion. However, because a large part of the sequence is discarded, these techniques lose information. Such loss can be problematic for observing brief phenomenon such as the initial arrival of contrast in the ROI. Moreover, these methods can fail if the motion is not cyclic or has other frequency components than those due to the breathing motion.

Another strategy is to use registration to compensate for motion in each image. Registration aims to align two images (the moving image and the reference image) by maximizing a similarity criteria between them. In addition to finding a robust and efficient similarity criterion, the challenge is to define the reference image with respect to which the whole sequence is to be registered. Due to the low contrast-to-noise ratio prior to contrast arrival and the lack of stable landmarks typical of harmonic imaging sequences, the problem is particularly difficult in DCE-US.

Current methods used in DCE-US realign the whole sequence with respect to a reference image defined by an operator. Different strategies have been used to compute the similarity metric. Rognin et al. [55] used a multiple mask strategy: the operator defines a delimitation mask around the region to be realigned and a feature mask that contains well-identified features of the organ. The metric is then computed and minimized over the intersection between these two masks. Zhang et al. [56] and Bouhleb et al. [57] computed a similarity criterion which combined information from harmonic contrast and B-mode images. The main drawbacks of existing methods is that they require operator-dependent selection of the reference image. In addition, any reference image chosen in a DCE-US sequence is unlikely to provide good representation for the entire sequence, because the distribution of intensity in the frame changes with the arrival of the contrast agent in the tissue.

### 2.5.3 Echo-power data curve processing

#### Parametric modelling

To recover microvascular flow information from the function  $f_x(t)$ , one approach, similar to some inverse problem resolution, is to replace the function  $C_x(t)$  by a model depending on a few parameters and to find the parameters that best fit the data  $f_x(t)$ . With a known kinetic-flow physical model for  $h_x(t)$ , the parameters obtained from the fitting phase give information about the blood flow in the imaged tissue.

The first parametric model proposed for analysis of DCE-US data was the perfect mixed chamber model. In this model, the tissue is considered as a single compartment in which the concentration in contrast agent becomes instantaneously homogeneous each moment that in-flow and out-flow modify the contrast concentration. This model has only been used with destruction replenishment modulation [58, 59, 60]. It leads to a mono-exponential equation describing the echo-power replenishment data curves, with two parameters: A the plateau and B the rise constant [41].

$$f(t) = A(1 - e^{-Bt}). \quad (2.3)$$

This instantaneous mixing chamber model does not imply the concept of transit.

A more advanced model for  $h_x(t)$  uses several homogeneous compartments (each one being a perfect mixing chamber)[61]. This leads to the Erlang probability density function, used early in DCE-MRI [62]. By relaxing the parameter of the model corresponding to the number of compartments, it corresponds to the gamma probability function. This was introduced in DCE-US by Thijssen et al. [63], for bolus injection analysis.

Other models consider the flow in the vessels directly, rather than modelling the vascular network using a chamber formalism. Krix et al. [64] proposed a model based on a 3D distribution of velocities and vessel flow angles. It assumes that the blood flow velocity is uniform. It can take into account heterogeneous blood velocity, but at the price of a rapidly increasing complexity. Arditi et al. [42] and later Hudson et al. [65] proposed a lognormal function to model the transit time distribution based on work by Karshafian et al. [33] describing transit time kinetics in vascular trees. This model is widely used in DCE-US studies, for both bolus and DR acquisitions [63, 66, 67, 68, 69].

Another approach, slightly different in spirit, is to model the movement of microbubbles as the combination of linear convection and longitudinal diffusion. This approach leads to the Local Random Walk (LDRW) model, which has been applied in several applications by Mischi et al. [70, 71]. By construction, this model can only be applied to bolus injection sequences.

It should be noted that in the case of a bolus entry function, most of the work cited in section 2.5.3 considers that the entry function  $I(t)$  can be approximated by a Dirac, and therefore that the function  $f(t)$  is the impulse response of the tissue. To avoid this assumption, some work has proposed the application of deconvolution techniques inspired from techniques developed for DCE-MRI that decorrelate  $f_x(t)$  and  $I(t)$ . This decorrelation is performed either by evaluating  $I(t)$  in a feeding vessel outside the ROI [34, 35] or by assessing the response in the ROA with several different input modulations [36].

### Non-parametric modelling

In addition to parametric flow models such as those presented in section 2.5.3, some authors prefer to extract perfusion parameters, from the echo-power data curve without fitting a parametric model to it. One approach consists in extracting the parameters directly from  $f_x(t)$ , without applying any processing to it [72, 73, 74]. Other authors first apply a low pass filter (generally a moving average) to the echo-power curve [75, 76]. The advantage of such methods is that there is no risk of poor fitting that could lead to misinterpretation of the data. On the other hand, extracted parameters are more variable because they are more sensitive to noise.

Among the other methods that do not use parametric modelling of the perfusion curves, techniques measuring the coherence or the correlation between neighbouring perfusion curves [71, 77] have been

proposed. Those techniques are particularly adapted for detection purpose, in order to highlight perfusion anomalies characteristics of cancerous tissues.

#### 2.5.4 Region of interest and region of analysis

When a DCE-US sequence is acquired, only a limited part of the frame is of clinical interest. This part is delimited by the ROI. In this ROI, signal from one or several ROAs is extracted and analysed in order to retrieve microvascular flow information. Ideally, if analysis can be obtained for sufficiently small ROAs, the local flow can be presented on parametric maps reflecting the heterogeneity of the tumours. However, because individual pixels in DCE-US present a high level of speckle noise, it may be necessary to average the signal over several pixels, to decrease the variance of the signal and make flow parameter extraction more robust. Another specific characteristic of DCE-US to keep in mind when drawing ROAs and ROIs is their anisotropic nature: due to the anisotropic nature of the ultrasonic image formation process, the axial and the transversal resolution of images are different, and the correlation profile is anisotropic (an illustration is given in [77] and in Chapter 4, Fig.4.3). Different ROI and ROAs selection strategies have been reported in the literature.

The first strategy is to select a unique ROA corresponding to the whole ROI, around the whole tumour, to obtain a highly averaged estimation of  $f_x(t)$  for each image frame [78, 79, 80]. The advantage of this approach is to improve the signal-to-noise ratio. However, an obvious drawback is that information may be lost in the case of heterogeneous tumours. Moreover, the larger is the analysis region, the more complex the transit time distribution can be. There is, therefore, a higher chance that the parametric model used to describe the signal cannot capture this complexity. Finally, as the size of the region of analysis increases, the validity of the hypothesis of a unique input function  $I(t)$  becomes more and more questionable.

Recently, authors have proposed the selection of several ROAs, to differentiate between perfused and non perfused regions of tumours. This may provide a more relevant characterization of the tumour microvascularization when necrotic or non perfused zones are present, but selection of the ROAs is highly operator-dependent.

Finally, extraction of local flow parameters from sub-millimetric ROAs can be done using either parametric flow models [69] or non-parametrically [71, 81]. Because the approach preserves spatial information, it is of great interest. However, it is much more sensitive to motion and noise than analysis from larger regions and, therefore, necessitates robust analysis techniques to handle a low signal-to-noise ratio.

#### 2.5.5 Fitting algorithms

When parametric models are used to analyse echo-power data curves, a fitting procedure must be applied to find the best parameters for the model. Surprisingly enough, despite its central role, this aspect of the quantification has received little attention in the literature.

In fact, the method used to fit the parametric model to the echo-power data curve is rarely specified in publications, and when it is, it is most often cited to be a least squares method [41, 45, 46, 48, 65, 69, 82]. Some authors such as Strouthos et al. [82] have reported use of a smoothing filter before fitting data, but the technique used for fitting remains least squares.

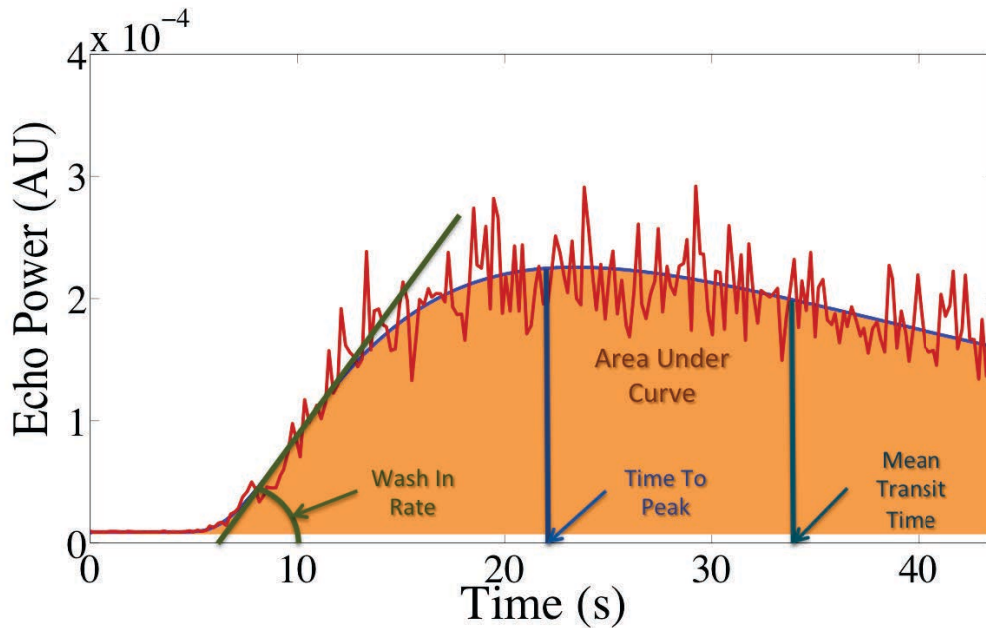


Figure 2.4: Illustration of the definition of WiR, AUC, TTP and MTT parameters for a bolus injection.

In [68], we examined the validity of the hypotheses that are made implicitly when using least squares for the analysis of DCE-US data and proposed a new model to better describe the noise and to design a more suitable fitting method. Kuenen et al. [83] also recently proposed a new method of fitting DCE-US data based on a derivation of maximum likelihood parameters. In their work, echo-power data curves were interpreted as transit time histograms, and maximum likelihood estimation was derived based on the parameters of the probability density function underlying these histograms.

### 2.5.6 Extracted flow parameters

A large number of quantitative parameters are extracted and studied in the contrast-enhanced imaging literature. Depending on the type of models chosen to describe the echo-power curves (parametric or non parametric), the parameters are estimated from the fit model or from pre-processed data curves. In this section, the most common parameters are described. In some cases, they can also be expressed very simply, directly from the model's parameters. It should be noted that most of these parameters depend on the definition of a time origin that must be chosen consistently between different data acquisitions.

**Bolus injection sequences** The first commonly used parameter is the time to peak (TTP), in seconds. It is defined as the time the echo-power takes to reach its maximum level. For a Dirac bolus, TTP represents the mode of the transit time distribution. By using a parametric model, the TTP can be estimated directly.

The mean transit time (MTT), in seconds, is very commonly used in DCE-MRI. It is defined as the statistical mean of the transit:

$$MTT = \frac{\int_{acq} t \cdot f_x(t) dt}{\int_{acq} t dt} \quad (2.4)$$

For a Dirac bolus, this quantity represents the mean of the transit time distribution.

The area under the curve (AUC) corresponds to the integral of the fit model, but the definition of the boundaries for the integration may vary from one study to another. The integration can be made for  $t \in T_{auc} = [0; \infty]$ , to compare data with different acquisition times. However, this extended integration range can cause artificially large variabilities in AUC values. The integration can also be performed over a finite time  $t \in T_{auc} = [0; t_{end}]$ . In this case, it is important to maintain the same integration interval from one acquisition to another.

$$AUC = \int_{T_{auc}} f_x(t) dt \quad (2.5)$$

In the initial development of the indicator dilution theory by Stewart and Hamilton [84, 85], used to assess in particular cardiac outputs, AUC was directly related to the cardiac output (CO) ( $CO = \frac{\text{Quantity of indicator}}{AUC}$ ), corresponding to the volume of blood pumped by the heart. By extension, it can be related to the volume of blood going through the tissue of interest.

TTP and MTT provide kinetic information about the vascular network, while AUC represents the amount of contrast agent flowing through the tumour.

The Wash in rate (WiR) is also estimated in some studies. It corresponds to the highest slope during the wash in phase. The AUC under wash-in or wash-out phases, correspond, respectively, to the area under the curve before and after the TTP.

**Destruction replenishment sequences** Two main parameters are generally extracted with DR data: the mean flow velocity is related to the speed at which the curve reaches a constant value. Its expression depends on the parametric fit model.

Alternative measurement of blood-flow rate can also be made. Its mathematical expression depends on the mathematical model fit to the curve. It is expressed as the value of the plateau (relative blood volume) multiplied by the mean flow velocity. This parameter correlates well with the real blood flow, in mL/min [41, 86].

## 2.6 Hypotheses behind the linear systems analysis

The different approaches and methodologies presented in this chapter implicitly make a certain number of hypotheses. As previously stated, the linear systems formalism assumes that the system has the properties of superposition and of scaling. Due to signal saturation, these properties are only valid when the contrast agent's concentration scales linearly with the detected echo-power. Moreover, the behaviour of microbubbles is assumed to be similar throughout the whole region of analysis. It has been shown [87] that the behaviour of adherent microbubbles such as those used in molecularly targeted imaging, is different from that of freely flowing microbubbles. More generally, the acoustic response of microbubbles is effected by their environment and the incident acoustic intensity is not completely uniform throughout the imaged plane. Thus, the assumption of uniform microbubble response throughout the ROA may not be well met under all imaging conditions. Also, the hypothesis of the uniqueness of the input function is questionable: tumours can present a complex vascular network with several blood supplies. Similarly, when considering small ROAs, regions are considered independent of one another although the blood flowing from one ROA may provide blood supply to an adjacent ROA. This hypothesis cannot be avoided, unless volumetric (three-dimensional) data are available.

Finally, when the echo-power  $f_x(t)$  is processed, the flow is assumed to be steady, and its pulsatile nature during the cardiac cycle is not taken into account. This hypothesis can be considered satisfied if the ROI is relatively far away from the heart in the vascular tree and if the pressure wave generated by the heart fades away before reaching the ROI. In practice, pulsatile artefacts are not observed on echo-power data curves so that this hypothesis is robust. In the rest of this thesis, these hypothesis are considered as valid, but they must be kept in mind. Future work taking them into account could contribute to further refinement of DCE-US imaging.

## 2.7 Perspectives for microvascular flow quantification with DCE-US

### 2.7.1 Clinical practice

While functional imaging and DCE-US imaging have been available and improved for more than 20 years, the clinical use of such techniques is still mainly qualitative, and quantitative indexes such as presented above are rarely used outside of large scale validation study such as [94]. Several reasons can explained the difficulty of the clinical transfer: first, because of the many factors previously mentioned, DCE-US still suffers from a high variability. Even if solutions are proposed to mitigate this variability, the techniques proposed can be seen as complicated to set up in routine clinical practice. Moreover, quantitative indicators extracted reflect a specific functional aspect, which for DCE-US is vascular network characteristics. Contrary to more general indicators such as the size of the tumor, they can not be by themselves exhaustive predictors of tumour state. Those characteristics, conjugate with the noisy nature of ultrasound imaging, have the consequence that individual quantitative parameters values are not yet fully trusted by clinicians for prognosis or diagnosis, because they are considered as too subjective and too variable. More coarse but less variable parameters such as morphological indicators [16] are still preferred for treatment decision making.

### 2.7.2 Pre-clinical studies

In pre-clinical studies, imaging modalities allowing to easily perform large number of acquisitions on small animals at a relatively low cost are desirable. DCE-US has these characteristics. Expected outcome of such studies is the identification of significant physiological differences between groups that can be related to the effect of a therapy, rather than an accurate prognosis or diagnosis for a single individual. DCE-US is able to non-invasively measure characteristics of the vascular network that are difficult or impossible to assess by other modalities. Therefore, it can lead to a better understanding of treatment effects on the characteristics of the vascular network, which is of high interest in particular in the context of anti-angiogenic therapies. This better understanding is also helpful in clinical practice, to improve qualitative evaluation: signs observed in patients can be related to phenomenon observed in pre-clinical studies. However, in order to extract useful information about the effect of a therapy, it is desirable to have parameters that can be related to specific properties of the vascular network. To be able to extract such parameters, it is thus necessary to take into account and develop methods to compensate for the effects of exogenous factors previously described, such as motion or input function. It is also important to base

the development of the post-processing method on accurate physical and physiological modelling of the tumour and the signal.

## 2.8 Conclusion

Many factors influence evaluation of flow with DCE-US: the injection, the type of acoustic input function modulation, the acquisition settings, the way data are linearised and the way the linear echo-power is processed. The sources of variability that are specifically addressed in the following chapters are those related to the linear echo-power post-processing. In Chapter 3, we characterize the multiplicative nature of DCE-US noise, and propose a model of signal that allows us to derive a new method to better fit parametric models to the DCE-US signal. In Chapter 4, a method is proposed to simulate DCE-US sequences that uses a texture generation algorithm: random noise textures with realistic properties in terms of statistics distribution and spatial correlation are generated. Breathing and probe motion affect DCE-US sequences and increase the variability of microvascular flow parameters. To decrease this variability, a new motion correction algorithm is proposed in Chapter 5. This algorithm takes into account the microvascular flow temporal dynamic to improve registration quality. In Chapter 6, a clustering method originally developed for DCE-CT and DCE-MRI sequences is adapted for DCE-US sequences. This method automatically detects heterogeneity in the flow, and should help to better take into account tumour heterogeneity when evaluating development and therapeutic response. Finally, Chapter 7 demonstrates, on an *in vivo* data set, the potential improvements that can be obtained by integrating the new fitting and clustering algorithms to sensitively assess tumour therapeutic response.

## Chapter 3

# Characterization and modelisation of DCE-US sequences<sup>1</sup>

### 3.1 Introduction

Among the different steps of the quantification of microvascular flow using DCE-US presented in Chapter 2, the influence of the fitting method on parameters variability has been largely overlooked.

From a probabilistic point of view, finding the parameters of the perfusion model is achieved by determining those that are most likely, given the echo-power data. The least squares criterion achieves this when the data are corrupted by an additive, independent, identically distributed, zero mean Gaussian noise [88]. Conventional B-mode ultrasound medical images have a granular appearance, the acoustic speckle, that originates from physical phenomena underlying image formation [89, 90]. Burckhardt [89] and later Wagner *et al.*[90] proposed that these data are best described by the Rayleigh distribution which is governed by the scale parameter  $\alpha$ . Thus, the probability density function (PDF) of the envelope ( $E$ ) of B-mode ultrasound data is:

$$p(E; \alpha) = \begin{cases} \frac{E}{\alpha^2} \exp(-E^2/(2\alpha^2)) & \text{if } E \geq 0 \\ 0 & \text{if } E < 0. \end{cases} \quad (3.1)$$

Modelling the signal with this single parameter distribution implies that there is a constant linear relationship between the mean  $\mu$  and the standard deviation  $\sigma$  of the envelope ( $\mu\sqrt{\frac{4}{\pi}} - 1 = \sigma$ ). Thus, it is well established that the envelope of B-mode ultrasound data presents noise that can be described by a multiplicative model. More recently, more sophisticated PDFs (sometimes with no obvious scaling-factor) have been introduced [91].

DCE-US images present the same type of granular appearance as seen in conventional, B-mode images. Although the nature of the speckle in DCE-US images suggests the multiplicative nature of the noise, only limited evidence of this multiplicative nature has been presented, based on signal correlation [92].

In the current work, theoretical background is first presented to demonstrate the link between the least squares fitting method and the assumption of additive gaussian noise. Then, our acquisition settings

---

<sup>1</sup>This chapter is adapted from Barrois, G., Coron, A., Payen, T., Dizeux, A., & Bridal, L. (2013). A multiplicative model for improving microvascular flow estimation in dynamic contrast-enhanced ultrasound (DCE-US): theory and experimental validation. *IEEE Transactions on Ultrasonics, Ferroelectrics, and Frequency Control*, 60(11), 2284-94 2013 [68]

for *in vitro* and *in vivo* DCE-US data are described. Using these experimental data, the non-additive nature of the noise corrupting contrast-enhanced ultrasound images acquired with a clinical ultrasound system is demonstrated. Therefore, least squares should not be the most appropriate criterion for fitting parametric models to clinical data. A multiplicative model for DCE-US data and a maximum likelihood approach to estimate perfusion parameters from such data are developed. Flow parameters estimated using the least squares criterion and the multiplicative-model based criterion are compared on simulated and experimentally acquired DCE-US data.

## 3.2 Additive model for DCE-US perfusion data

### 3.2.1 Model of signal

A sequence of  $N$  DCE-US frames is acquired at  $t_i$  with  $1 \leq i \leq N$ . Perfusion begins at  $t_1 = 0$ . To consider the general case, the methods of contrast agent injection and data acquisition are not specified. The echo-power data is represented by the function  $f(x, t_i)$ , where  $x$  is the spatial coordinates. To evaluate the evolution of the concentration of contrast agent in an analysis block around a pixel  $x$  and extract information on the vascularization, the mean linear-echo-power in the analysis block,  $f_x(t_i)$ , is usually assessed. To analyse  $f_x(t_i)$ , a parametric perfusion model with additive noise is considered:

$$f_x(t_i) = f_{+x}(t_i) = u(\theta_x, t_i) + v_{+x}(t_i) \quad (3.2)$$

where:

- $u$  is a parametric perfusion model describing the echo-power as a function of time.  $u$  is the information of interest.
- $\theta_x$  represents the local parameters of the parametric perfusion model  $u$ .
- $v_{+x}$  is a realization of a stationary zero-mean white Gaussian process  $V_{+x}$  with standard deviation  $\sigma$ .

### 3.2.2 Maximum likelihood criterion for additive model

In order to estimate the parameters of the model such that it best fits the echo-power data curve  $f_{+x}$ , the likelihood associated with Eq (3.2) is maximized. Considering the independence of the noise from one frame to another, using Eq (3.2), we can write the likelihood as the product of the probability density function of  $f_{+x}$  at all time points:

$$\begin{aligned} \mathcal{L}(\theta_x) &= \prod_{i=1}^N p_{F|\Theta_x}(f_{+x}(t_i)|\theta_x) \\ &= \prod_{i=1}^N p_{V_{+x}}(f_{+x}(t_i) - u(\theta_x, t_i)) \end{aligned} \quad (3.3)$$

The negative logarithm of Eq (3.3) is taken and the probability density of the noise is replaced by the Gaussian density. Maximizing the likelihood is equivalent to minimizing:

$$-\log \mathcal{L}(\theta_x) = \sum_{i=1}^N \left( \log(\sqrt{2\pi}\sigma) + \frac{(f_{+x}(t_i) - u(\theta_x, t_i))^2}{2\sigma^2} \right) \quad (3.4)$$

or solving the following problem:

$$\arg \min_{\theta_x} \sum_{i=1}^N (f_{+x}(t_i) - u(\theta_x, t_i))^2 \quad (3.5)$$

Eq (3.5) corresponds to the least squares solution [88] for the data  $f_{+x}(t)$ . This method of fitting will be termed LS method in the rest of the chapter. For an additive Gaussian noise model, the LS solution is the maximum likelihood solution. This is valid if the noise is Gaussian and identically distributed, but the validity of these assumptions is not demonstrated in the context of DCE-US.

### 3.3 Acquisition of DCE-US data

All *in vivo* and *in vitro* data were acquired with an Aplio 50 ultrasound imaging system and a PLT-1202-S linear probe (Toshiba Medical Systems, Tshigi, Japan), used with a transmit-frequency setting of h12.0 in Contrast Harmonic Imaging (CHI) mode. The mechanical index was fixed at a low level ( $MI = 0.1$ ) to avoid bubble destruction. The size of the pixels in the sequences is  $0.06 \times 0.06$  mm<sup>2</sup>. Many ultrasound system settings are cited without units as displayed on the Aplio monitor.

#### 3.3.1 Dose ranging data

Dose ranging experiments were conducted with BR38 experimental ultrasound contrast agent (Bracco Suisse SA, Geneva, Switzerland). Details of the experiment are described in [50]. The agent was reconstituted prior to the experiment in 5 mL of physiologic serum, to yield approximately  $2 \times 10^8$  microbubbles/mL. Data were acquired for dilutions from 1:400,000 to 1:250 of native reconstituted agent. Images were acquired during 10 seconds at 10 Hz, giving a total of 100 images for each concentration. Data acquisition from all dilutions was performed within less than 15 minutes to ensure that concentrations were not depleted by microbubble-gas dissolution. An image acquired from a suspension of BR38 at 1:1,000 dilution is shown in Figure 3.1. The bracket designates the gelatin stand-off placed between the transducer and the surface of the agitated microbubble suspension. The white rectangle delimits the region of interest in the contrast agent suspension from which average echo-power was calculated after linearisation of the data. Image pixel values were converted into echo-power using custom software developed by our group.

#### 3.3.2 *in vivo* data

DCE-US data were acquired in the transverse plane of the left kidney of a mouse. A total of 4 independent injections were performed through a catheter in the tail vein of 3 mice using a volume- and speed-controlled injection system [40], which allows a good repeatability of the injection. Each injection consisted of 50  $\mu$ L of SonoVue<sup>®</sup> (Bracco Imaging SpA, Milan, Italy) injected at 2 mL/min injection rate. The data for echo-power evaluation was extracted from the renal cortex, in an area where the perfusion is approximately homogeneous.

All the acquisitions were used for subsequent analysis except one acquisition removed due to a problem occurring during the injection.

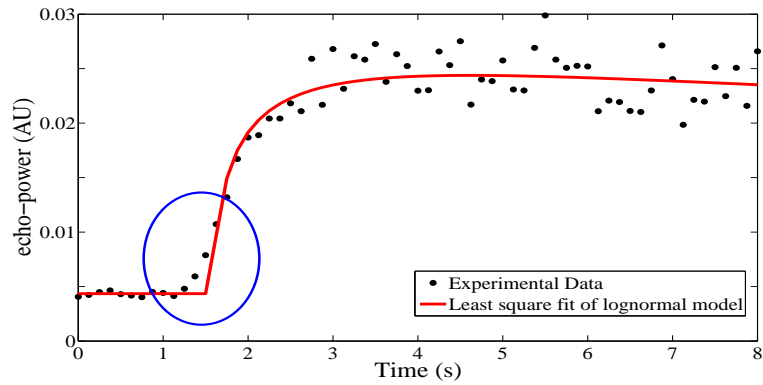


Figure 3.1: Image acquired during the dose ranging experiment ( $2 \times 10^5$  microbubbles/mL). The bracket designates the gelatin stand-off placed between the transducer and the surface of the microbubble suspension. The white rectangle delimits the region of interest in the contrast agent suspension from which average echo-power was calculated. Image pixel values were converted into echo-power using custom software developed by our group [50].

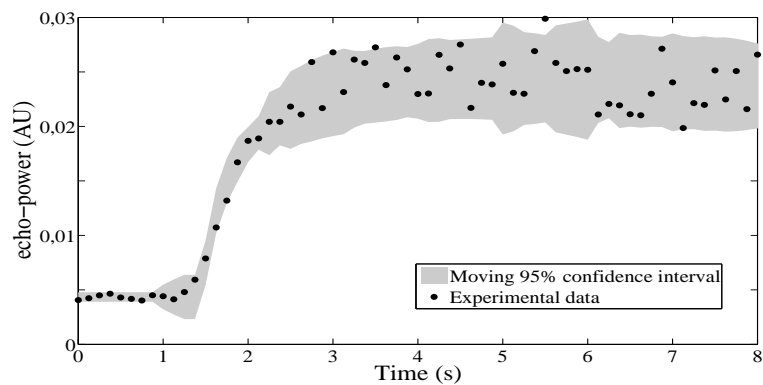
### 3.4 Experimental analysis of the nature of DCE-US signals

#### 3.4.1 Qualitative observations

An example of the first seconds of mean echo-power data acquired *in vivo* in murine kidney by DCE-US is presented in Figure 3.2. The mean echo-power has been calculated from a region of interest of  $18.72 \text{ mm}^2$  (5,200 pixels) that was selected to outline the renal cortex. The lognormal bolus perfusion model [69] fit to this data using the LS approach is shown by the solid, red curve. In Figure 3.2 (a), a lack of accuracy of the LS fitted model is apparent at the initial rise (circled region). This is not unique to this acquisition and was often observed in the experimental curves. In Figure 3.2 (b), a grey envelope representing the value of the local 95 % confidence interval is superimposed on the data. Its value has been calculated based on the estimation of the standard deviation of the residuals over sets of 8 neighbouring points, and assuming a gaussian distribution. This data illustrates that the standard deviation of the signal seems to increase as the level of the signal increases. This is not a feature anticipated for identically-distributed noise. In order to better evaluate the nature of the noise, the standard deviation was compared for signals with different echo-power levels acquired from controlled-dose concentrations of contrast agent.



(a)



(b)

Figure 3.2: In panel (a), the red curve represents the least squares solution for the lognormal function best describing the echo-power measured in the renal cortex of a mouse after injection of a bolus of contrast microbubbles. The curve does not fit the data well during the early rise of the bolus (as designated by the blue circle). In panel (b), a moving 95% confidence interval estimated at each time by assuming that the noise is Gaussian additive is shown by the grey shading. The non-homoscedasticity of the noise is demonstrated by the fact that the widths of this interval increases as the level of the echo-power increases.

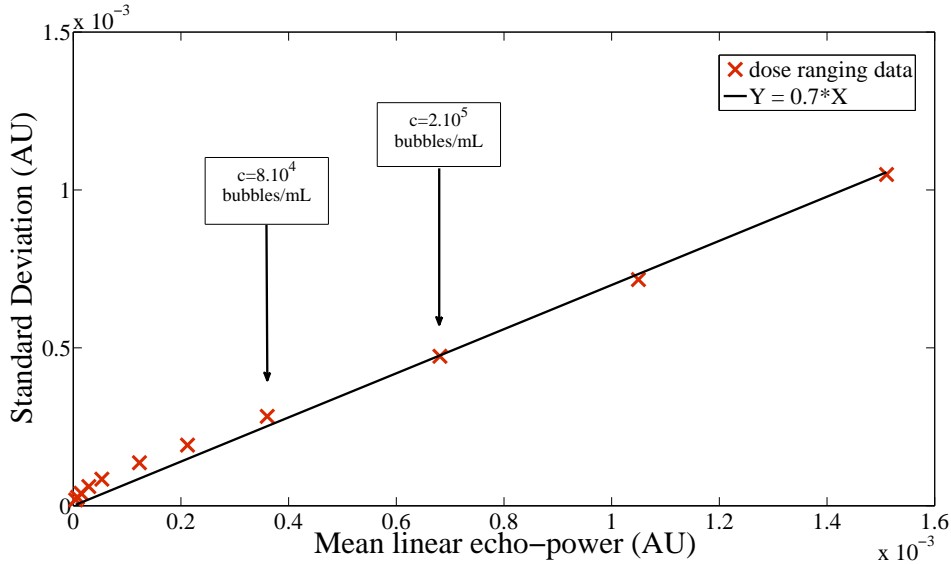


Figure 3.3: The mean linear echo-power and its standard deviation were calculated from 778,100 temporally independent measurements of the echo-power for different concentration of contrast agent suspensions (dose-ranging experiment). The red crosses represent the standard deviation of each data set as a function of its mean. The mean value is linked to the concentration in contrast agent: the data set with the lowest mean value corresponds to the lowest concentration in contrast agent ( $5 \times 10^2$  microbubbles/mL), the highest mean value to the highest concentration ( $8 \times 10^5$  microbubbles/mL). For constant additive noise, the standard deviation would be independent of the mean value of the echo-power and the data points would lie along a horizontal line at a level determined by the constant noise level. Clearly the data are not well described by such a model. A linear relationship between the standard deviation and the mean (estimated via linear regression) is proposed (solid line).

### 3.4.2 *In vitro* experiment: probability density function, mean and standard deviation of the DCE-US echo-power data

For a region of interest of  $1.86 \times 15.6 \text{ mm}^2$  ( $31 \times 251 \text{ pixels}$ ) in the focal area and the proximal zone of the contrast suspension (white rectangle in Figure 3.1), the pixel by pixel distribution of the linear echo-power was extracted. As the sequences were made of 100 images, the total number of linear echo-power estimation was 778,100 for each concentration. Examples of estimated probability densities functions for the linear echo-power at two microbubble concentrations are represented by the solid grey curves in Figure 3.4. The distributions are asymmetric and clearly exhibit a mode. Therefore, the function chosen to model the echo-power should have these properties. The mean linear echo-power and the standard deviation of the distribution of the linear echo-power are then calculated for each concentration of contrast agent. Each standard deviation is plotted as a function of the mean echo-power in Figure 3.3.

When a least squares method is used to fit a model to a perfusion curve, it relies on the assumption that the relationship between the standard deviation and the mean of the experimental data as presented in Figure 3.3 can be modeled by a horizontal line chosen somewhere between the minimum and maximum standard deviations. The assumption of a linear proportionality between the standard deviation and the mean is clearly closer to the experimentally determined characteristics. This relationship implies that a

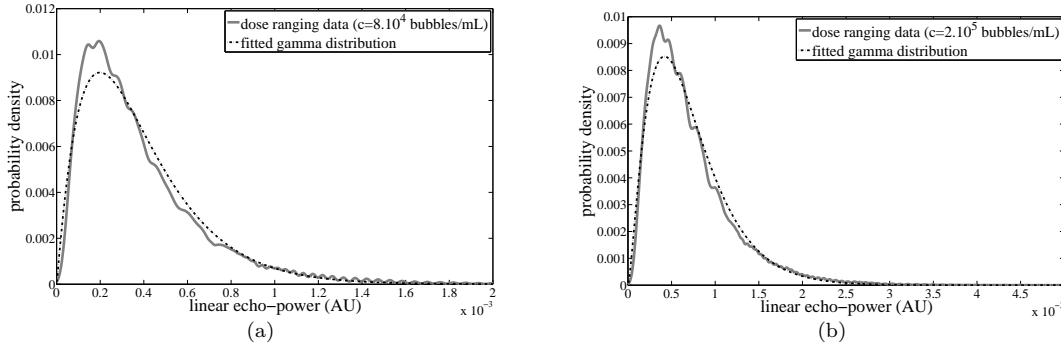


Figure 3.4: Distribution of data as experimentally determined from 778, 100 linear echo-power estimations (solid grey line) fit to a gamma probability density (black dotted line). Data are from suspensions of  $8.10^4$  microbubbles/mL (a) and  $2.10^5$  microbubbles/mL (b).

multiplicative model should better describe the noise. It is therefore, relevant to develop a multiplicative model for the estimation of parameters from DCE-US echo-power data curves.

### 3.5 Multiplicative model for DCE-US perfusion data

#### 3.5.1 Model of signal

To better describe the nature of the DCE-US data, the echo-power at  $x$  or in a region around  $x$ ,  $f_x(t_i)$ , is modeled as the multiplication of a realization of the stationary stochastic process  $v_{*x}$  and  $u$ :

$$f_x(t_i) = f_{*x}(t_i) = u(\theta_x, t_i)v_{*x}(t_i). \quad (3.6)$$

The ultrasound echo-power is the square of the amplitude of the envelope. Therefore, because the sum of the squares of  $n$  random variables following a Rayleigh  $R(\sigma)$  distribution (Eq 3.1) follows a gamma distribution  $gamma(n, \sigma^2)$  [93], a gamma distribution was chosen to represent the probability density of the noise  $v_{*x}$ . Furthermore, as we use a clinical ultrasound system, we estimate the echo-power of each pixel from the JPEG images encapsulated in DICOM files that were linearized [50]. Considering that those images are not directly computed from the envelope of the RF, a gamma distribution

$$p_{V_{*x}}(v) = gamma(v; k, \alpha) = \begin{cases} \frac{v^{(k-1)}}{\Gamma(k)\alpha^k} \exp \frac{-v}{\alpha} & \text{if } v \geq 0 \\ 0 & \text{if } v < 0 \end{cases} \quad (3.7)$$

is a good compromise in terms of accuracy and flexibility, as shown with the two examples of the PDF given in Figure 3.4. For the gamma distribution, the ratio of the standard deviation  $\sigma$  is equal to  $\frac{\mu}{\sqrt{k}}$ . Therefore, the  $k$  parameter controls the sharpness of the gamma distribution of the noise  $v_{*x}$ . The 0.7 slope value obtained in Figure 3.3 corresponds to a  $k$  value that is approximately equal to 2.

In order to apply the maximum likelihood estimation to this distribution, we impose the mode of the gamma distribution to be one, which is equivalent to  $\alpha(k-1) = 1$ . This condition for a multiplicative model is the equivalent of imposing a centered noise for an additive model. Therefore, the distribution can be parametrized by a single parameter:

$$p_{V_{*x}}(v) = gamma\left(v; k, \frac{1}{k-1}\right) \quad (3.8)$$

### 3.5.2 Maximum likelihood criterion for multiplicative model

As for Eq (3.2), in order to estimate the parameters of the perfusion model such that it best fits the echo-power data curve  $f_{*x}$ , the likelihood associated with Eq (6.1) is maximized. Supposing the independence of the noise from one time to another, the likelihood can be expressed as

$$\mathcal{L}(\theta_x) = \prod_{i=1}^N p_{F|\Theta_x}(f_{*x}(t_i)|\theta_x), \quad (3.9)$$

which can be rewritten as

$$\mathcal{L}(\theta_x) = \prod_{i=1}^N p_{V_{*x}}\left(\frac{f_{*x}(t_i)}{u(\theta_x, t_i)}\right). \quad (3.10)$$

Replacing the distribution of the noise by Eq (3.8), taking the opposite of the log-likelihood, the problem aims to solve

$$\arg \min_{\theta_x} \sum_{i=1}^N \left( (k-1) \log(u(\theta_x, t_i)) + (k-1) \frac{f_{*x}(t_i)}{u(\theta_x, t_i)} \right) \quad (3.11)$$

which is equivalent to solving

$$\arg \min_{\theta_x} \sum_{i=1}^N \left( \log(u(\theta_x, t_i)) + \frac{f_{*x}(t_i)}{u(\theta_x, t_i)} \right). \quad (3.12)$$

This equation does not depend on the parameters of the noise distribution. The rest of the regression process consists in finding the minimum of this function in the parameter space. Note that no assumptions have been made about the perfusion model function and the number of parameters in the model, which makes this method applicable to all parametric models and types of contrast agent injection. This method will be referred to as the MM method.

## 3.6 Validation of the multiplicative model on simulated and in vivo data

### 3.6.1 Perfusion data

#### Simulation of perfusion data

In order to compare the two models in terms of error in the estimation of the parameters, simulated data were used. A set of data was generated based on the multiplicative model presented in Eq (6.1). Bolus injection data were simulated because it is currently the most commonly evaluated type of injection. To generate the data, we selected as an echo-power data curve model the lognormal model introduced by Rognin *et al.*[69]:

$$u((m, s, c, A), t) = A \frac{\exp\left(\frac{-[\log t - m]^2}{2s^2}\right)}{\sqrt{2\pi}ts} + c \quad (3.13)$$

with

- $m$  the mean of the underlying normal distribution,
- $s$  the standard deviation of the underlying lognormal distribution,

- $c$  an offset to take into account the fact that the echo-power is not zero when the concentration in microbubbles is zero,
- $A$  a scaling parameter.

Each point of the curve was generated from the lognormal model and the gamma distribution, with the noise distribution parameter  $k = 3$  that corresponds to a mean signal coming from a small analysis block of  $5 \times 5$  pixels in the dose ranging data. By considering small blocks instead of pixels, the distribution of the linear echo-power is slightly sharper than in Figure 3.3 but the signal is still very noisy. In the fitting phase, the parameter  $c$  was estimated independently of the fitting process using an average of the points before bolus arrival.  $A$ ,  $m$  and  $s$  are determined by the fitting algorithms. The sampling of the data was chosen to be 0.2 s and each simulated data record was 60 s long, which correspond to typical values encountered in experimental data. Once each fit was performed, quantitative perfusion parameters were extracted from the fitted curves and compared to the values used to generate the data. Four widely used perfusion parameters were compared in this study :

- Wash in Rate (WiR): maximum gradient during the wash-in phase.
- Area under curve (AUC): integral of the best-fit curve during the acquisition.
- Mean transit time (MTT): mean value of the lognormal distribution underlying the data, given by  $MTT = \exp(m + s^2/2)$ .
- Time to peak (TTP): time of the maximum of the best-fit curve, given by  $TTP = \exp(m - s^2)$ .

The values of the simulated perfusion parameters were chosen in a realistic range and to represent the broad range of shapes encountered in DCE-US evaluations. Data were generated for MTT varying from 25 s to 175 s with a 15 s step (11 values) and for TTP varying from 8 s to 24 s with a 2 s step (9 values): 99 different sets of parameters. For each set of parameters, 500 curves were simulated. The total number of simulations was therefore 49,500.

### Analysis of *In vivo* perfusion data

The maximum likelihood and least squares regression methods were applied to echo-power data curves calculated of  $5 \times 5$  pixels (about  $0.3 \times 0.3 \text{ mm}^2$ ) distributed in the renal cortex. In each acquisition, the renal cortex was divided into 140 to 217 analysis blocks. The union of all the analysis blocks for a given acquisition is referred to as the region of interest.

### Criteria for comparison and handling of outliers

The performances of the MM and LS approaches were compared based on the perfusion parameters presented earlier WiR, AUC, TTP and MTT, because these parameters are used in clinical evaluations. Results were compared for the simulated data sets using a criterion of accuracy, the absolute error, given by  $\frac{|RealValue - EstimatedValue|}{RealValue}$  in % and a criterion of precision, the variation coefficient given by  $\frac{std(EstimatedValue)}{Mean(EstimatedValue)}$  in %. For each parameter, the evaluation of the accuracy of the methods is of interest because the maximum likelihood does not guarantee the absence of bias. For the comparison of MM and LS approaches using the *in vivo* DCE-US data sets, only a precision criterion can be used. It is assessed

Lognormal parameters	LS criterion		MM criterion	
	mean		mean	
	abs. error.	var. coeff.	abs. error.	var. coeff.
	%	%	%	%
$A$	50.3	12.9	49.8*	10.5*
$m$	3.7	4.3	2.7*	3.3*
$s$	5.8	7.3	3.9*	4.9*
Perfusion parameters	LS criterion		MM criterion	
	mean		mean	
	abs. error.	var. coeff.	abs. error.	var. coeff.
	%	%	%	%
MTT	22.0	17.3	15.5*	12.7*
TTP	5.6	7.0	4.3*	5.4*
AUC	3.3	4.0	3.2*	3.9*
WiR	9.3	11.8	7.0*	8.8*

Table 3.1: Precision and accuracy for the two methods on simulated data for perfusion parameters. Significantly better ( $p < 0.05$ ) results are marked with an asterisk (\*)

by computing the standard deviation of parameters values obtained from the data blocks in the region of interest. Statistical analysis was conducted using a paired t-test to compare the mean absolute errors in the simulated data set and using Levene's test to compare the variances of the parameter distributions in the simulated and *in vivo* data sets. Differences were considered as significant for  $p < 0.05$ .

In the *in vivo* data set, due to the high level of noise from small voxels of data, the fit of the perfusion model in some analysis blocks can fail. This can lead to outliers in the extracted perfusion parameters values. Parameter estimates from analysis blocks with failed fits were identified and removed according to the following criteria: if an extracted perfusion parameter is greater than 5 times or less than 1/5 the median of the parameters extracted from the other data blocks in the region of interest (relatively homogeneous renal cortex), it was considered to be an outlier, and it was removed.

### 3.6.2 Results

#### Performance comparison on simulated data

The mean accuracy (absolute error) and precision (coefficient of variation of the estimations) of the three lognormal parameters and four perfusion parameters estimated from all the simulated echo-power data curves are summarized in Table 3.1. Statistical tests have been run over the absolute errors of all the simulations. The MM criterion provided better mean accuracy and significantly better precision than the LS approach for all model and perfusion parameters. For both of the fitting methods, the errors made on the lognormal parameter  $A$  are quite large. This is probably due to the fact that a small error on  $m$  or  $s$  leads to a large compensation by  $A$ . In spite of this, estimation errors on  $A$  do not seem to strongly affect the perfusion parameters. MTT, the perfusion parameter with the largest errors, is independent of  $A$ . Boxplots of the absolute errors are displayed for ranges of parameter values in Figure 3.5. The asterisks

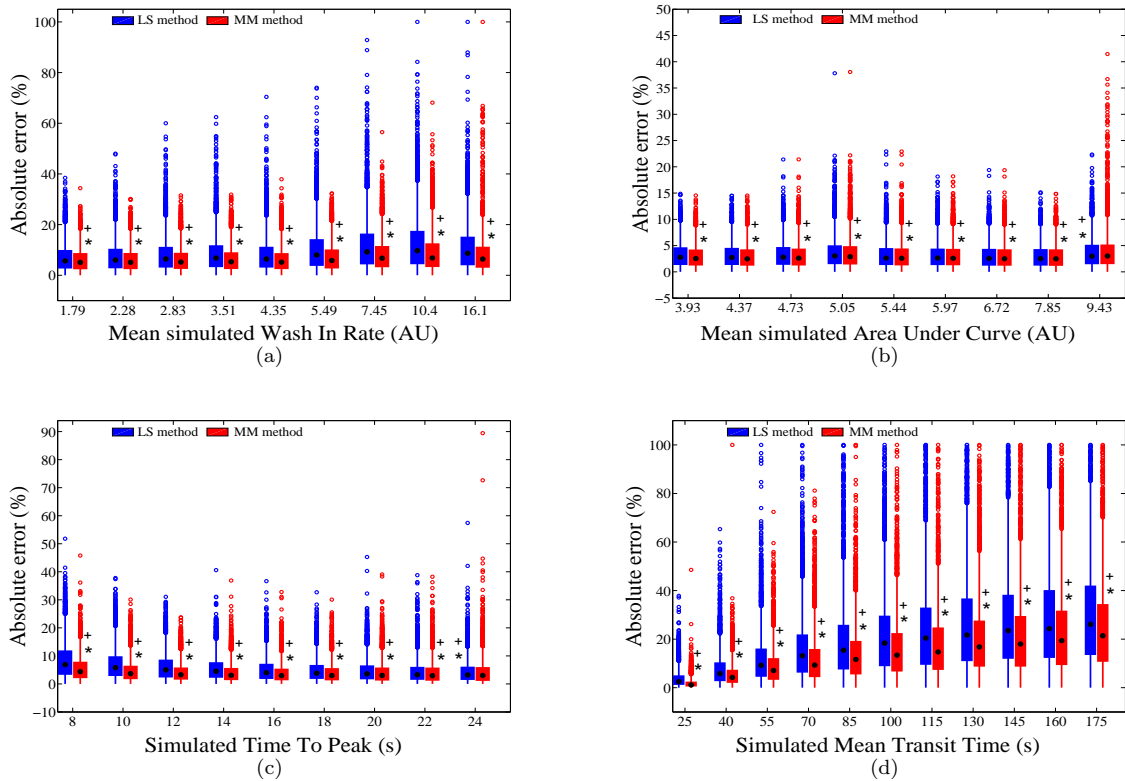


Figure 3.5: Boxplot of the absolute errors as a function of the value of the perfusion parameters Wash in Rate (WiR), Area Under Curve (AUC), Time To Peak (TTP) and Mean Transit Time (MTT). The parameters were estimated by fitting the 49,500 sets of simulated data using the MM (Multiplicative Method) and the LS (Least Squares) fitting techniques. The asterisks mark the method that has the best precision (smallest coefficient of variation). The crosses mark the method for each paired comparison that has the best accuracy (lowest mean absolute error). The seemingly high density of out-of-range points (marked with circles, defined as values superior to  $q_{75\%} + 1.5(q_{75\%} - q_{25\%})$ ) is due to the high number of simulations (5,500 simulations for TTP, AUC and WiR values, 4,500 for each MTT value) but represent only 3% of the total number of points.

and crosses above the bars, which indicate, respectively, the most precise and accurate methods, show that the MM criterion outperformed LS criterion in terms of precision and accuracy except for the longest value of simulated TTP and for the highest AUC. Also, the precision of the LS estimated parameters are reduced when the WiR or the MTT increases and when the TTP decreases. These trends are also observed for the MM estimated parameters but to a lower degree.

The parameters obtained in these noisy simulated data using the maximum likelihood based on the multiplicative model criterion are more precise and accurate than those obtained using the least squares criterion in most of the cases. This was anticipated since the simulated data were constructed using the gamma distribution model for the noise that is used to construct the MM criterion. Nevertheless, this noise model was selected for simulations based on the experimentally determined form of the noise (Figure 3.4). Thus, the simulated results should be on the order of those observed for experimentally acquired DCE-US data.

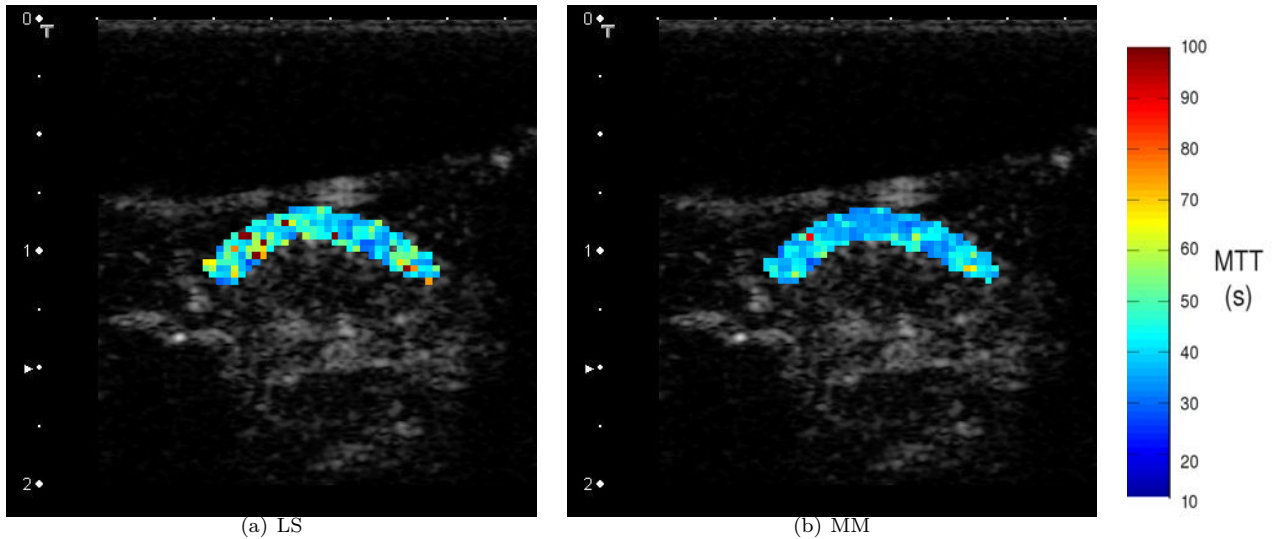


Figure 3.6: Images constructed based on the DCE-US acquisition of bolus-passage sequence in the kidney of a mouse. A parametric map corresponding to the value of the parameter Mean Transit Time (MTT) estimated using the LS criterion in Figure (a) and the MM criterion in Figure (b) is superimposed on the renal cortex. The color of a pixel of the parametric map corresponds to the value of MTT estimated for the signal coming from one analysis block ( $5 \times 5$  pixels patch). It is observed that the MTT values are more homogeneous in the map estimated using the MM criterion.

#### Performance comparison for in vivo data

Perfusion parameters (TTP, MTT, AUC and WiR) obtained within the analysis blocks in the same region of interest via the two methods of estimation are compared. Example parametric maps of MTT obtained with the two methods for the same acquisition are presented in Figure 3.6. The complete results are presented in Figure 3.7. For each acquisition, boxplots of the distributions of the parameter estimated using MM and LS criterion are compared. Results that have a significantly ( $p < 0.05$ , Levene's non parametric test) lower coefficient of variation (after removing the outliers) are marked with an asterisk.

The coefficient of variation for the *in vivo* data are often larger than those observed on simulated data. This is expected because the area of perfusion of the renal cortex is only approximately homogeneous. For the 11 independent sets of data acquired, the MM criterion exhibits lower coefficients of variation over the region of interest for 9 TTP, 10 MTT and 10 WiR parameter maps. The coefficients of variation were not significantly different for the AUC parameter. The mean percent decreases of the coefficient of variation for TTP, WiR and MTT were, respectively, 40%, 25% and 59%. This is consistent with the results obtained on simulated data. Moreover, for all the data acquired *in vivo*, parameter calculation with the MM method led to a smaller or equal number of outliers as compared to the same parameter calculated with the LS method. The smaller number of outliers obtained with the MM method indicates that the estimator provides greater stability than the LS method.

A high coefficient of variation on *in vivo* data does not necessarily mean that the estimator is not precise: the coefficient of variation could be due to the natural variability of the data. However, the similarity of the *in vivo* results with results obtained on simulated data suggests that at least a part of the differences of coefficient of variation observed here between MM and LS, are due to the better precision of the MM criterion.

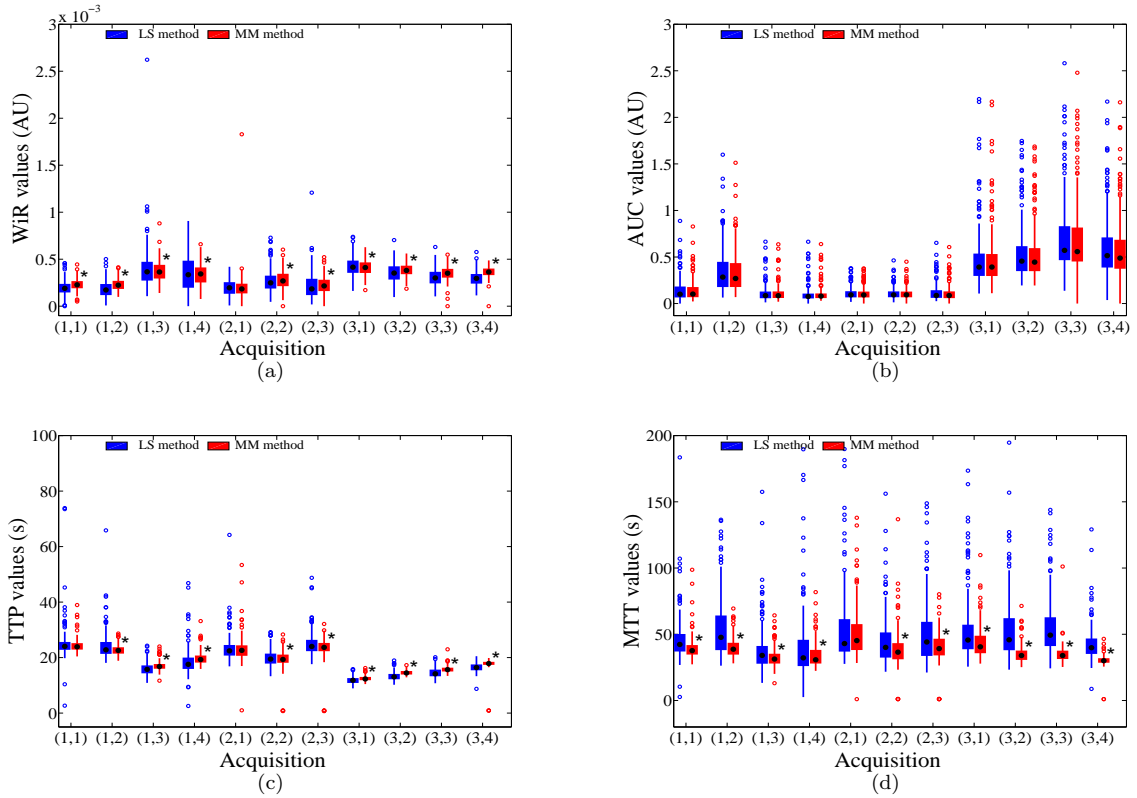


Figure 3.7: Each parameter was estimated for all the analysis blocks in the selected region of interest of the kidney of 3 mice. Data acquired on independent days are displayed for each mouse. In the labels of the abscesses, the first number in the parentheses corresponds to the mouse number, the second corresponds to the acquisition number. For each perfusion parameter, boxplots of the distribution of parameter estimates in the region of interest obtained using the two methods are presented. When distributions were significantly different ( $p < 0.05$ , Levene’s non parametric test) that with the lower coefficient of variation is marked with an asterisk

### 3.7 Discussion

The Gamma distribution chosen in this work to model the distribution of the squared amplitude of the envelope has some convenient characteristics: it only depends on two parameters, its mode can be expressed analytically and the resulting maximum likelihood estimator does not depend on the distribution parameters. This choice can be debated. Indeed, it is based on a Rayleigh modeling of the echo-power, but more general models such as the Rician distribution, exist. Integration of a more sophisticated model for maximum likelihood estimation will result in an increased mathematical complexity and/or larger numbers of parameters. For instance, computing the maximum likelihood while assuming a squared Rician distribution leads to the presence of a Bessel function in the metric, and the maximum likelihood estimator is no longer independent of the distribution parameters. Although several studies have considered the characteristics of the B-mode signal distribution [91], little information exists on the distribution characteristics in harmonic mode. In this study, our primary aim was not to identify the most sophisticated distribution model but was rather to demonstrate that the least squares minimization was intrinsically not adapted to DCE-US data and to propose a simple alternative that is more consistent

with the nature of DCE-US signal and noise.

The lack of agreement between the modelled curve and the data points at the initial rise of the bolus curve (Figure 3.3) indicates a relative lack of accuracy of the multiplicative model at low echo-power levels. This may be due to the fact that, for low concentrations of contrast microbubbles, different types of noise combine. The method used to estimate the  $c$  parameter of the lognormal model implicitly makes the hypothesis that the distribution of the signal is additive symmetric (with a mean value equal to  $c$ ) before the arrival of the bolus of contrast agent. We assume however that, upon arrival of the bolus, the multiplicative part of the noise is predominant. To fully describe the mixed nature of the noise at low concentrations will require a complimentary modeling of the signal. At lower concentration, rather than the Rayleigh noise of DCE-US signal, the most significant effect could be the statistic of arrival of the microbubbles, and models of the echo-power data curve as transit time distribution histograms, such as proposed in [83] could make the model more accurate at low concentrations.

The coefficients of variation of perfusion parameters obtained from simulated and *in vivo* experimental data for bolus injections provide clues that may explain some trends observed by other authors [46, 94]: the poor efficiency of MTT in clinical studies could, at least in part, be explained by the very high coefficient of variation induced by the least squares fitting. Similarly, the efficiency of time to peak, wash in rate, or other parameters that aim to capture the form of the wash-in, may have been hidden by the poor fitting of this part of the curve induced by the least squares fitting method. The new fitting method improves the fitting of this part of the curve and could lead to reconsider the best parameters for diagnoses. In this study, a more rigorous mathematical framework has been proposed for parameter extraction in contrast-enhanced ultrasound perfusion curves. The demonstration of the efficiency of the new method has been done using bolus injection data curves. However, as the difference between the MM and the LS criterion comes from the nature of the signal, it is very likely that similar results (better precision and accuracy of the fitting) would be obtained for all models and injection types.

The comparison of the performance of the MM and LS criteria has been quantitatively estimated on noisy data, which corresponds to perfusion data coming from the mean over a few pixels (Figure 3.6). However, this does not at all mean that use of this method is of interest only for very noisy data. Indeed, even if by averaging the noise over more pixels, the distribution of the noise (that we have approximated by a gamma law) better approaches a gaussian law due to the central limit theorem, the multiplicative nature of the noise remains (Figure 3.2). Therefore, the MM criterion will still be intrinsically better than the LS criterion, in particular for the fitting of the beginning of the perfusion curves.

In order to quantify the least squares fit, a quality of fit (QOF) index is proposed by Rognin *et al.*[55], based on the computation of a ratio between the sum of the squares of the residuals (SSR) and the total sum of squares (SST). However, the derivation of this QOF index, using the least squares method of fitting, is directly derived from an additive model of the noise which was demonstrated to fail in this study. The new model of signal proposed in the current work should contribute to future developments of new indexes that would better indicate the reliability of parameters estimated from DCE-US data.

Many other factors can lead to important uncertainty in DCE-US perfusion evaluation (movement, variation of injected doses/population/response of bubbles, attenuation and propagation effects). Authors have shown that quantitative DCE-US imaging can be degraded by attenuation or time-dependent modifications of contrast agent [47]. Taking into account such effects is important in assuring the accu-

racy and the precision of quantification in DCE-US imaging. Much work has addressed methods aimed at reducing these sources of variability, and control of these factors is essential in obtaining good DCE-US evaluations. The relative variability due to each of these factors depends highly on the experimental conditions and tissues considered. The results reported in this chapter should be used in conjunction with optimized experimental and signal analysis choices. The strength of the method offered by the current work is that it can be applied universally to clinical DCE-US data. In particular, bias of the fit at the beginning of the perfusion curves is reduced. This is of particular interest because the information most sensitive to changes in the microvascular flow has been shown to be mainly contained in the first passage of the bolus [95]. Therefore, having a method that more accurately fits the first seconds of the perfusion curve is of widespread interest for better discrimination of perfusion parameters. Moreover, local evaluation of perfusion and parametric mapping has been limited due to the high level of noise in echo-power estimations from a small volume of scattering structures. By better addressing the nature of the noise, our method can improve the fit of data from small voxels and provide higher resolution parametric mapping.

### 3.8 Conclusion

In this chapter, we aimed to develop a new mathematical model of perfusion data in DCE-US that considers the multiplicative nature of the noise. From this, a new fitting method was derived. To demonstrate that this new method improves estimation of flow parameters, first, the highly non-additive nature of the noise was demonstrated using *in vitro* data from harmonic imaging of suspensions of contrast agent at different doses. A multiplicative model for the signal was then proposed and a new mathematical method to extract the perfusion parameters was derived. Using simulated data, this new method was demonstrated to be more precise and more accurate than least squares fitting. This improved precision was upheld when the two techniques were compared on *in vivo* data. In light of these results, this simple-to-implement new method should be used to fit parametric models to DCE-US echo-power data. Use of the method in future studies may modify relative robustness of parameters for diagnosis and should improve the perspectives for parametric imaging able to better resolve local differences in tissue perfusion.

### 3.9 Acknowledgements

The BR38 microbubbles were kindly provided by Bracco Suisse SA.

## Chapter 4

# Simulation of DCE-US sequences<sup>1</sup>

### 4.1 Introduction

Software is available for the simulation of ultrasound data for a defined arrangement of scattering structures and sound propagation conditions, such as Field II developed by [97] or CREANUIS presented in [98]. Such software simulates linear and non-linear propagation and scattering of ultrasonic waves based on detailed maps of scatterer distributions. To simulate dynamic ultrasound sequences from microbubbles in a complex vascular network, the time-varying distribution of the flowing microbubbles would need to be mapped to simulate each frame of the sequence. Although this could be of considerable interest, modelling flow in a microvascular network would be very computationally demanding and no such simulation has been reported using Field II or CREANUIS.

The objective of this work is to propose an alternative and simpler approach to simulate DCE-US sequences representative of data observed in tissues with complex microvascular networks. This technique could be useful for the simulation of DCE-US sequences to evaluate quantification, motion compensation algorithms or attenuation correction models.

The original approach proposed to simulate DCE-US perfusion data reposes on an example-based algorithm [99]. Example-based texture generation methods allow construction of arbitrarily large textures based on a sample and preserve spatial structure and intensity distribution. The quality of the texture of DCE-US noise obtained with such an algorithm is assessed in terms of its spatial correlation and distribution. A framework combining these simulated textures with data describing the evolution of contrast agent concentration as a function of time at each pixel is developed to provide a simple but realistic sequence in terms of its spatial correlation and distribution model of DCE-US data.

---

<sup>1</sup>This chapter is adapted from Barrois, G., Coron, A., & Bridal, L. (2014). Simulation of dynamic contrast-enhanced ultrasound sequences using example-based texture generation. IRBM. [96]

## 4.2 Materials and methods

### 4.2.1 Dose-ranging data

#### Acquisition

The same set of data acquired from calibrated-concentration solutions of ultrasound contrast as used in Chapter 3 is used in this work. The acquisition protocol have been described in Section 3.3.1.

#### Sample and seed extraction

One of the 40 images at each dose was randomly chosen to be used for sample and seed extraction. The other 39 were then used for evaluation. From the selected image a sample of  $31 \times 101$  pixels was selected close to the solution's surface, in an area where the signal was homogeneous and not significantly attenuated. From this sample, a  $3 \times 3$  pixels seed was randomly selected and used to initialize the  $K$ -coherence algorithm (Figure 4.1).

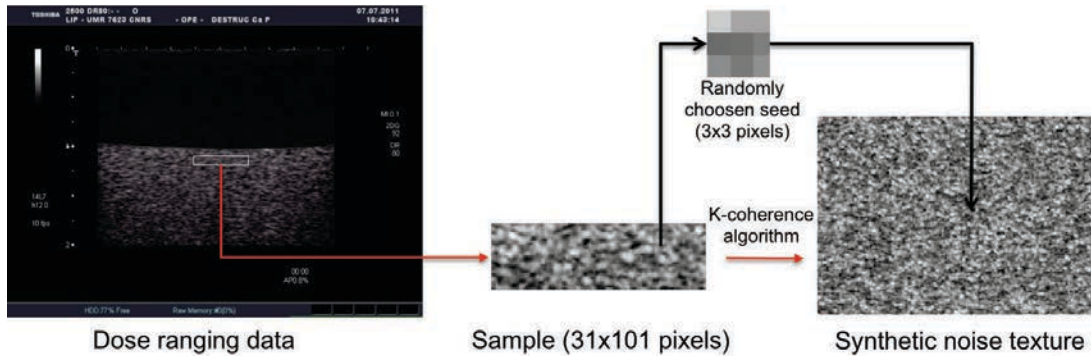


Figure 4.1: The use of the dose-ranging data in the context of  $K$ -coherence. From a selected image for each contrast microbubble concentration, a region was selected in the superficial portion of the contrast solution (box outlined in white on the image). A seed was randomly extracted from this sample and the  $K$ -coherence algorithm was run to generate a synthetic noise texture.

### 4.2.2 Simulation of DCE-US sequences

#### Signal model

To consider additive noise, dominant at low concentrations, the contrast echo-power at  $x$  at time  $t_i$ ,  $f_x(t_i)$ , is modelled as the signal anticipated from the perfusion dependent contrast concentration, or the perfusion signal,  $u$ , corrupted by a multiplicative speckle-noise term,  $v$ , and an additive baseline noise term,  $\epsilon$ :

$$f_x(t_i) = u(t_i) \cdot v(t_i) + \epsilon(t_i). \quad (4.1)$$

The speckle-noise,  $v$ , is due to the random fluctuations of the power detected from the distributions of sub-wavelength-sized contrast microbubbles. The additive baseline noise  $\epsilon$  is due to electronic noise which is present with and without contrast agent. The perfusion signal that is assumed to describe the variation of the contrast echo-power as a function of contrast agent concentration. Therefore, the speckle-noise

term is normalized to have a distribution with a mode value equal to 1. The distributions and the spatial correlation properties of the terms  $\epsilon$  and  $v$  are assumed to be constant.

### ***K*-coherence noise generation**

Equation (4.1) includes a speckle and a baseline noise component. In order to realistically simulate these, an example-based texture generation algorithm was used. Example-based texture generation methods allow construction of arbitrarily large textures from a sample image while preserving spatial structure and intensity distribution.

The *K*-coherence algorithm [99] was chosen because of its speed and simplicity. This algorithm, has two phases: analysis and synthesis. During the analysis phase, for each input pixel of the sample, a similarity set of the  $k$  most similar pixels (in the sense of the minimum squared difference of the contrast echo-powers) in the sample is constructed. The first step of the synthesis phase is to initialize the center of simulated image with a seed (selected from the sample). The pixels adjacent to the seed (which initially have no attributed value) are then successively filled as follows: for the current pixel to fill, a candidate set is constructed based on its filled neighbourhood (i.e. pixels in its neighbourhood that have been attributed a value) and on the similarity sets constructed during the analysis phase. A value for the current pixel is chosen among the best candidates in the candidate set. The algorithm continues to the next pixel to fill. This iterative process allows the initial seed to grow progressively, until it reaches the size specified by the user. A detailed description of the algorithm is given in pseudocode in appendix A to facilitate implementation.

Because of the random nature of speckle noise, the algorithm is designed to allow randomness in the generated texture: the seed is selected randomly in the sample and the choice of the value in the candidate set is chosen randomly among the best candidates. The size of the neighbourhood is set to 3 to allow variations in the simulated texture while limiting the computation time. Higher values of neighbourhood size lead to a size-dependant increase computation time (55% longer for 5 neighbours than for 3) without a significant gain in the statistical distribution and spatial correlation of the generated texture.

The baseline noise  $\epsilon$  is constructed using a sample from the dose-ranging data at the concentration of 0 microbubbles/mL. The speckle-noise term,  $v$ , is constructed using a sample from the dose-ranging data at a concentration of  $8 \times 10^4$  microbubbles/mL and then normalized to have a mode value equal to 1. This concentration has been chosen because overall, it leads to the most realistic correlations and distributions (the quantitative measures of realism are presented after in Section 4.2.3) for the different simulated concentrations. In this particular configuration, the time to generate one texture of baseline noise or of speckle noise is approximately 25 s for a texture of 91728 pixels on a desktop computer.

### **Parametric noise generation**

To compare the *K*-coherence noise generation to a reference method, a parametric method of simulation was used. The parametric method is the method that is used, for instance in [70] or [100]. Speckle-noise  $v$  from equation (4.1) is generated from a given distribution and combined to the perfusion signal. Baseline noise  $\epsilon$  is assumed to be zero. The contrast echo-power is assumed to follow a Gamma distribution. This distribution has been shown in [68] to well describe the dose-ranging data.

The parameters of the Gamma distribution are estimated using a maximum likelihood estimator

applied on data extracted from the 40 images of the dose-ranging data at  $8 \times 10^4$  microbubbles/mL in the same  $31 \times 101$  pixels zone close to the surface of the solutions as used in the  $K$ -coherence algorithm. The distribution is then normalized to have a mode value equal to 1.

### Perfusion signal generation

The perfusion term,  $u$ , models the evolution of the echo-power due to variation of contrast agent concentration with time: the value of  $u$  at pixel  $x$  as a function of time represents the echo-power that would be measured from that pixel for perfectly denoised experimental data. To generate  $u$ , noisy perfusion curves were extracted from each pixel in an experimentally acquired  $2D$ +time perfusion sequence and then low pass filtered. A moving median with a 20 sample large window was applied to smooth the experimental curves, which are corrupted due to speckle noise and noise due to motion. This window size has been chosen to remove the noise and the motion without affecting the perfusion dynamic. The resulting smoothed curves were used to reconstruct a  $2D$ +time perfusion sequence.

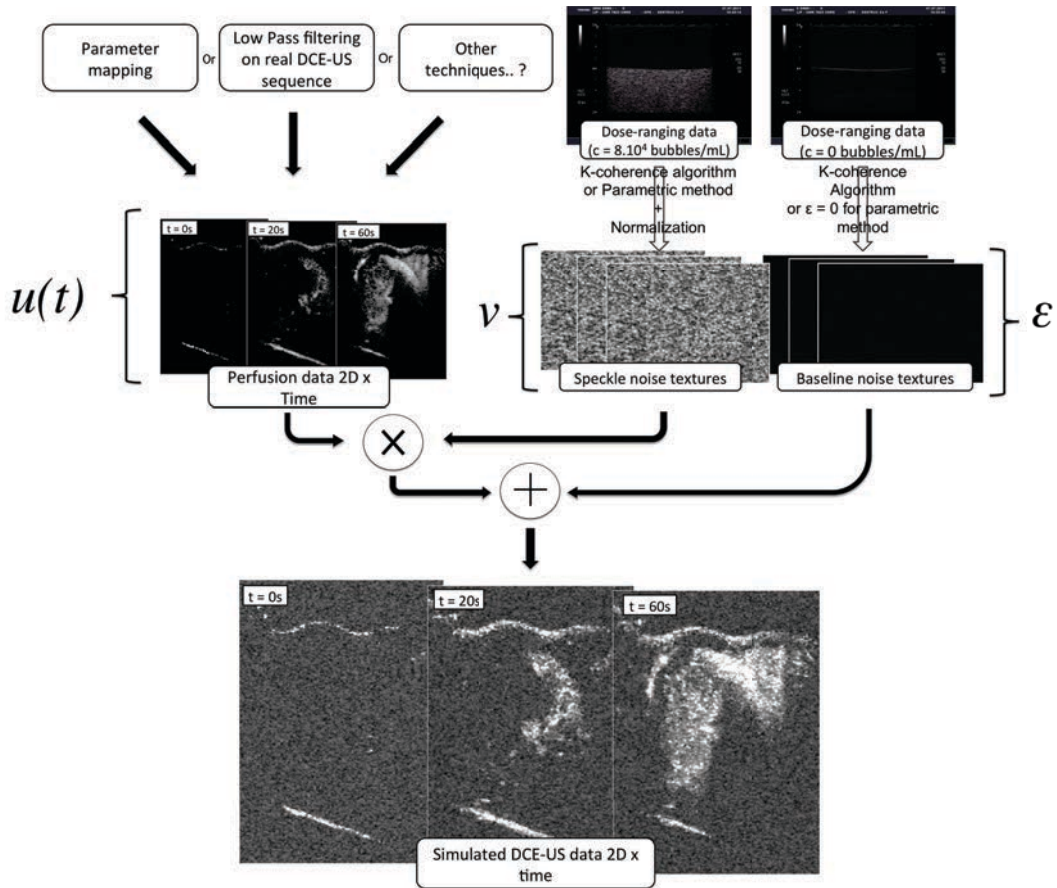


Figure 4.2: Diagram of the different steps of the simulation of DCE-US sequences. The first step is to generate noise-free perfusion maps ( $u(t, x)$ ). Speckle noise  $v(t, x)$  and baseline noise  $\epsilon(t, x)$  are also generated from dose-ranging data, using the  $K$ -coherence algorithm. Perfusion maps are multiplied by normalized speckle noise and baseline noise is added, according to Eq 4.1.

### 4.2.3 Comparison of noise statistics

#### Distribution

An efficient simulation algorithm for DCE-US should produce data with a statistical distribution similar to that of experimentally acquired data. To assess this characteristic, the distance between the distributions of simulated and experimental DCE-US data was measured.

Many different measurements of the divergence between two statistical distributions  $p_1$  and  $p_2$  exist. The squared Hellinger distance was used [101]. It presents the advantage of being symmetric and is defined as follows:

$$D(p_1, p_2) = H^2(p_1, p_2) = \int_{-\infty}^{+\infty} (\sqrt{p_1(t)} - \sqrt{p_2(t)})^2 dt \quad (4.2)$$

The simulation results and the dose-ranging data are thus compared by computing the distance between the histogram of the simulated contrast echo-power and that of the dose-ranging contrast echo-power-data. For the simulated data,  $300 \times 300$  pixels were taken into account. For the experimental dose-ranging data, pixels were extracted from the same area as the sample in the 39 images that were not used to generate the data ( $31 \times 101 \times 39$  pixels). The distances obtained were compared with those obtained with the parametric simulation method: the squared Hellinger distance of the obtained Gamma distribution to the dose ranging distribution was calculated.

#### Spatial correlation

The spatial correlation of each image was characterized by its autocorrelation. The granular appearance characteristic of experimentally acquired DCE-US images suggests that simulated contrast echo-power values should be correlated with their neighborhood. In order to assess the spatial correlation of the simulated noise, its autocorrelation  $AC_{KCoher}$  is computed and compared to the autocorrelation functions of the dose-ranging data  $AC_{DR}$ . Considering that the noise is stationary in space, one can estimate the dose-ranging autocorrelation by computing the autocorrelation of the image, and considering that the noise is stationary in time, this estimation was refined by taking the mean of the autocorrelation functions  $AC_{DR,k}$  with  $k \in \{1, \dots, 39\}$  on the 39 images. The values of the simulated and real autocorrelation functions were compared in a  $20 \times 20$  pixels neighborhood to assess the similarity of the spatial correlation between simulation and experimental data. The mean of the sum of squared (MSD) differences between the autocorrelation of the simulated noise and the autocorrelation of the dose-ranging samples ( $MSD_{KCoher/DR}$ ) was computed. The values obtained were compared to those obtained between experimental data and the parametric model ( $MSD_{Param}$ ) and to the variance of the experimental autocorrelation function ( $MSD_{DR Var}$ ) itself, which gives an idea of the variation of the autocorrelation function occurring experimentally:

$$MSD_{KCoher/DR} = \sum_{i,j} (AC_{KCoher}(i, j) - AC_{DR}(i, j))^2 \quad (4.3)$$

$$MSD_{Param} = \sum_{i,j} (AC_{Param}(i, j) - AC_{DR}(i, j))^2 \quad (4.4)$$

$$MSD_{DR Var} = \sum_{i,j} var(AC_{DR,k}(i, j)) \quad (4.5)$$

## 4.3 Results

### 4.3.1 Distribution

Concentration (microbubbles/mL)	$D(p_{DR}, p_{example\ based})$	$D(p_{DR}, p_{param})$	Improvement (in %)
0	$2.4 \times 10^{-3}$	$4.8 \times 10^{-1}$	99%
$2 \times 10^4$	$7.3 \times 10^{-2}$	$1.4 \times 10^{-1}$	47%
$4 \times 10^4$	$6.0 \times 10^{-2}$	$1.7 \times 10^{-1}$	64%
$8 \times 10^4$	$3.2 \times 10^{-2}$	$2.4 \times 10^{-1}$	86%
$2 \times 10^5$	$1.1 \times 10^{-2}$	$3.2 \times 10^{-1}$	96%
$4 \times 10^5$	$1.1 \times 10^{-2}$	$3.2 \times 10^{-1}$	96%

Table 4.1: Comparison of the squared Hellinger distances between the dose-ranging (DR) data distributions and simulated data generated using two methods : the example-based texture generation method and the parametric method.

For all the concentrations, the squared Hellinger distance is lower for the example-based texture generation than for the parametric method.

The performance of the parametric method depends on the concentration in contrast agent: the best results were obtained when there was no contrast agent, which correspond to the simulation of the baseline noise. When non-zero concentrations of contrast agent are modelled, the noise distribution of the simulation diverges from that of experimental measurements. However, the distance increases as simulated concentration increases.

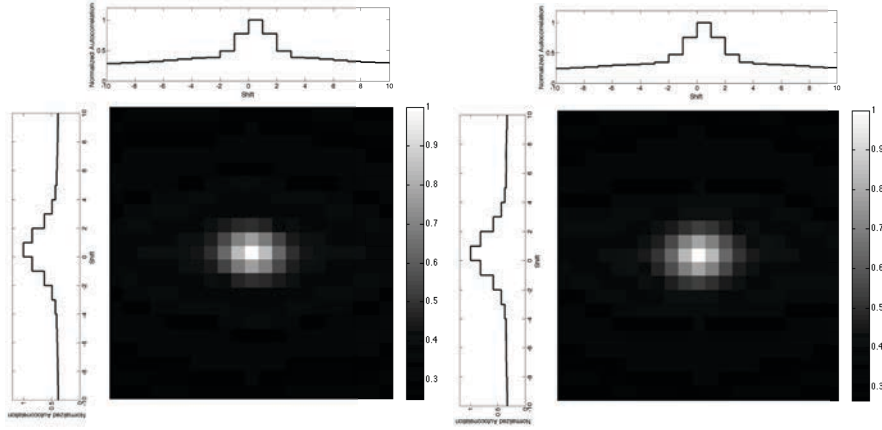
The example-based generation method follow the inverse tendency: for non-zero concentrations of contrast agent, the distance decreases when the concentration increases.

### 4.3.2 Spatial correlation

Concentration (microbubbles/mL)	$MSD_{DRvar}$ (A.U)	$MSD_{Simu/DR}$ (A.U)	$MSD_{Param}$ (A.U)
0	0.68	0.55	93.97
$2 \times 10^4$	0.65	4.77	33.30
$4 \times 10^4$	0.46	1.59	43.46
$8 \times 10^4$	0.47	0.14	55.32
$2 \times 10^5$	0.42	0.25	67.56
$4 \times 10^5$	0.26	0.63	72.25

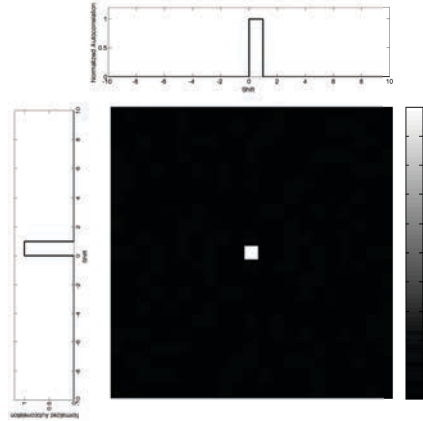
Table 4.2: Comparison of the mean squared difference between the experimental spatial autocorrelation and the two noise simulation methods.

For each contrast agent concentration, the mean squared difference of the experimental autocorrelation function with the autocorrelation function of uncorrelated noise ( $MSD_{Param}$ ) and of noise generated



(a) dose-ranging noise autocorrelation

(b) example based noise autocorrelation

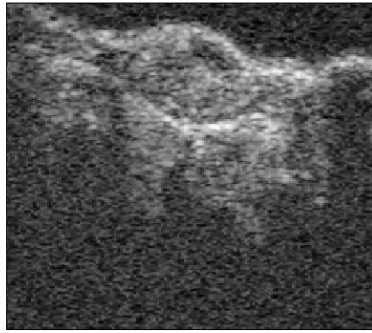
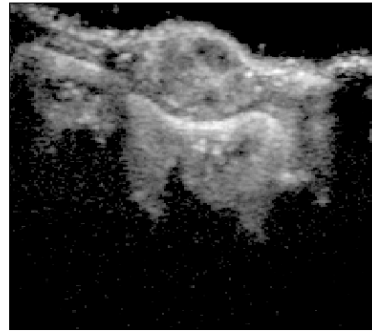


(c) Random noise autocorrelation

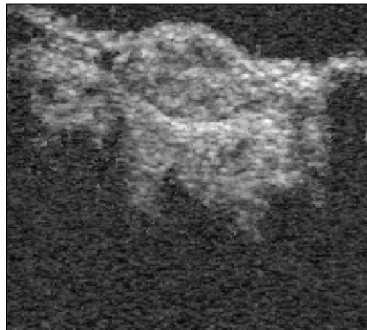
Figure 4.3: Noise spatial autocorrelation functions are displayed. (a) dose-ranging data ( $8 \times 10^{-4}$  *microbubbles/mL*), (b) noise generated using the *K*-coherence example-based texture generation technique, (c) random noise generated without spatial autocorrelation. On the left and above the images are the profiles of the autocorrelation functions along respectively the *y* axis for a 0 shift in *x* and along the *x* axis for a 0 shift in *y*

using the example-based method ( $MSD_{Simu/DR}$ ) are compared. The variance of the experimental autocorrelation function is also given ( $MSD_{DRvar}$ ). Results are presented in Table 4.2. In addition, the spatial autocorrelation functions of the experimental data, of uncorrelated noise and of noise obtained with the example-based method for the  $8 \times 10^4$  *microbubbles/mL* concentration, are displayed in Figure 4.3. The mean squared difference is superior to the natural variance of the autocorrelation, for all concentrations. The difference between the new simulation method and the experimental data is of the same order as the variance of the autocorrelation function. This means that the difference between simulation and experimental data is comparable to the difference between a single acquisition and the estimated experimental autocorrelation function. For non-zero concentrations of contrast agent, the spatial correlation of the data simulated with the *k*-coherence algorithm best corresponds with that of the dose-ranging data for comparisons made at  $8 \times 10^4$  *microbubbles/mL* which was the concentration used to generate the noise texture pattern.

### 4.3.3 Example of DCE-US sequence simulation

(a) Experimental *in vivo* data

(b) Perfusion map (denoised data)



(c) Simulated image

Figure 4.4: Images at  $t = 60$  s from an (a) *In vivo* DCE-US sequence, (b) perfusion signal before its combination with speckle and background noise and (c) Image from simulated DCE-US sequence

The algorithm of simulation presented in Section 4.2.2 was tested by simulating a DCE-US sequence. To do so, an *in vivo* sequence of DCE-US, acquired with the same imaging system as the dose-ranging data, was used. The images were acquired after injection of a bolus of 100  $\mu\text{L}$  of Luminity (Bristol-Myers Squibb) contrast agent to image tissue in a subcutaneous murine pancreatic tumor. The sequence contained 72 images, acquired at 4 images/s. Using the algorithm summarized in Figure 4.2, perfusion data were first extracted using low pass filtering (in the temporal dimension). Then, the baseline of the image was subtracted. In the resulting denoised perfusion image (Figure 4.4 (b)) the gray level intensity is proportional to the concentration-dependant echo-power at each pixel. Generated background and contrast noise were then combined with the perfusion information according to Eq (4.1). Seventy-two speckle-noise and baseline-noise images were simulated, respectively, from the dose-ranging images at 0 microbubbles/mL to  $8 \times 10^4$  microbubbles/mL concentrations. These were combined with the perfusion maps to obtain a simulated DCE-US sequence. The whole simulation process took about 1 hour on a basic desktop computer (Intel Core 2 CPU, 2.66 GHz x 4, 3.8 Go). The simulation of each noise texture of  $364 \times 252$  pixels took 25 s.

An image from the simulated sequence is presented in Figure 4.4, with the corresponding original

image and perfusion data. Qualitatively, it seems that the characteristics of the DCE-US image are preserved. This similarity is present for all the images of the sequence.

## 4.4 Discussion

The  $K$ -coherence algorithm that has been chosen to simulate the noise is not the most recent example-based texture generation algorithm [102]. However, it has several advantages. It is easy to implement and understand. It preserves the distributions: Table 4.1 shows that the distance between the distributions of the simulated data are very close to those of the original data, as compared to a parametric method. The spatial correlations of the obtained images are close to that of the original images as summarized in Table 4.2.

Speckle noise is generated using dose ranging data at a single concentration (here  $8 \times 10^4$  microbubbles/mL). That means that the distribution of the signal at this concentration is assumed to well represent that for all the concentrations in the simulated sequence. This is a very strong assumption, but the results show satisfactory distribution and correlation similarity with experimental data at all the tested concentrations. Therefore, the use of data acquired for a single concentration of contrast agent for the generation of the speckle term at all the concentrations seems acceptable. Future development could consist in finding a way to use the whole range of concentrations of the dose-ranging data to simulate more realistically the signal distribution for the entire range of contrast agent concentrations, for instance by using spatial interpolation techniques.

The effect of the attenuation encountered in DCE-US data on the noise is not simulated by the method presented here. The hypothesis is made that the distribution of the noise is independent of the depth. This assumption is clearly not true, in particular when the concentration of contrast agent is high. One should account for the attenuation in the perfusion data by applying an attenuation term depending on depth before incorporating the noise. However, this is automatically taken into account when the perfusion signal is extracted from real DCE-US sequences.

One of the potential applications of this method is the simulation of data sets for evaluation of motion compensation techniques. It is possible to artificially introduce known motion or deformation on the perfusion data, before the combination with noise. Because the true perfusion would be known, it would then be possible to quantify the improvement in quantification performance made with the motion compensation algorithm. Another potential application is the evaluation of the robustness of perfusion quantification parameters in the presence of noise. Again, because the true perfusion would be known, it would be possible to evaluate the error made because of the noise.

The generation of the DCE-US textures is based on dose-ranging data. This is both an advantage and a drawback of the method. It is an advantage because it is virtually possible to simulate data from any DCE-US imaging system and contrast agent, without having to consider the process of image formation. It is a drawback because in order to be able to simulate ultrasound imaging system in a specific configuration, dose-ranging data have to be available or must be acquired.

## 4.5 Conclusion

A framework for the simulation of DCE-US data has been proposed. It is based on a realistic modelling of DCE-US data and on the use of an example-based texture generation method. The quality of the simulated noise has been assessed and shown to be close to real DCE-US data in terms of the distribution and spatial correlation. The method has been tested to simulate a perfusion sequence from real perfusion data.

Contrary to the methods developed by [97] or [103], the simulation method proposed does not aim to realistically simulate the underlying physics of DCE-US data. However, its flexibility, the possibility that it offers to simulate complex perfusion patterns, and the realism of the obtained data in terms of spatial correlation and data distribution could make it very useful for the initial validation or comparison of registration, segmentation, or quantification algorithms.

## 4.6 Acknowledgements

The BR38 microbubbles were kindly provided by Bracco Suisse SA.

## Chapter 5

# Automatic motion estimation using flow parameters for dynamic contrast-enhanced ultrasound<sup>1</sup>

### 5.1 Introduction

As presented in Chapter 2, several factors affect functional flow quantification, such as attenuation from tissue and microbubbles [47] or scanner settings [46, 48]. Motion, due to respiration or probe movements, is another major cause of variability in the estimation of flow parameters from echo-power curves. To limit the effects of motion on quantification, several approaches are possible, as presented in Chapter 2: asking the patient to hold his or her breath during the acquisition, use of gating techniques or registration techniques.

The two key challenges of registration are 1) to identify a robust and efficient similarity criterion and 2) to define the reference with respect to which all other images in the sequence will be registered. Due to the low contrast-to-noise ratio and the lack of stable landmarks in harmonic imaging sequences, selection of the reference image is difficult in DCE-US. Currently, mostly rigid registration techniques have been proposed to meet the challenge of DCE-US sequence registration.

In this work, the contrast uptake information is taken into account in order to make the registration more accurate, more precise and operator independent. Some authors have developed methods that include the estimation of flow-parameters in the registration of DCE-MRI sequences. Bhsushan et al. [104] combined motion estimation and flow-parameters estimation in a unified probabilistic framework. Adluru et al. [105] and Buonaccorsi et al. [106] generated a reference sequence using the flow-parameters locally estimated flow parameters and then registered the original sequence with respect to it. However, contrast uptake kinetics have not yet been integrated into techniques for DCE-US sequence registration.

The goal of this work is to design and evaluate a new automatic registration method that combines motion and flow-parameter estimations. An iterative algorithm that successively estimates motion and flow is proposed. A final registration is then performed to refine motion estimation. The results are

---

<sup>1</sup>This chapter is adapted from Barrois, G., Coron, A., Lucidarme, O. & Bridal, L. (2014). Automatic motion estimation using flow parameters for dynamic contrast-enhanced ultrasound. Manuscript in preparation for submission.

compared to those obtained with mutual information based registration on both simulated and 12 DCE-US sequences acquired in patients.

## 5.2 Material and methods

### 5.2.1 Joint motion and quantification estimation: problem formulation

The variable  $f$  denotes a DCE-US sequence of  $N$  frames, and  $f(x, t_n)$  (or  $f_x(t_n)$ ) represents the echo-power at position  $x$  and time instant  $t_n$  with  $n \in [1, \dots, N]$ . The ROA is located at the position  $x$  and the ROA can be as small as a single pixel. To compensate  $f$  for motion, one needs to estimate  $\mathbf{T} = \{T_n\}_{1 \leq n \leq N}$  a set of transformations. So, if the motion is correctly compensated, the sequence of images  $\{f(T_n(x), t_n)\}_{1 \leq n \leq N}$  is still. Let  $u(\theta(x), t_n)$  be a parametric model of flow, for example like the lognormal model, associated with the motion compensated sequence  $f$ , with  $\theta(x)$  the parameters of the model  $u$  at  $x$ . Both  $\mathbf{T}$  and  $\theta(x)$  have to be estimated from  $f$ . This estimation problem is expressed as an optimization problem by maximizing a likelihood.

The linear echo-power  $f(x, t_n)$  can be modelled as the parametric flow model  $u(\theta(x), t_n)$ , corrupted by a multiplicative speckle noise  $v_x$ :

$$f(T_n(x), t_n) = u(\theta(x), t_n)v_x(t_n). \quad (5.1)$$

As in Chapter 3, the noise is described by a gamma distribution with a mode equal to 1 :

$$p_{V_x}(v) = \gamma(v; k, \frac{1}{k-1}) = \begin{cases} v^{(k-1)} \frac{(k-1)^k}{\Gamma(k)} \exp(-v(k-1)) & \text{if } v \geq 0 \\ 0 & \text{if } v < 0 \end{cases} \quad (5.2)$$

According to Eq (5.1), assuming the temporal independence of the noise, the likelihood for the model and the transformation parameters over the analysis region can be written as:

$$\mathcal{L}(\theta, \mathbf{T}) = \prod_{n=1}^N \prod_x p_{F|\theta(x), k, T_n(x)}(f(T_n(x), t_n) | \theta(x), T_n(x)),$$

which can be rewritten, according to Eq (5.1):

$$\mathcal{L}(\theta, \mathbf{T}) = \prod_{n=1}^N \prod_x p_{V_x} \left( \frac{f(T_n(x), t_n)}{u(\theta(x), t_n)} \right)$$

The estimation problem aims to maximize this likelihood. It is equivalent to minimizing the opposite of the log-likelihood. Assuming that the noise follows the gamma distribution of Eq (5.2), the estimation problem can therefore be rewritten as:

$$\arg \min_{\theta, \mathbf{T}} \sum_{n=1}^N \sum_x \left( \log(u(\theta(x), t_n)) + \frac{f(T_n(x), t_n)}{u(\theta(x), t_n)} \right) \quad (5.3)$$

### 5.2.2 Joint motion and quantification estimation: the (M/Q) algorithm

In order to solve this optimization problem, the following strategy is proposed:

- Motion  $\mathbf{T}$  and model parameters  $\theta$  are sequentially, and iteratively estimated until convergence;

```

1 Model_Based_Registration( $N, f, \hat{\mathbf{T}} = \{\hat{T}_n\}_{1 \leq n \leq N}$ )
   Input:  $N$  number of images in the sequence
    $f$  the sequence of images with  $f(x, t_n)$  the echo-power at position  $x$  and instant  $t_n$  ( $1 \leq n \leq N$ )
   Output:  $\hat{\mathbf{T}} = \{\hat{T}_n\}_{1 \leq n \leq N}$  sequence of  $N$  estimated transformations
   /* Initialization */
2  $j \leftarrow 0$ 
3  $\forall n, \hat{T}_n^j \leftarrow 0$ 
4  $f_l \leftarrow \text{low\_resolution}(f)$  /* Spatial-domain smoothing and subsampling */
                                     /* Iterations */
5 while  $j = 0$  or any  $\{\hat{T}_n^j \neq \hat{T}_n^{j-1}\}_{1 \leq n \leq N}$  do
6    $j \leftarrow j + 1$ 
7   update  $\mathcal{P}$  and  $\bar{\mathcal{P}}$  with Eq. (5.4)
8    $\forall x, \theta(x) \leftarrow \arg \min_{\theta} \sum_n \left( \log(u(\theta(x), t_n)) + \frac{f_l(T_n^{j-1}(x), t_n)}{u(\theta(x), t_n)} \right)$  /* Update local flow */
9    $\forall x, n, f_{th}(x, t_n) \leftarrow u(\theta(x), t_n)$  /* Update theoretical contrast sequence */
10   $\forall n, \hat{T}_n^j \leftarrow \arg \min_T \sum_x \left( \log(f_{th}(x, t_n)) + \frac{f_l(T(x), t_n)}{f_{th}(x, t_n)} \right)$  /* Update transformations */
11 end
   /* Final registration */
12  $\forall x, n, f_s(x, t_n) \leftarrow \text{median\_filter}(f(T_n^j(x), t_n))$  /* Time-domain smoothing */
13  $\forall n, \hat{T}_n \leftarrow \arg \min_T \text{mutual\_information}(f_s(x, t_n), f(T(x), t_n))$ 

```

**Algorithm 1:** Joint motion and quantification estimation: the M/Q algorithm

- Because high level of speckle noise for small ROAs in the DCE-US sequence  $f$  and to speed up the process,  $f_l$  a lower resolution sequence associated to  $f$  is introduced: Each  $f_l$  frame is computed by spatially smoothing each image  $f$  with a 2D constant square convolution kernel of width  $W$ , followed by a factor  $W$  subsampling along each direction. As a consequence, the ROAs associated with each voxel of  $f_l$  is a square of  $W \times W$  pixels of  $f$ . Thus, in Eq. (5.3),  $f$  is replaced by  $f_l$  during the iterative process.
- Some regions of the sequence are perfused and some are not. Estimating all flow parameters on non-perfused regions is meaningless. For such regions a dedicated model is considered by fixing the values of some of the flow parameters.

The algorithm is described in Algorithm 1. The main steps are commented below and some implementation details are given in Section 5.2.6.

### Perfused and non perfused ROAs

Perfused tissue spans a limited part of each frame, so the sequence can be divided in two mutually exclusive regions,  $\mathcal{P}$  the set of perfused pixels and  $\bar{\mathcal{P}}$  the set of non perfused pixels.

Analysis regions are classified as perfused ( $\mathcal{P}$ ) or non-perfused ( $\bar{\mathcal{P}}$ ) at each iteration. This classification is done (line 7) by thresholding on the median value of each registered echo-power signal during the

sequence:

$$\begin{cases} x \in \mathcal{P} & \text{if } \text{median\_filter}(f_l(T_n(x), t_n)) > \mathcal{P}_T \\ x \in \bar{\mathcal{P}} & \text{if } \text{median\_filter}(f_l(T_n(x), t_n)) \leq \mathcal{P}_T \end{cases} \quad (5.4)$$

### Functional flow-parameter estimation

At each analysis region  $x$ , the vector of parameters  $\theta(x)$  is estimated (line 8) by minimizing Eq (5.3), with  $u$  the model  $u$  for perfused and non-perfused ROAs. When the model parameter estimation step is completed, a theoretical contrast echo-power sequence  $f_{th}$  is generated by attributing to each analysis  $x$  at each time  $t_i$  the corresponding model value  $u(\theta(x), t_i)$  (line 9).

### Motion estimation

Once a parametric model value has been attributed to each analysis region of the sequence to generate the theoretical sequence, it is possible to optimise Eq (5.3) according to the transformation matrices  $\mathbf{T}$ . Each frame of  $f_l$  is then registered with respect to the corresponding frame of  $f_{th}$  (line 10).

### Final registration

Due to the low signal to noise ratio, flow-parameter estimation and motion estimation are done on a lower resolution version of the sequence. This is enough to compensate for the large amplitude motion due, for instance, to breathing. However there are still some low-amplitude motion artefacts. To refine the motion compensation, a final registration is performed (line 13). In this step, the moving sequence is the original sequence, with echo-power in dB. This sequence is registered with respect to a version of the original sequence (also with echo-power in dB) registered using  $\hat{\mathbf{T}}$  and smoothed in the temporal dimension, designated as  $f_s(x, t_n)$ . The smoothing aims at preserving image features while removing echo-power variations due to residual motion.

The artificial reference sequence generated from the perfusion model  $f_{model}$  is replaced by  $f_s$ , a time smoothed version of the motion-compensated original sequence at the finest resolution. Some smoothing is accomplished by applying a median filter to the sequence. Median filtering is chosen as it is more robust than mean filtering to remove extreme values resulting from motion. Each image of the initial sequence is then registered with respect to the corresponding image in the smoothed sequence. The metric that is optimised is the mutual information, because of its robustness. The resulting transformations  $\hat{\mathbf{T}}$  is the final transform estimation.

### 5.2.3 Reference mutual information registration (MI)

The performance of the registration method proposed in this chapter is compared to a reference image based mutual information registration (MI registration) : in this technique, the whole sequence is registered with respect to a reference image chosen by an expert. The reference image is chosen as the image where the structures of the vascular network are the most visible. The metric that is used is a mutual information metric [107]. A mask that delimits the ROI over which the similarity measurement will be computed is delimited. For the sake of fairness of the comparison, this mask is the same as the mask used in the M/Q method. This reference registration is based on the method proposed in [55].

Other registration parameters are the same as those used for the final registration of the M/Q method (in particular the echo-power is in dB).

### 5.2.4 Simulation of DCE-US data

Simulation of DCE-US data for the validation of the registration method is done according to the method presented in Chapter 4, with the model of signal of Eq.(4.1). The flow signal  $u$  is generated from still *in vivo* sequences, by smoothing them in the time dimension, which also has the consequence to remove residual motion. A triangular periodic motion of 2.4 mm of amplitude in both directions is added to the sequence. The period is respectively 1 s and 0.7 s in  $Y$  and  $X$  directions. A periodic  $\phi = 2^\circ$  amplitude rotation is also added, with a 1 s period. The center of rotation is at the center of the image. With  $\wedge_T$  the triangle function of period  $T$  and of amplitude 1:

$$V_i \begin{pmatrix} x \\ y \\ 1 \end{pmatrix} = \begin{pmatrix} \cos(2\pi\rho \wedge_{1s}(t_i)) & \sin(2\pi\rho \wedge_{1s}(t_i)) & 2.4 \wedge_{0.7s}(t_i) \\ -\sin(2\pi\rho \wedge_{1s}(t_i)) & \cos(2\pi\rho \wedge_{1s}(t_i)) & 2.4 \wedge_{1s}(t_i) \\ 0 & 0 & 1 \end{pmatrix} \cdot \begin{pmatrix} x \\ y \\ 1 \end{pmatrix} \quad (5.5)$$

After addition of the motion to the flow signal, it is combined with noise textures according the model of Eq.(4.1). The resulting sequence presents the advantage to be close to real DCE-US sequences in terms of signal distribution and spatial correlation, as demonstrated in *Barrois et al.* [96], but with known motion. The important steps of the generation of moving DCE-US sequences are summarized in Figure 5.1. The difference with the diagram in Chapter 4 is that motion  $V$  is added to  $u(t)$  before the combination with the noise texture. A total of 27 different sequences were generated.

### 5.2.5 Clinical DCE-US data

Clinical DCE-US data were acquired using an Aixplorer (Supersonic imagine, Aix-en-Provence) ultrasound clinical imaging system in contrast mode and a SL10-2 probe 2-10MHz, with mechanical index fixed a low level. A bolus of SonoVue<sup>®</sup> (Bracco SpA, Milan, Italy) was injected intravenously and a contrast sequence was acquired during 35-50 s. 12 sequences were analysed in this study.

### 5.2.6 Implementation of the registration algorithms

#### $\mathcal{P}_T$ the threshold of perfused and non-perfused regions

The value  $\mathcal{P}_T$  of the threshold is selected as 300% of the median value of the first image of the sequence: at this time, no contrast agent has penetrated the tissue yet, therefore the median is representative of non perfused tissue.

#### Flow model

To be applied, the model based registration necessitates the specification of a flow model. In this work, because the available data are from bolus injections of contrast agent, the parametric model that was used to fit the echo-power data curves was the lognormal model for a bolus, presented in [69]:

$$u(\theta(x) = (m(x), s(x), c(x), A(x)), t) = A(x) \frac{\exp \frac{-[\log t - m(x)]^2}{2s(x)^2}}{\sqrt{2\pi}ts(x)} + c(x) \quad (5.6)$$

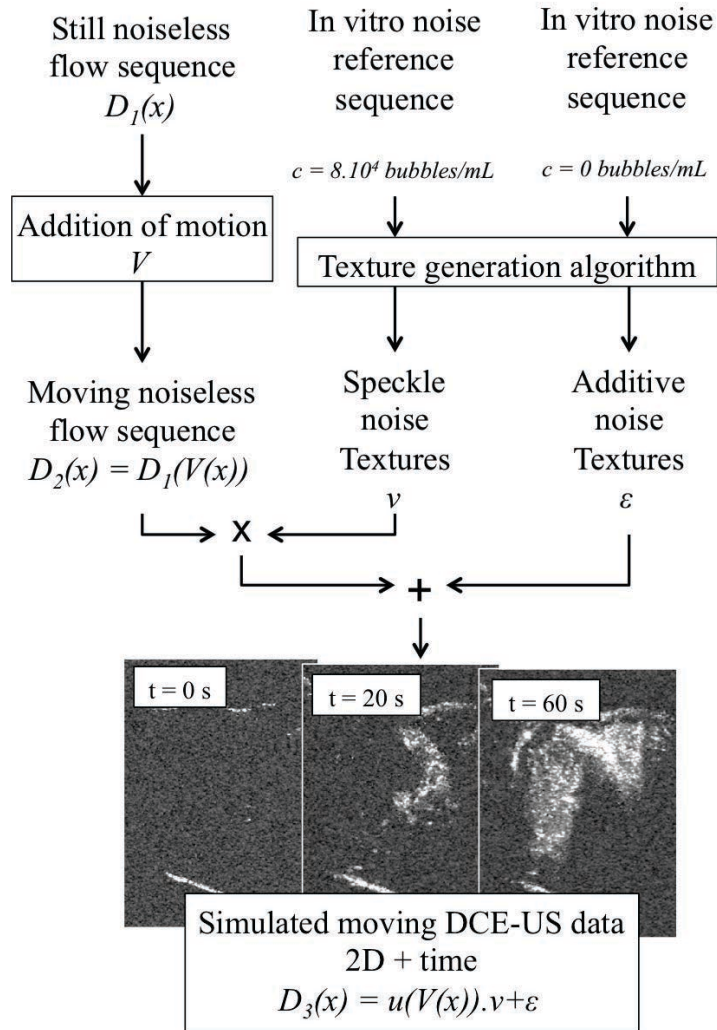


Figure 5.1: Important steps of the simulation algorithm used to simulate moving DCE-US sequences to evaluate the registration algorithms.

with  $m$  the mean of the underlying normal distribution,  $s$  the standard deviation of the underlying normal distribution,  $c$  the offset to take into account the fact that the echo-power is not zero when the concentration of microbubbles is zero and  $A$  a scaling parameter. At each perfused analysis region  $x$ , the vector of parameters  $\theta(x) = (m(x), s(x), c(x), A(x))$  is estimated by minimizing Eq (5.3) with  $u$  the lognormal model. Because, by definition, non-perfused analysis regions should present a constant value for  $u$  with time, the parametric model  $u(\theta(x), t_i)$  must be constant. This can be implemented by forcing the parameter  $A$  to be zero. In this case:

$$\forall t_i, \forall x \in \bar{\mathcal{P}}, u(\theta(x) = (m(x), s(x), c(x), 0), t) = c(x).$$

### Lower resolution sequence

For DCE-US data, for a correlation radius defined as the distance at which image autocorrelation becomes lower than 50% of its maximum, it has been observed in [96] that it is higher than 0.15 mm. Kuenen et al. [108] also reported distances on this order using other ultrasound imaging systems. Considering this, a subsampling ratio of 3 provide a reasonable compromise between processing speed and loss of spatial information.

### Stopping condition

Due to the presence of the final registration and of the subsampling, some stopping conditions (line 5 of Algorithm 1) for the model based registration have to be chosen in order to limit the number of iterations to a low number. Practically,  $tx_T$ ,  $ty_T$  and  $\theta$  are fixed to limit the number of iterations to three in most cases.

### Median filtering

A 20 second window was chosen based on empirical tests: the smoothing window must be large enough to remove the components due to motion, which are generally at low frequencies.

### Registration software

The algorithms presented above were implemented using the open source software package elastix, developed by Klein et al. [109]. The software was modified to implement the metric presented in 5.3. Mutual information metric implementation used was the Advanced Mattes Mutual Information Metric [110]. The software was integrated in a Matlab wrapper, ElastixFromMatlab<sup>©</sup> (CNRS and Riverside Research) . For all the registration methods, a multi-resolution scheme and an adaptive stochastic gradient descent method was used to find the optimal registrations.

### Theoretical sequence generation

When the model parameter estimation step is completed, a theoretical contrast echo-power sequence is generated, by attributing to each analysis region  $x$  at each time  $t_n$  the corresponding model value  $u(\theta(x), t_n)$ . This theoretical sequence will be used for the estimation of motion.

### 5.2.7 Comparison of the methods

#### Simulated data

For all the sequences, a ROI was selected around the tissue of interest. If the motion is perfectly estimated, the true transformation  $V$  and the estimated transformation  $\hat{T}$  should compensate up to a constant rigid transformation:

$$\forall i, V_{t_i} \circ \hat{T}_{t_i} = T_{const} \quad (5.7)$$

Therefore, when  $\hat{T}$  and  $V$  are applied successively,  $V_{t_i} \circ \hat{T}_{t_i}(ROI) = ROI_{t_i reg}$  should be as still as possible because ideally:

$$\forall i, ROI_{t_i reg} = T_{const}(ROI) \quad (5.8)$$

Thus, to assess the quality of the registrations, two measures of the stability of  $ROI_{t_i reg}$  in the sequence are proposed. First, the Dice coefficient measures for each frame how well the ROI is superimposed with a reference ROI. The transformation applied to this ROI is therefore assumed to be subject to the constant transformation  $T_{const}$ :

$$\text{with } ROI_{t_{ref}} = \hat{T}_{t_{ref}}(ROI), \quad (5.9)$$

$$\forall t_i, \text{Dice}(t_i) = \frac{|2 \cdot (ROI_{t_i reg} \cap ROI_{t_{ref}})|}{|ROI_{t_i reg}| + |ROI_{t_{ref}}|} \quad (5.10)$$

The second measure is the Hausdorff Distance to the same reference ROI:

$$\forall t_i, \text{Hausdorff}(t_i) = \max\left(\sup_{x \in ROI_{t_{ref}}} \inf_{y \in ROI_{t_i reg}} d(x, y), \sup_{x \in ROI_{t_i reg}} \inf_{y \in ROI_{t_{ref}}} d(x, y)\right) \quad (5.11)$$

The reference frame  $t_{ref}$  is chosen as the reference frame in the MI registration.

Finally, the echo-power data curves are also extracted from the sequences registered with the two methods and from the original sequence without motion. The sum of squared differences SSD between the logarithm of the echo-power data curves of the perfectly registered sequence and of the sequence registered using the two methods are compared:

$$\text{SSD} = \frac{1}{N} \sum_{x \in ROI} (\log(\text{mean}_{x \in ROI}(D_3(\hat{T}(x))) - \log(\text{mean}_{x \in ROI}(D_1(V \circ \hat{T}_{t_{ref}}(x))))^2 \quad (5.12)$$

Because of the multiplicative nature of the noise, the SSD was not computed directly on the contrast echo-power curves but on their logarithm to make the noise satisfy additive and homoscedastic conditions.

#### *In vivo* data

Comparison of *in vivo* results is made difficult by the fact that the "true" motion is unknown. In order to assess the quality of the registration obtained via the MI and M/Q algorithms, a manual registration was performed by an expert, and considered as the ground truth. The Hausdorff Distance, Eq. (5.11) and the Dice coefficient, Eq. (5.9) were computed, but with  $V$  replaced by the manual registration  $T_{manual}$ .

**Manual registration** Manual registration was performed using a program developed for this purpose. A reference image is first selected by the user. The expert can move forward and backward in the sequence to select an image (current image) to be aligned with the reference image. Each image displayed with

the reference image overlaid: the overlaying is accomplished by linearly combining the intensities of the current image and the reference image, with a weight respectively of  $\alpha$  and  $1 - \alpha$ , with  $\alpha \in [0, 1]$ . The expert can apply translation and rotation to the current image in order to align it with the reference image. When the alignment between the current image and the reference image is judged satisfactory, the expert can save the transformation, mark the current image as "registered" and select a new current image.

Because the motion in the sequence is mainly due to breathing, it is mostly a succession of uniform motions in one direction (inhalation and exhalation phases, sometimes still phases). Therefore the strategy adopted by the expert was as follow: first the extreme images at the beginning and the end of uniform motion phases were identified and manually registered. For the images in-between, the program automatically computed the motion as a linear interpolation of the extreme image transformations. When the motion between the extreme images was truly uniform, no further alignment was required. To assess whether the interpolated motion was satisfactory, the expert reviewed the entire sequence. If movements were still present, the expert aligned manually the remaining non-aligned images with the reference image.

When the manual registration was finished, the program provided the obtained transformation for all the images of the sequence.

## 5.3 Results

### 5.3.1 Assessment of accuracy in calibrated-movement sequences

MI and M/Q registration algorithm were applied to the 27 simulated sequences. Figure 5.2 shows a box-plot of the distribution of the different metrics used to compare the registration results for the simulations. Figure 5.2 (a) shows  $SSD_{curves}$  for the two registration methods. It is significantly lower ( $p < 0.05$ , Mann Whitney U-test) with the M/Q registration method than with the MI registration method. Similarly, the Hausdorff distances are significantly lower with the M/Q registration as shown in Figure 5.2 (b). Finally, the Dice criteria is significantly higher with the M/Q registration method Figure 5.2 (c).

### 5.3.2 Registration performance with respect to manual expert registration in DCE-US sequences acquired in patients

Table 5.1 shows the results for the registration of the 15 clinical sequences. The pathology associated with each sequence is given. The mean Dice coefficients and Hausdorff distances with their standard deviations along the sequence are computed. For 80% of the sequences, the mean Dice coefficients are higher and the mean Hausdorff distances are lower for the M/Q method than for the MI registration. For 87% of the sequences, the standard deviation of the two measurements are lower along the sequence with the M/Q method than with the MI registration.

## 5.4 Discussion

Results obtained on simulated data show that the M/Q method retrieves the motion better than the MI method. The method that has been used to simulate the sequence is not based on parametric assumptions

Sequence	Condition	Method	Dice (%)		Hausdorff (mm)	
			mean	std	mean	std
1	Hepatic tumour	M/Q	<b>89.0</b>	<b>8.1</b>	0.22	<b>0.17</b>
		MI	88.7	10.0	0.22	0.23
2	Neuroendocrine metastasis	M/Q	<b>91.4</b>	9.3	<b>0.33</b>	0.40
		MI	90.8	<b>8.9</b>	0.35	<b>0.36</b>
3	Abdominal scan	M/Q	88.7	<b>6.6</b>	0.26	<b>0.15</b>
		MI	<b>91.0</b>	8.1	<b>0.21</b>	0.17
4	Fast Angioma	M/Q	<b>92.2</b>	<b>6.0</b>	<b>0.19</b>	<b>0.13</b>
		MI	90.3	6.0	0.24	0.23
5	Cylindroma hepatocyte	M/Q	<b>72.7</b>	<b>25.7</b>	<b>0.49</b>	<b>0.49</b>
		MI	58.7	33.5	0.74	0.59
6	Hepatic tumour	M/Q	<b>84.5</b>	<b>13.3</b>	<b>0.33</b>	<b>0.28</b>
		MI	72.5	20.2	0.63	0.46
7	Hepatocellular carcinoma	M/Q	69.9	<b>18.4</b>	0.51	<b>0.33</b>
		MI	<b>77.2</b>	22.1	<b>0.38</b>	0.43
8	Cholangiocarcinoma	M/Q	<b>88.3</b>	<b>18.2</b>	<b>0.40</b>	<b>0.66</b>
		MI	85.6	21.0	0.51	0.78
9	Hepatic tumour	M/Q	<b>90.0</b>	<b>5.1</b>	<b>0.25</b>	<b>0.13</b>
		MI	81.2	11.8	0.47	0.30
10	Kidney metastasis	M/Q	<b>91.4</b>	<b>5.4</b>	<b>0.24</b>	<b>0.16</b>
		MI	84.4	10.7	0.44	0.29
11	Abdominal scan	M/Q	85.4	7.8	0.35	0.18
		MI	<b>90.9</b>	<b>5.7</b>	<b>0.23</b>	<b>0.13</b>
12	Thyroidic metastasis	M/Q	<b>92.7</b>	<b>4.4</b>	<b>0.21</b>	<b>0.12</b>
		MI	88.9	10.1	0.32	0.26
13	Hepatic tumour	M/Q	<b>93.7</b>	<b>5.4</b>	<b>0.23</b>	<b>0.17</b>
		MI	92.0	7.4	0.28	0.23
14	Suspect Nodule	M/Q	<b>85.5</b>	<b>8.1</b>	<b>0.33</b>	<b>0.17</b>
		MI	81.1	8.1	0.42	0.25
15	Cholangiocarcinoma	M/Q	<b>63.0</b>	<b>19.6</b>	<b>0.73</b>	<b>0.29</b>
		MI	62.9	34.1	0.70	0.67

Table 5.1: Individual results for each of the 15 clinical DCE-US sequences. For each sequence, the best results for mean and standard deviation of Dice criterion and Hausdorff distance are in bold.

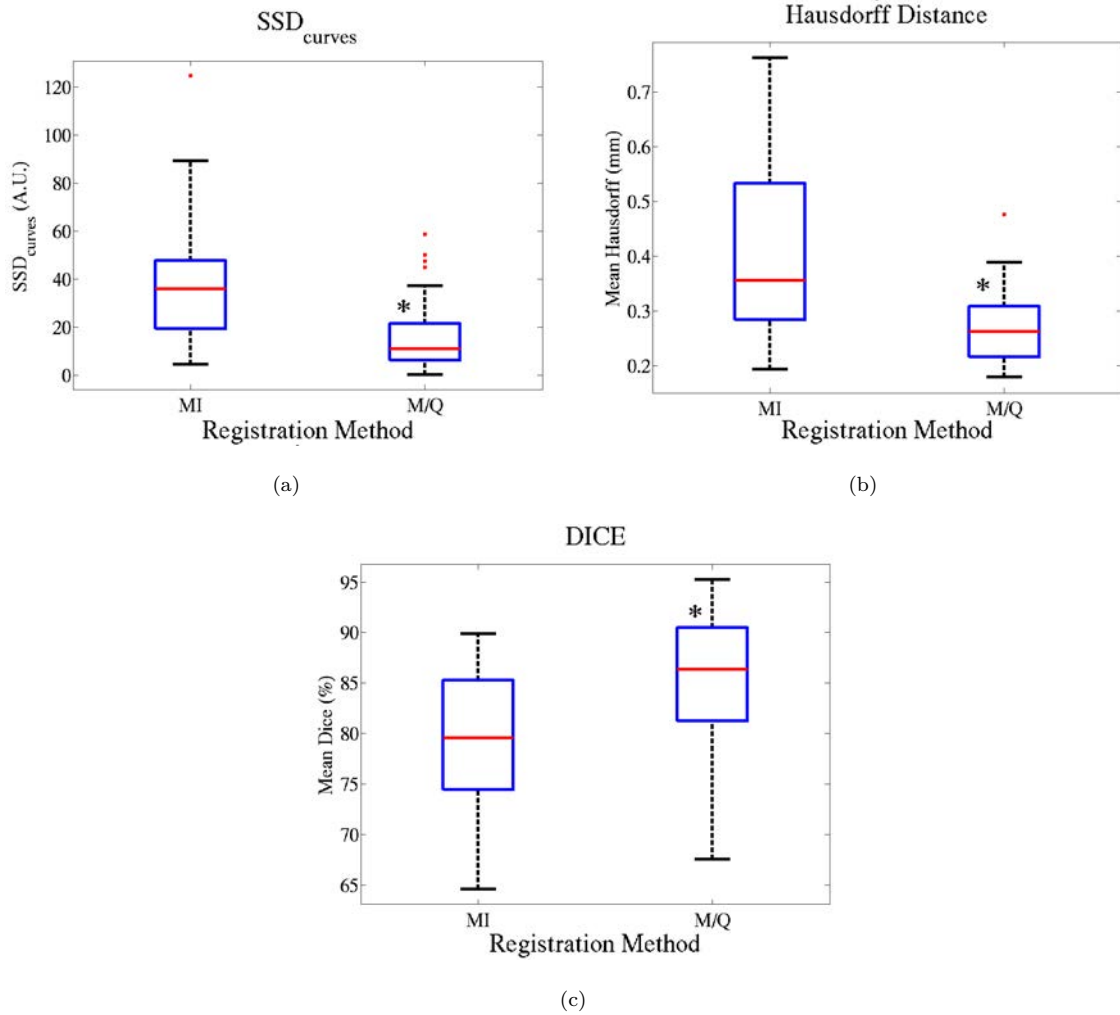


Figure 5.2: Boxplots of the distribution of the results for simulated sequences, for three criteria. a)  $SSD_{curves}$  b) Hausdorff distance c) DICE coefficient

about the distribution of the noise or the dynamic of the contrast agent, but based on experimentally acquired data. Therefore, the simulations are not biased toward the M/Q method in any way.

The results in Table 5.1 show that the standard deviation of the Hausdorff distance and of the Dice criterion along the sequence are lower for the M/Q method than for MI in a majority of the cases considered. The lower standard deviation observed with the M/Q method suggests that the quality of the registration is more uniform along the sequence. This is an important feature, because large registration errors can cause large variations in the echo-power data curves, which in turn can lead to large variations in the model fit. The sequences where the MI method performs better than the M/Q method are sequences where the motion to handle is not only periodic, for instance with a shift in the average position of the tissue of interest between the beginning and the end of the sequence. In this case, the parametric model estimation can fail to find accurate vector of parameters  $\theta$  at some location, leading to a less precise registration. This could be handled by applying a quick preliminary registration with respect to a reference image.

The M/Q method have been tested and compared to MI on data with bolus injection of contrast agent, using a lognormal parametric model of perfusion. However, the M/Q registration is virtually compatible

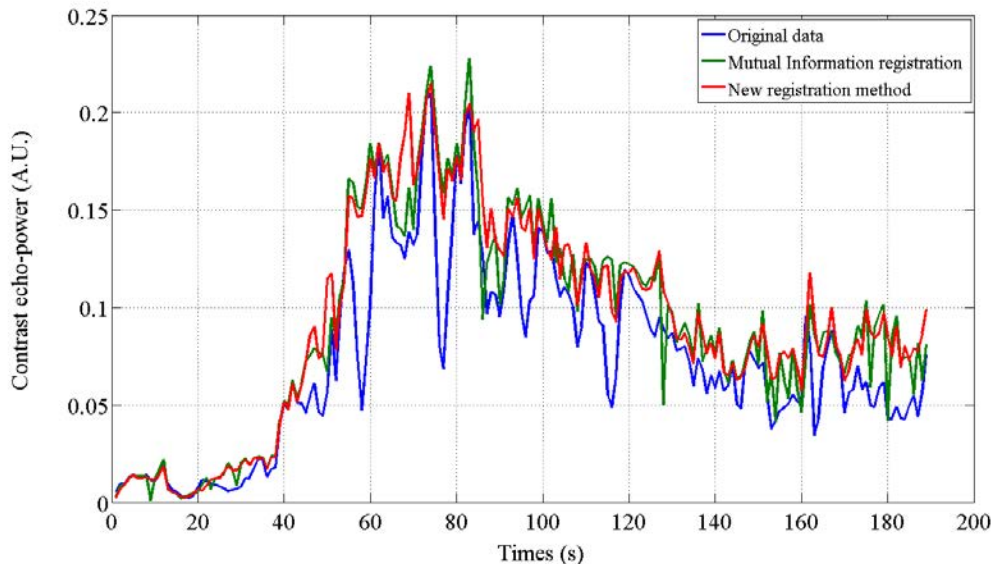


Figure 5.3: Example of echo-power data curves extracted from data acquired *in vivo* in a tumor. Curves are presented before registration, after MI registration and after M/Q registration.

with any type of parametric models and input function modulation (bolus, destruction-replenishment). Even non-parametric models such as smoothing splines could be used, as long as they are robust enough to filter the large temporal variations due to motion.

The M/Q method has been compared to the MI method because it is commonly used. It could be of interest to compare the M/Q method with techniques that call on both B-mode and contrast mode images for registration. Such dual-mode methods have been demonstrated to retrieve the motion better than methods using only the B-mode or contrast-mode images [57]. However, they necessitate dual display availability and perfect synchronization between the two imaging modes.

By definition, registration techniques cannot handle out-of-plane images. The choice of rigid transformation is made to prevent over-register the sequence by the method. Using this method, out-of-plane images are still detectable and can be removed from flow estimation when identified. Further work could consist in investigating whether out-of-planes images result in detectable variations in the registration metric that could be identified and used to remove non-relevant images from quantification.

Because model fitting is, in a sense, a smoothing algorithm, one could wonder why a median filter is applied in the final registration rather than another fitting step at a finer scale (without sub-sampling) to obtain the new artificial reference sequence. The main reason is that model fitting is based on strong assumptions about the kinetics of contrast agent in the tissue and is, therefore, a very coarse smoothing. It is thus very efficient to remove strong variations such as the ones caused by breathing motions. However, it may also remove "natural" variations, not due to motion, that are useful for registration. Moreover, fitting a parametric model to each pixel would take a long time, whereas median smoothing is fast (less than 10 s to smooth the whole sequence).

The development of 3D ultrasound imaging will require the development of adapted registration methods. This method is easily transportable to 3D by extracting echo-power data curves from 3D analysis regions. Moreover because out-of-plane motion does not exist in 3D, one could imagine using a

more flexible transform space to obtain more accurate registration.

## 5.5 Conclusion

A new completely automatic method that uses flow information to estimate motion in DCE-US is developed. By using a realistic model of noise for DCE-US signal, the two estimation problems are formulated in one. Solutions to the problem are estimated using two steps, a first iterative step to filter low frequency motions and a final registration step which aims to remove higher frequency motions. The method demonstrates a better ability to estimate artificially added motion on simulated data sequences than a mutual information registration. It also exhibits better matching with a manual registration performed by an expert on *in vivo* acquired sequences.

By removing operator-dependent selection of a reference image, this method will renders flow parameter estimation more reproducible and non-operator-dependant. Moreover, the improvement in the quality of motion estimation that is demonstrated should make flow parameter estimation more accurate and precise. In particular, it could allow a more accurate local quantification, which is of interest to better reveal the local heterogeneity of the flow.

# Chapter 6

## Dynamic clustering<sup>1</sup>

### 6.1 Introduction

It has been suggested [12] that drugs normalizing tumour vascular network could enhance the delivery efficiency of conventional cytotoxic therapies (see Chapter 1). Anti-angiogenic therapy can contribute to the normalization of the vascular network. Methods able to detect changes in vascular network structures are therefore desirable to monitor how they change throughout the tumor during anti-angiogenic therapy [111].

As presented in Chapter 2, flow quantification using DCE-US is based on the analysis of the contrast echo-power data curves. Because the signal to noise ratio of DCE-US images can be low at some time points, the curves are generally extracted from a ROA that includes the entire tumor ROI. This provides spatial averaging of the signal and effectively decreases the noise level. In most studies, ROIs are drawn manually by an expert around the tissue of interest [10, 79, 112]. This approach has two main drawbacks: first, it renders the analysis operator-dependant. Second, the tissue of interest may be heterogeneous in terms of perfusion. Thus, averaging the signal over the whole tissue causes a loss of spatial information, and small capillary flows can be masked by high intensity flows coming from large vessels.

Several possibilities exist to overcome these issues. First, rather than extracting the signal from the entire ROI around the whole tumour, it is possible for the expert to draw several ROAs, delimiting, for instance, a peripheral and central zone of the tumour. ROAs can also be selected to separate regions that appear more or less enhanced on the initial contrast sequences. However, these approaches are operator-dependant and may rely on *a priori* assumptions about the perfusion in the selected zones. Moreover, the expert may miss spatial heterogeneity when drawing the ROAs. It is also possible to analyse signal from small ROAs in the ROI, of typically less than one square millimetre [68, 76, 113], to obtain local values for the flow parameters, and compute parametric maps. However, this approach requires robust analysis methods and, due to the large variability of individual, local estimations, parametric maps are often only qualitatively used in studies. A more desirable analysis method would provide operator-independent and quantitative indicators, that incorporate spatial information.

In this chapter, a method that was initially developed by Y. Rozenholc (MAP5 UMR CNRS 8145, University Paris 5) to group statistically-related perfusion from small ROAs of DCE-CT and DCE-MRI

---

<sup>1</sup>This chapter is adapted from Barrois, G., Coron, C., Dizeux, A., Rozenholc, Y. & Bridal, L. (2014). Manuscript in preparation for submission.

data is adapted to cluster highly-local ROAs together based on the shape of echo-power data curves from DCE-US sequences. The adaptations made to the method for analysis of DCE-US are described. The specificity and the sensitivity of the method are evaluated and compared to those of a more conventional clustering technique on a simulated data set. The relevance of the clusters identified is qualitatively assessed using data acquired in the kidney *in vivo*.

## 6.2 Material and method

### 6.2.1 Conventional technique: K-means clustering

K-means clustering is an iterative method to find clusters and their cluster's centers in data [88]. It is used in many image processing and data analysis applications, such as images segmentation [114] or classification of times series [115, 116], and is at the foundation of numerous image analysis methods.

In this study, K-means is applied on a simulated dataset and results are compared to those obtained using the DynClust algorithm. Prior to application of the clustering algorithm, principal component analysis is used to reduce the dimensions of the data set.

The **dimension reduction** phase works as follows: each enhancement vector at each location is considered as an observation, represented in a space of dimension  $N$ . The output of principal component analysis applied on the ensemble of  $M$  observations is an orthonormal basis of  $N$  vectors  $(c_1, \dots, c_N)$ , with associated eigenvalues  $(\lambda_1, \dots, \lambda_N)$ . Each vector is a linear combination of the  $N$  original dimensions. The eigenvalues correspond to the amplitudes of the projection (associated eigenvalues) of the observations on the vectors. The vector  $c_1$  has the largest eigenvalue,  $c_2$  the second largest, etc. Therefore, the vectors encompass a decreasing amount of variability of the dataset. To limit the dimensions of the dataset on which the K-means algorithm is applied, only the  $L$  first vectors are selected.

The **K-mean** algorithm is then applied to the  $M$  observations projected on the  $L$ -dimensional space  $(c_1, \dots, c_L)$ . The number of clusters  $K$  has to be fixed. The output of the algorithm is the attribution of a cluster (between 1 and  $K$ ) to each of the  $M$  observations.

### 6.2.2 DynClust algorithm

The package "DynClust: Denoising and clustering for dynamical image sequences (2D or 3D)+T" implements the DynClust algorithm in R and is available on the Comprehensive R Archive Network (CRAN). The algorithm consists in two phases: a denoising and a clustering step. It is based on a procedure which can statistically assess the similarity of two enhancement vectors  $\mathcal{I}_x$  and  $\mathcal{I}_y$  at locations  $x$  and  $y$ . This is done by testing whether the difference vector  $\mathcal{I}_x - \mathcal{I}_y$  is significantly different from the zero vector, based on a multiple test strategy.

This multiple test strategy was originally developed for Gaussian noise [117, 118], and adapted for heterogeneous symmetric noises [119]. In the statistical framework presented above, the symmetry is granted by the fact that the tested vector is the difference between two vectors corrupted by the same noise. It requires the specification of the noise variance. It also requires a level of regularity (exponent of the Holder condition superior to 0.25) in the enhancement vectors, which is satisfied in the context of contrast imaging.

The **denoising step** consists in constructing at each spatial location  $x$ , a neighbourhood  $\mathcal{V}_x$  of locations, regrouping enhancement vectors similar to  $\mathcal{I}_x$ . The construction is done iteratively, using a growing neighbourhood, by testing the similarity of the pixels spatially close to the current neighbourhood, using the tests mentioned above. This approach is therefore local. Once the denoising step is accomplished, a neighbourhood  $\mathcal{V}_x$  is associated with each spatial location  $x$ .

In the **clustering step**, clusters are constructed iteratively from these neighbourhoods, by regrouping them based on the same statistical test as used in the denoising step. However, spatial information is not used in this case, and disjoint clusters can be merged together.

Another interesting feature of the algorithm is that it does not require specification of the number of clusters to find. One hyperparameter as must be pre-selected: the variance  $\sigma$  of the noise. In practice, this parameter defines the sensitivity of the algorithm to temporal variations: the lower it is, the more sensitive to variation the algorithm is, but the less robust it is to noise (and consequently the higher the number of clusters will be). The choice of the value for this parameter is a typical compromise between robustness and sensitivity.

This algorithm has previously been tested and validated on simulated and *in vivo* DCE-CT data. Tests demonstrated a good ability to differentiate between heterogeneously perfused areas. We propose to adapt the algorithm and test it in the context of DCE-US data.

### 6.2.3 Implementation in DCE-US

#### Statistical framework

The same statistical framework as presented in Chapter 3 is used to describe the noise. A sequence of  $N$  DCE-US frames is acquired at  $t_i$  with  $1 \leq i \leq N$ . The echo-power at  $x$  or in a region around  $x$ ,  $f_x(t_i)$ , is modelled as the multiplication of a realization of a perfusion signal  $u_x$  and a standardized noise  $v$ :

$$f_x(t_i) = f_x(t_i) = u_x(t_i)v(t_i). \quad (6.1)$$

As presented in Section 6.2.2, the DynClust algorithm, as developed for DCE-MRI and DCE-CT, assumes that the signal of interest is corrupted by an additive noise. In order to comply with this condition, the logarithm of the DCE-US signal is taken. Moreover, because the information of interest is encompassed in the temporal variations of the signal and not in its baseline, the baseline value, defined as the mean signal before the time of arrival of the contrast agent  $t_{CA}$ , is subtracted from the signal:

$$\mathcal{I}_x(t_i) = \log(f_x(t_i)) - \log(\text{mean}_{t < t_{CA}}(f_x(t))) = \log(u_x(t_i)) + \log(v(t_i)) - \log(\text{mean}_{t < t_{CA}}(u_x(t))). \quad (6.2)$$

The resulting quantity is the enhancement vector, and is used as an input for K-mean and DynClust algorithms.

#### K-mean: Algorithm parameters

The implementation for DCE-US data is straightforward: the observations are the enhancement vectors  $\mathcal{I}_x$  of the ROI. The number  $L$  of components selected by the dimension reduction phase was chosen as  $L = 3$ , because it is observed that the eigenvalues  $\lambda_i$  for  $i > 3$  are low compared to the first 3 eigenvalues. The number of cluster was chosen to be  $K = 2$  for the sensitivity/specificity analysis.

### DynClust: Algorithm parameters

In this work, the variance  $\sigma$  has been set to 125. This value has been fixed using the data acquired in the kidney, by dichotomy, as offering a compromise between an accurate differentiation of anatomic areas and a low number of clusters in the areas that are anticipated to be functionally uniform.

In order to decrease processing time, the enhancement vector was computed over small ROAs of  $3 \times 3$  pixels, from which the signal was averaged rather than for all the pixels of the original sequence.

#### 6.2.4 Data simulation and acquisition

##### Simulated data set

To assess the ability of the algorithm to detect differences in perfusion, sequences with two compartments were generated, each presenting a different set of flow parameters.

DCE-US data were simulated using the algorithm presented in [96] and Chapter 4, based on the linear system formalism presented in Chapter 2. First, a perfusion signal was generated by convolving the impulse response of a vascular network with a lognormal transit time distribution generated from Eq (5.6), with an input function  $I(t)$ , also generated from a lognormal distribution with fixed parameters.

Sequences with 100 images of  $18 \times 18$  pixels were generated to simulate two compartments (I and II), each presenting different flow characteristics. Each of the two areas comprised a region with dimensions of  $9 \times 18$  pixels. In the compartment I, the reference compartment, the flow parameters time to peak ( $TTP = \exp(m - s^2)$ ) and scaling parameter  $A$  of the tissue transit time distribution are kept fixed, with values, respectively of 20 seconds and  $1.10^{-3}$  (arbitrary units). These values were chosen as typical values encountered *in vivo*. In the compartment II, the test compartment, only one parameter was varied at a time with respect to the parameters used to model flow in compartment I. Data were simulated for TTP and  $A$  varying in 5% steps, respectively, from 0% to 60% and 0% to 100% with respect to reference values, with 5% steps. For one parameter varying the other parameter is kept at its initial values. For each set of parameter values, 100 simulations were generated, which led to a data set of 3200 simulations.

##### Data acquisition in murine kidney

Data were acquired with an Aplio 50 ultrasound imaging system and a PLT-1202-S linear probe (Toshiba Medical Systems, Toshiy, Japan), used with a transmit-frequency setting of h12.0 in Contrast Harmonic Imaging (CHI) mode. The mechanical index was fixed at a low level ( $MI = 0.1$ ) to avoid bubble destruction. The size of the pixels in the sequences was  $0.06 \times 0.06$  mm. DCE-US data were acquired in the transverse plane of the left kidney of one mouse. A total of 3 independent injections were performed through a catheter in the tail vein of a mouse using a volume and speed-controlled injection system [40], which allowed a good repeatability of the injection. Each injection consisted of  $50 \mu\text{L}$  of SonoVue<sup>®</sup> (Bracco Imaging SpA, Milan, Italy) injected at a rate of 2 mL/min.

Because these sequences were subject to a high level of motion due to breathing, they were registered before applying the DynClust algorithm, using the registration method proposed in Chapter 5.

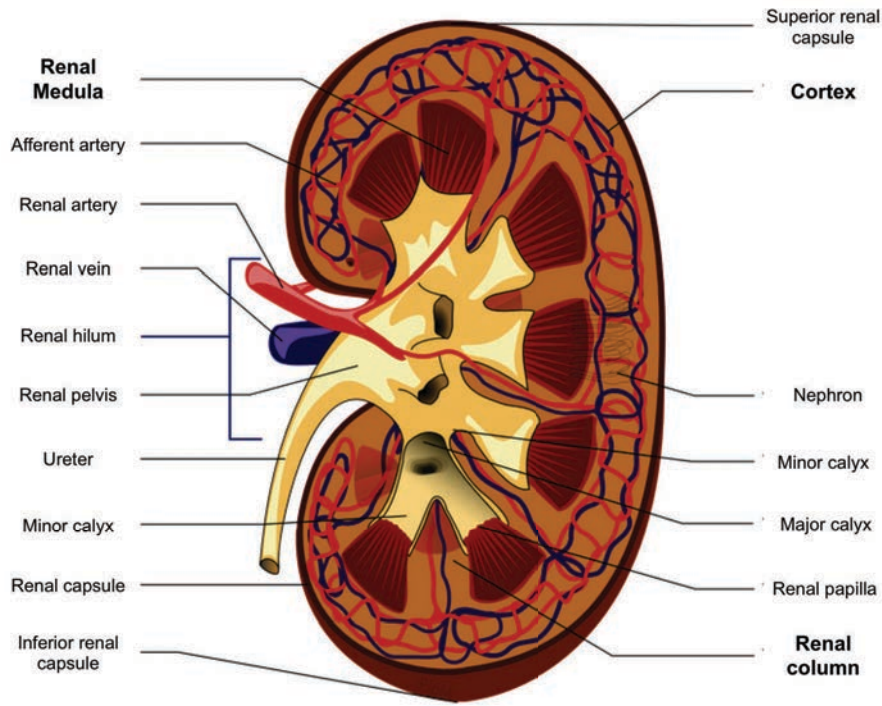


Figure 6.1: Atlas of a mammalian kidney anatomy (adapted from Piotr Michal Jaworski, CC licence)

### 6.2.5 Data comparison

#### Evaluation of sensitivity and specificity using simulated sequences

The capacity of the DynClust and K-means algorithm to correctly classify the pixels in the two compartments in two different clusters was assessed by computing the sensitivity and the specificity of the classifier, for each variation of the parameter of interest.

The sensitivity is defined as the percentage of pixels in II classified correctly:

$$\text{Sensitivity} = \frac{\text{Pixel in II classified in II}}{\text{Total number in II}}, \quad (6.3)$$

and the specificity is the number of pixels in I correctly classified:

$$\text{Specificity} = \frac{\text{Pixel in I classified in I}}{\text{Total number in I}}. \quad (6.4)$$

#### Qualitative test of clustering in normal kidney

Because kidneys anatomy is well known, it is possible to qualitatively assess anatomical relevance of the clusters obtained by the algorithm. In the data acquired in kidneys, the cluster distribution was evaluated based on discrimination of standard anatomical structures presented on Figure (6.1): the peripheral cortex of the kidney has a high vessel density with homogeneous perfusion. Vessels in the renal column carry blood from the renal artery to the cortex. The renal medula is more weakly perfused. Thus, in normal kidney, it is anticipated that three distinct flow patterns should be identified: cortex, renal columns and medula.

## 6.3 Results

### 6.3.1 Sensitivity and specificity analysis

Figure 6.2 and Figure 6.3 show the sensitivity and the specificity of the two clustering algorithms, as a function of the percent difference between parameters ( $A$  and  $TTP$ ) in compartments I and II.

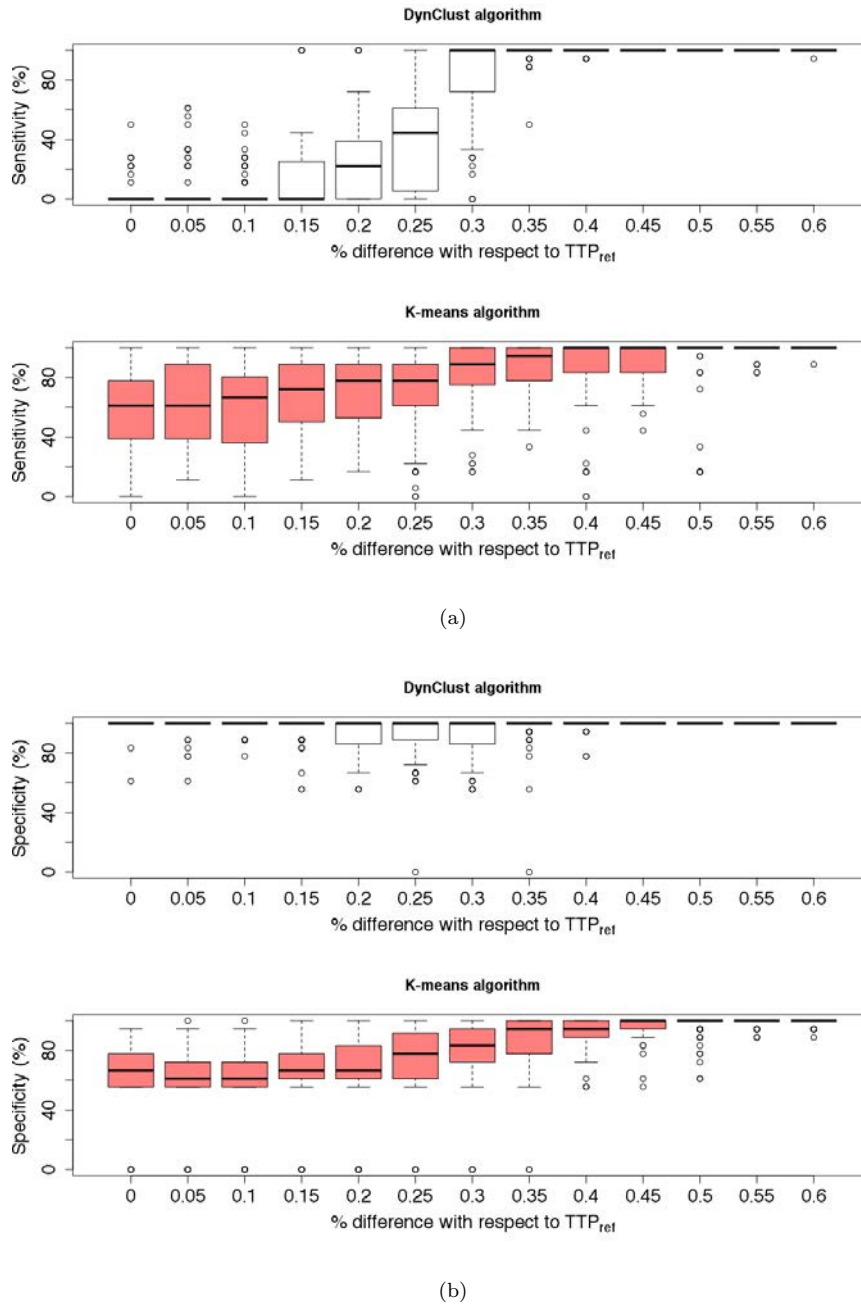
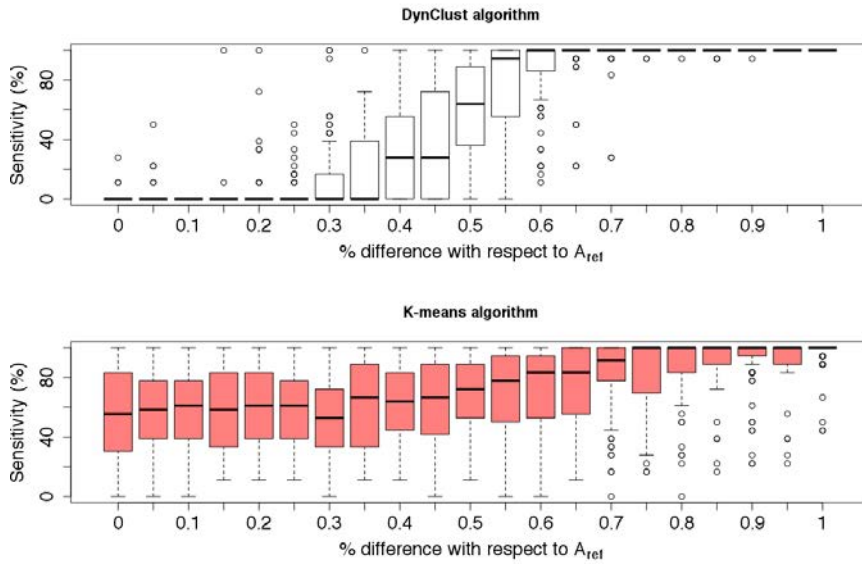
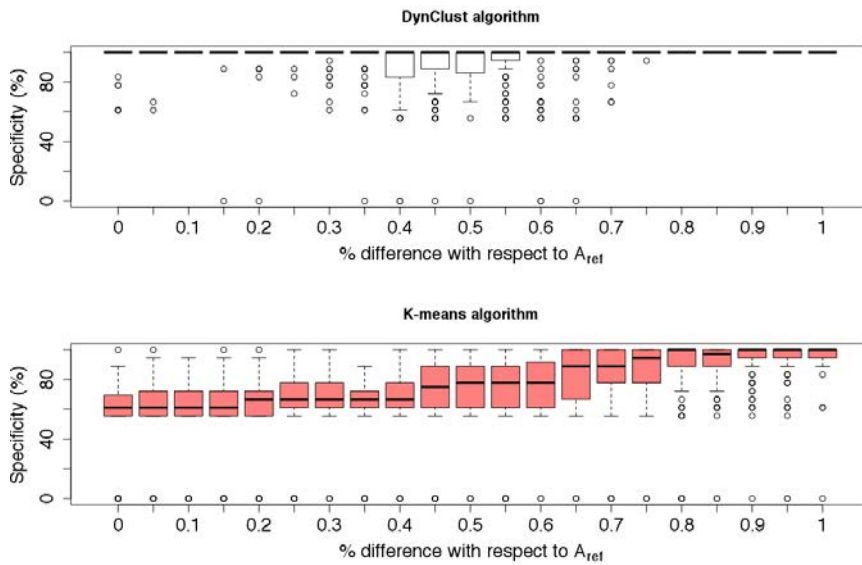


Figure 6.2: Boxplots of the specificity and the sensitivity of the method depending on the variation of  $TTP$  between the two compartments.

In the sensitivity graphs, it is visible that when the % difference between  $TTP$  or  $A$  in the two regions is below a certain level, the two regions are grouped within a single cluster. For the  $TTP$  parameter, this level is between 15 and 30% difference, while for  $A$ , it is between 30 and 50% difference. At the same time, the specificity stays high, with median values at 100% for all the % difference levels that were



(a)



(b)

Figure 6.3: Boxplots of the specificity and the sensitivity of the method depending on the variation of  $A$  between the two compartments.

tested.

For K-means, specificity and sensitivity are always non-null, even for very low % differences between parameters in the two compartments. This means that even when perfusion is approximately uniform, the algorithm tries to identify clusters. This creates a lot of false positive detections which are demonstrated by the specificity values between 70 and 80% obtained with the K-means algorithm.

### 6.3.2 Kidney qualitative evaluation

Cluster maps for the data acquired in a mouse kidney are shown in Figure 6.4 (a) (b) and (c). Only the 3 largest clusters were retained for display. In Figure 6.4 (d), representative echo-power data curves

extracted from the clusters in Figure 6.4 (b) are presented. Although the 3 acquisitions have been performed on the same kidney, the cluster maps are relatively different. However, in the 3 acquisitions, a low amplitude cluster is identified in the central zone of the kidney. This is consistent with the kidney anatomy. In the periphery, two main clusters are identified: one cluster which emits a medium signal and one cluster with higher amplitude signal. In some cases, the high-amplitude enhancement zones seem to span from the center of the kidney toward the periphery. That would be consistent with a zone corresponding to the renal columns, which bring the blood to the renal cortex.

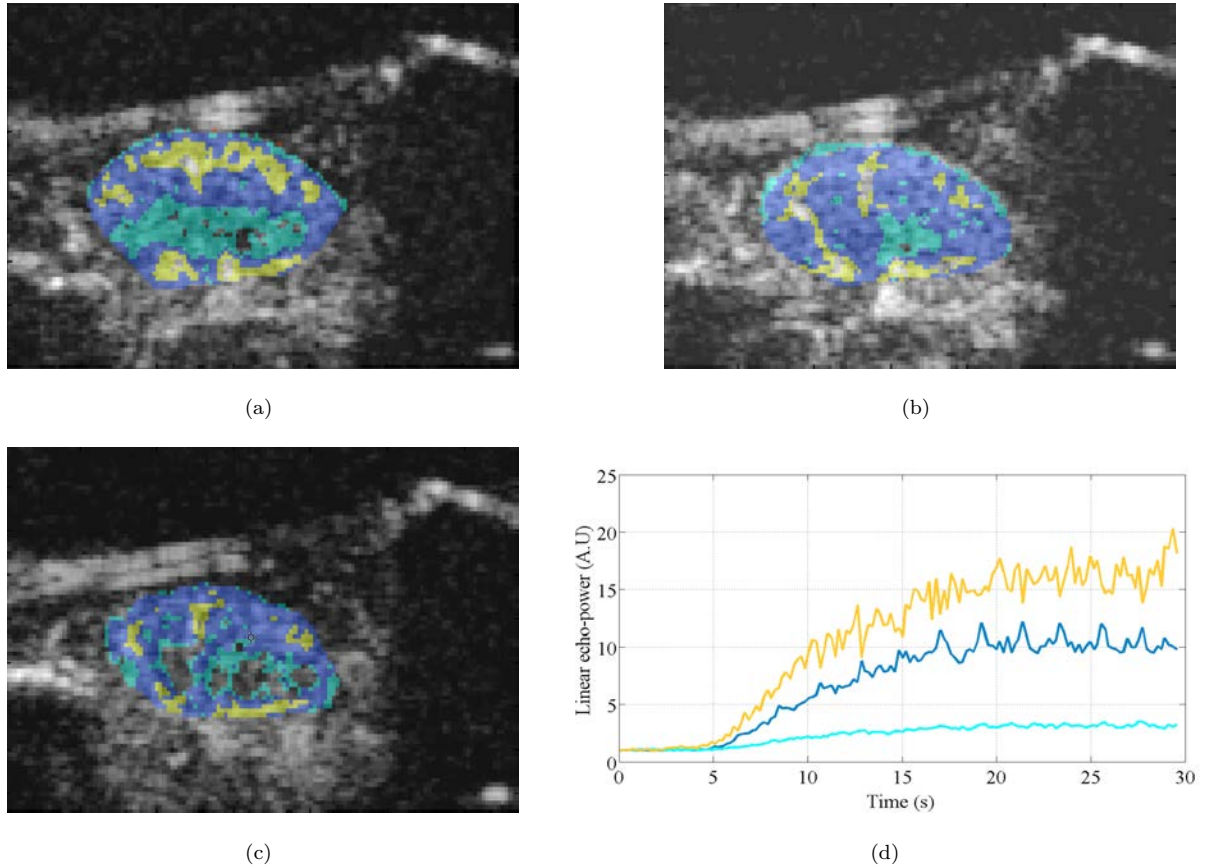


Figure 6.4: (a)-(c) B-mode images of three independent DCE-US sequences acquired *in vivo* along the transverse axis of murine kidney. The three most prevalent clusters are superimposed on the B-mode image. d) Echo-power data curves obtained from the clusters presented in Figure 6.4. The color of the curve correspond to the cluster it has been extracted from.

## 6.4 Discussion

The results obtained on the simulated data set give an idea of the order of magnitude of the variabilities of amplitude (which varies with  $A$ ) and of the kinetics (which varies with  $TTP$ ) the clustering algorithm is able to detect. This could be modified by changing the hyper-parameter of the algorithm. Nonetheless, the specificity of the algorithm is high in this configuration which prevents it from identifying insignificant heterogeneities. Moreover, the fact that the noise simulation method is non-parametric, uses experimentally acquired noise and mimics well DCE-US noise in terms of correlation and distribution according to Chapter 4 should make simulation conditions comparable to experimental conditions. Compared to

the K-means algorithm, results obtained via DynClust are more robust. Moreover, contrary to K-means algorithm, the sensitivity of DynClust is highly dependent on the % difference in the parameters between clustered zones. This is an advantage because clusters identified will maintain a characteristic level of differences in terms of temporal dynamics.

The results for the *in vivo* kidney data set, presented on Figure 6.4, look different although they are from the same individual. This could be explained by the fact that the imaging plane is not the same in each acquisitions. Moreover, the acquisitions have been performed on three different days, which could increase the variability. The results obtained on the same data set using K-means algorithm are not presented for two reasons: they are irrelevant when the number of clusters is setted to a high value (superior to 5). When the number of cluster is inferior to 5, results are comparable to those obtained with DynClust, but no quantitative comparison can be done because the ground truth is unknown. This emphasize the difficulty of using K-mean in application, such as tumour heterogeneity assessment, where the desired number of clusters is unknown. The fact that the sensitivity of DynClust to differences in temporal dynamics can be fixed via the hyperparameter  $\sigma$  is therefore a strong advantage.

In spite of the relative differences in the precise location of clusters detected on the three imaging sequences, the clusters obtained with the algorithm seems to correspond well in all cases to physiological regions of different flow. Considering that the algorithm does not use any *a priori* information about the shape of echo-power data curves, of the position or the number of clusters in the sequence, these results suggest that the algorithm has the potential to detect flow variability. This potential will be further assessed on pre-clinical data in the next chapter.

In this work, signal attenuation has not been compensated for. This could play a role because signal with a similar dynamic could be classified in different clusters, depending on how attenuated the signal is. However, this did not seem to strongly effect the results obtained in the kidney. No discernible dependence on depth was identified in the detected clusters. Attenuation is not anticipated to be very strong for the acoustic frequency (7 MHz) and imaging depths (0.1cm) considered for the acquisition of the data in the murine kidney.

The value for the hyperparameter  $\sigma$  has been selected empirically by qualitatively adjusting the parameter to enhance the detection of the different flow territories of the kidney. If the value determined this way leads to satisfactory results, it should be possible to determine in a more rigorous and satisfactory way the value of  $\sigma$ . In particular, using the simulations, it should be possible to fix the variance according the desired sensitivity.

The time necessary to run the algorithm on a sequence is approximately 3 minutes for a 128 frames sequence with  $84 \times 126$  pixels on a personal computer. This is reasonable, considering the fact than the process is completely automatic. However, the processing time can be increased when the data requires registration. Further work could consist in estimating simultaneously the cluster and the motion, in a single mathematical framework.

## 6.5 Conclusion

The applicability of a clustering algorithm to DCE-US contrast echo-power data curves, without shape and number of clusters *a priori* is evaluated, and its sensitivity and specificity are assessed on simulated, dual compartmented data. Results obtained on *in vivo* kidney data suggest that the clusters obtained are

---

physiologically relevant. By providing non-operator dependant indicators of the tumour heterogeneity, this algorithm can potentially be a promising tool to assess cancer therapy in pre-clinical or clinical studies.

# Chapter 7

## Evaluation of fitting and clustering methods on pre-clinical data

### 7.1 Introduction

In this Chapter, clustering and fitting procedure techniques presented respectively in Chapter 6 and Chapter 3 are tested on a pre-clinical dataset of murine tumours, to illustrate their interest and their potential for diagnosis and therapy following.

The dataset is constituted of three treatment groups: one group receiving an anti-angiogenic therapy acting on the vascular network, one group receiving a cytotoxic therapy stopping tumour growth but not supposed to act on vascular network structure, and a placebo group. Because the two treated groups have different therapeutic targets, they should lead to different functional modifications, in particular in terms of microvascular architecture, that DCE-US would ideally be able to capture.

In [71], an indicator evaluating the local coherence of the echo-power data curves to detect prostate cancer was proposed, demonstrating ability to accurately differentiate between cancerous and non-cancerous tissues. This indicator was based on measures of spectral coherence between the echo-power data curves extracted from one pixel and echo-power data curves from its neighbourhood. The results suggest that parameters evaluating flow coherence in tissues could be of clinical interest to follow angiogenesis. In this work, a non-parametric indicator, with a similar spirit as in [71], is proposed using the clustering algorithm results to extract information related to the dispersion of the vascular network. A measurement of the spectral coherence of the echo-power data curves extracted from the clusters with the whole tumour echo-power data curve is used.

The potential clinical interest of the clustering and the fitting method is evaluated by assessing the ability of the different indicators to differentiate between the treatment groups.

### 7.2 Material and method

#### 7.2.1 Data Acquisition

Tumours were induced by subcutaneous injection of fragment of Lewis lung (3LL) tumours cells in 61 black mice. Mice were treated from 6 days after tumour cell injection, and were allocated to three different

therapy groups: one group received 40mg/kg daily of an anti-angiogenic, one group receiving during 3 days 150mg/kg daily of a cytotoxic therapy via i.p. injections, and one group receiving a placebo.

DCE-US data were acquired from each mouse on days 1 (before therapy beginning, 6 days after cell injection.), 3, 7 and 9 days after the therapy beginning. 61 mice were included in this study: 27 controls received placebo (Placebo group), 20 mice were treated with the anti-angiogenic (Anti-ang group), and 14 with a cytotoxic treatment (Cytotoxic group).

Data were acquired with a Sequoia 512 ultrasound imaging system and 15L8w probe (Siemens) 7-14 MHz, with mechanical index fixed a low level ( $MI = 0.1$ ). The size of the pixels in the sequences is  $0.053 \times 0.053 \text{ mm}^2$ . The ultrasonic probe was placed such that the ultrasound focal zone was centred on the tumour position. Sequences were 200 frames long, with a XX Hz sampling frequency.

## 7.2.2 Processing

Before the analysis, regions of interest (ROIs) were drawn manually around the whole tumour by an expert. The size of the ROI is designated as  $|\text{ROI}|$ .

### Flow parameters extraction

The lognormal model (Eq.(5.6)) was fitted to the mean echo-power data of the whole tumour. To assess the fitting methods, parameters were extracted from the whole tumour using the least squares (LS) and the multiplicative model (MM) method (described in Chapter 3). AUC, TTP and MTT as described in Chapter 2 were estimated.

For the whole tumour analysis, the ROA is selected as equal to the whole tumour ROI. Flow parameters extracted this way are designated as  $\text{AUC}_{tot}^{\text{LS}}$  and  $\text{AUC}_{tot}^{\text{MM}}$ ,  $\text{MTT}_{tot}^{\text{LS}}$  and  $\text{MTT}_{tot}^{\text{MM}}$  and  $\text{TTP}_{tot}^{\text{LS}}$  and  $\text{TTP}_{tot}^{\text{MM}}$ .

### Clustering analysis

**Clustering results** The clustering method presented in Chapter 6 is applied to all the sequences. Parameters and implementations are identical to those of Chapter 6. The number of clusters in the ROI is  $K$ . Clusters are sorted by size, which means that cluster number 1,  $C_1$  is the largest cluster and number  $K$ ,  $C_K$ , the smallest. The size of the cluster number  $i$  is designated as  $|C_i|$ . The echo-power data curve extracted by averaging for each frame the signal coming from cluster number  $i$  is designated as  $f_i(t)$ , while the echo-power data curve extracted from the whole ROI is designated as  $f_{\text{ROI}}(t)$ .

**Coherence indicator** To assess the dispersion of flow kinetics in the whole tumour ROI, an indicators measuring the mean coherence between the echo-power data curves extracted by cluster and from the whole ROI is proposed, inspired by the coherence parameter presented in [71].

In order to have an indicator independent from the appearance time of the contrast agent in the cluster, the coherence is performed in the frequency domain: because appearance time is entirely contained in the phase of the Fourier transform, operating on the amplitude of the Fourier transform allows to overcome this issue. Because, as presented in Chapter 3, the echo-power data curves  $f_i(t)$  are considered to be a perfusion signal  $u_i$  corrupted by a multiplicative speckle noise  $v$ , the Fourier transform is performed on the logarithm of the curves. With  $F_i^{\log}(\nu)$  the Fourier transform of the logarithm of  $f_i(t)$  and the

notations of Chapter 3:

$$F_i^{\log}(\nu) = TF[\log(f_i(t))](\nu) = TF[\log(u_i(t)) + \log(v(t))](\nu) \quad (7.1)$$

$$F_i^{\log}(\nu) = TF[\log(u_i(t))](\nu) + TF[\log(v(t))](\nu) = U_i^{\log}(f) + V^{\log}(\nu) \quad (7.2)$$

According to Eq (7.1), the frequency contents of the noise  $V^{\log}(\nu)$  and of the perfusion signal  $U_i^{\log}(\nu)$  are summed and can therefore be more easily separated assuming that their bandwidths are relatively disjoint.

Once the Fourier transform has been performed, the computation of the spectral coherence coefficient can be performed on the bandwidth  $[\nu_{min}, \nu_{max}]$  of interest. The spectral coherence coefficient  $\rho$  (also used in [71]) is computed for each cluster as follow:

$$\rho(i) = \frac{\int_{\nu_{min}}^{\nu_{max}} (|F_i^{\log}(\nu)| - |\bar{F}_i^{\log}|)(|F_{ROI}^{\log}(\nu)| - |\bar{F}_{ROI}^{\log}|)d\nu}{\sqrt{\int_{\nu_{min}}^{\nu_{max}} [|F_i^{\log}(\nu)| - |\bar{F}_i^{\log}|]^2 d\nu \int_{\nu_{min}}^{\nu_{max}} [|F_{ROI}^{\log}(\nu)| - |\bar{F}_{ROI}^{\log}|]^2 d\nu}}. \quad (7.3)$$

From expression in Eq (7.3), it should be noted that the measurement is invariant by multiplication of  $f_i(t)$  by a constant: this means that this measurement is an indicator of the similarity of the shape of the temporal response of the cluster with the whole tumour response, and not of their relative amplitudes.

Finally, to obtain a unique global indicator for the whole ROI, the average spectral coherence coefficient  $\rho_{ROI}$  is computed :

$$\rho_{ROI} = 1/|ROI| \sum_i^K \rho(i)|C_i| \quad (7.4)$$

**Implementation** The minimum frequency is chosen as the first non-null frequency, such as the baseline information is suppressed:  $\nu_{min} = FR/N$  with  $FR$  the frame rate and  $N$  the number of images. The maximum frequency is chosen  $\nu_{max} = 0.5\text{Hz}$ , because it has been shown to be the limit of the frequency bandwidth for DCE-US echo-power data curves in [92].

### 7.2.3 Results comparison

To compare the different methods and parameters extracted, the evolution relative to day 1 of the different parameters are computed. For a given parameter, its evolution at day  $D$ ,  $\text{Param}^{\%}(D)$  is computed as:

$$\text{Param}^{\%}(D) = \frac{\text{Param}(D) - \text{Param}(1)}{\text{Param}(1)}. \quad (7.5)$$

To compare the efficiency of the different approaches for therapy following of the different methods and of the different parameters, their ability to reveal statistically significant differences between the different therapy group is assessed. To evaluate the significance, the non-parametric Mann-Whitney U test is used. Difference are considered significant when the p-value is lower than 0,05.

## 7.3 Results

### 7.3.1 Influence of the fitting method

The whole tumour parameter analysis led to significant differences for  $AUC_{ROI}$  parameter. The other parameters  $TTP_{ROI}$  and  $MTT_{ROI}$  did not lead to significant differences. Boxplots comparing the evolution

of  $AUC_{ROI}$  values found with MM and LS methods, at days 3, 7 and 9 are presented in Figure 7.1, with  $p$ -values displayed only when inferior to 0,05. Divergences can be observed between the two methods for the significance of the differences between the groups: at day 3 (Figure 7.1 a)), the difference between the anti-angiogenic group and the cytotoxic group is significant using MM method but is not with LS. The same is also true at day 9, and additionally a significant difference is observed between Placebo and Cytotoxic group that is not observed with MM.

### 7.3.2 Comparison clustering and whole tumour

As stated in the previous section, the whole tumour parameters  $TTP_{ROI}$  and  $MTT_{ROI}$  does not permit to differentiate between the different groups (with both fitting methods). Boxplots representing the distribution of the evolution of the number of cluster  $K$  at days 3, 7 and 9 are presented on Figure 7.2. Similarly, boxplots representing the distribution of the evolution of  $\rho_{ROI}$  at days 3, 7 and 9 are presented on Figure 7.3. No significant differences are observed at day 3. At day 7,  $K$  has increased significantly more in the Anti-angiogenic group than in the Placebo group, and decreased significantly more in the Cytotoxic group than in the Placebo group. The coherence parameter  $\rho_{ROI}$  has also decreased significantly more in the Anti-angiogenic group than in the two others. At day 9, the difference between Anti-angiogenic group and placebo group has been lost, but all the other differences are maintained.

## 7.4 Discussion

### 7.4.1 Influence of the method of fitting

The results presented in section 7.3.1 show that the use of the MM leads to significant differences between groups for the parameter  $AUC_{ROI}^{MM}$  that are not completely similar with those obtained using LS fitting  $AUC_{ROI}^{LS}$ . In particular, an early difference is observed at day 3 between the Anti-angiogenic and the Cytotoxic groups.

It is not possible to assert without doubt that these differences are real functional differences and are not artefacts of the fitting method. However, several elements can be noticed: first, the differences observed are coherent with the respective expected effects of the anti-angiogenic and the cytotoxic therapy. Indeed, the Cytotoxic, is not supposed to act on the organization of the vascular network, while the Anti-angiogenic is. It seems therefore consistent to observe no difference between Placebo group and Cytotoxic group for an indicator related to the density of the network such as  $AUC_{ROI}$ , but significant differences between those two groups and the Anti-angiogenic group. Moreover, contrary to the results obtained using the LS method, the significance of the differences observed with the MM method are the same at days 3, 7 and 9. This is an argument that plays in favour of the MM method. For the other parameters ( $TTP_{ROI}$  and  $MTT_{ROI}$ ), the absence of significant difference using both method suggests that those parameters are not adapted to describe the differences between the groups in this particular study, and a fortiori to differentiate the two fitting methods.

The results above and the better theoretical basis of the MM method presented in Chapter 3 altogether suggest that the MM method of fitting could be adopted without risk of creating misleading results, and could potentially lead to changes in the functional differences observed with again potentially better characterisation of the effects of different therapies.

## 7.4.2 Interest of the clustering algorithm

The results observed with the evolution of the number of cluster obtained via the clustering algorithm show significant differences at day 7 between all the groups. This is the only parameter allowing to differentiate independently the three treatment groups. The explanation could be as follow: the number of cluster is correlated with the dispersion of the temporal profile but also with the size of the region of interest ( $R = 0.56$ ,  $p < 0.05$ ), as it can be seen on Figure 7.4, where the number of cluster is plotted against the size of the ROI for all the tumours before therapy beginning. Therefore, because the cytotoxic therapy limits the growth of the size of the tumour and the anti-angiogenic acts on its vascular structure, the difference observed may be the conjugate result of those two different causes.

In this sense, results observed with the spectral coherence parameter  $\rho_{ROI}$  are interesting, because this parameter is not significantly correlated with the size of the tumour. The differences observed are consistent with the expected effects of the therapy: the heterogeneity of the vascular network decreases in the anti-angiogenic group, compared to the two other groups. Moreover, this differences are maintained at day 9. As stated earlier, this parameter is not related to the amplitude of the flow that goes through the tumour (as AUC is) but only to the temporal profile of the echo-power data curves: for tumours taken before therapy beginning, correlation between AUC and  $\rho_{ROI}$  is non-significant. The information that it brings about the tumour is therefore different from the information captured by AUC.

One limit of this work is that the  $\rho_{ROI}$  parameter has not been validated using a ground truth method such as histology or another imaging modality. The assumption that its variations are related to the variations of organisation of the vascular network is therefore theoretical. However, the clustering technique it is based on has been validated in Chapter 6, and the spectral coherence is a well known quantity that has been extensively used in various domains, and that has been shown to be of interest in the context of DCE-US [71]. Associated with the fact that the results obtained are consistent with the clinical context, that the theoretical basis of the methods are solid, and that the conventional kinetic indicators TTP and MTT does not identify differences between the groups, the results obtained are encouraging.

For the computation of  $\rho_{ROI}$ , the bandwidth has been selected based on the literature. Further work could consist in investigating deeper what is precisely the frequency content of echo-power data curves  $f(t)$  and their logarithm, to have a finely tuned bandwidth that filter enough noise without leading to a loss of information.

## 7.5 Conclusion

In this study, the interest of the MM fitting algorithm presented in Chapter 3 and of the clustering technique presented in Chapter 6 are evaluated on a large pre-clinical data set. The MM fitting algorithm allows to obtain results that seems slightly more consistent than the LS algorithm, without additional cost. The clustering algorithm conjugated with a new proposed parameter evaluating the dispersion of the flow kinetics in the tumour allows to identify differences that does not appear with the parameters extracted via traditional parametric model fitting.

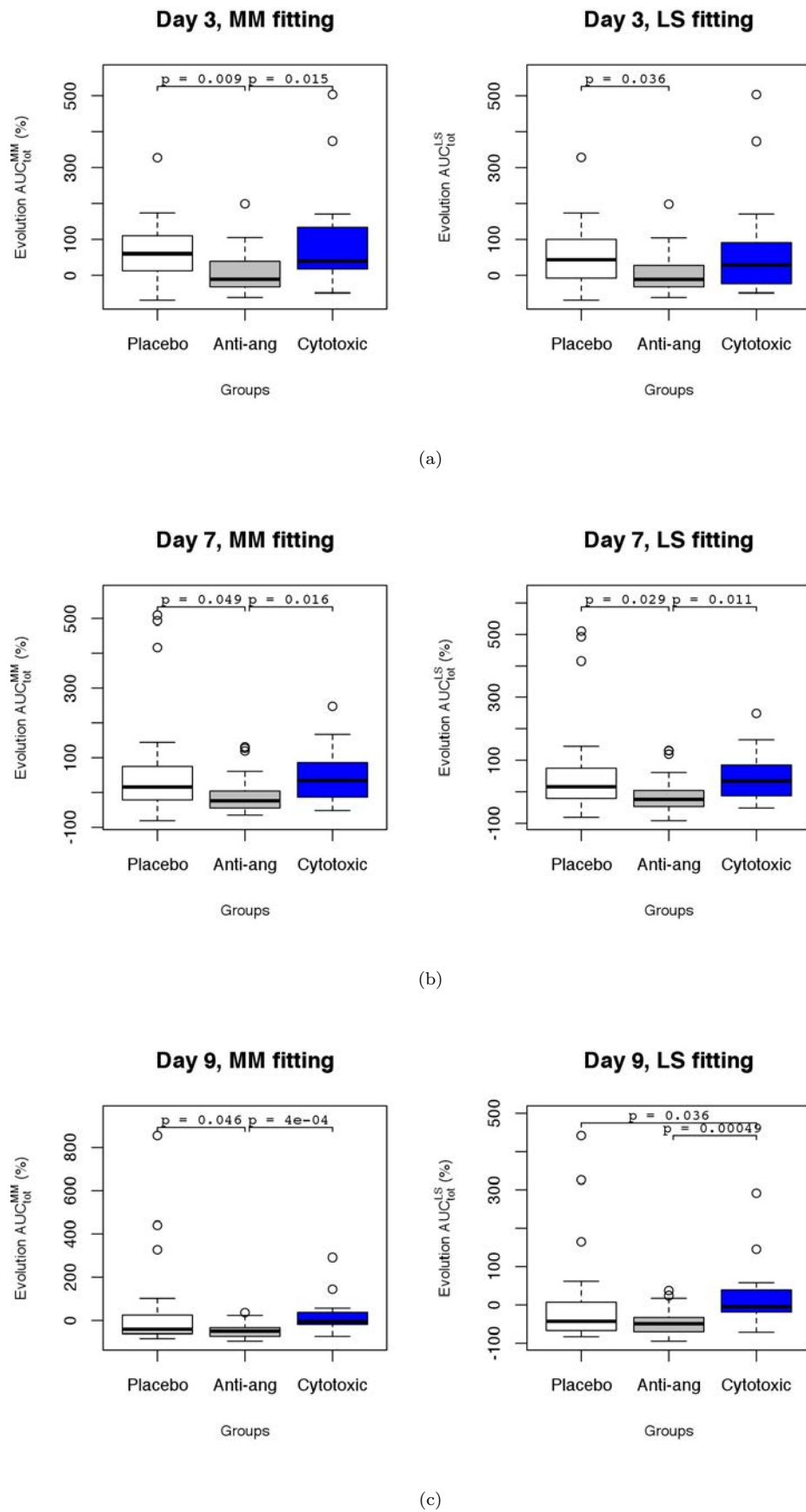


Figure 7.1: Boxplots of the evolution of the AUC parameter, estimated from curve fit performed with the MM fitting method and the LS fitting method, at Days 3 (a), 7 (b) and 9 (c) after therapy. The level of significance for discrimination of the anti-angiogenic group as compared to the placebo and cytotoxic treatment groups was strengthened when MM fitting was used.

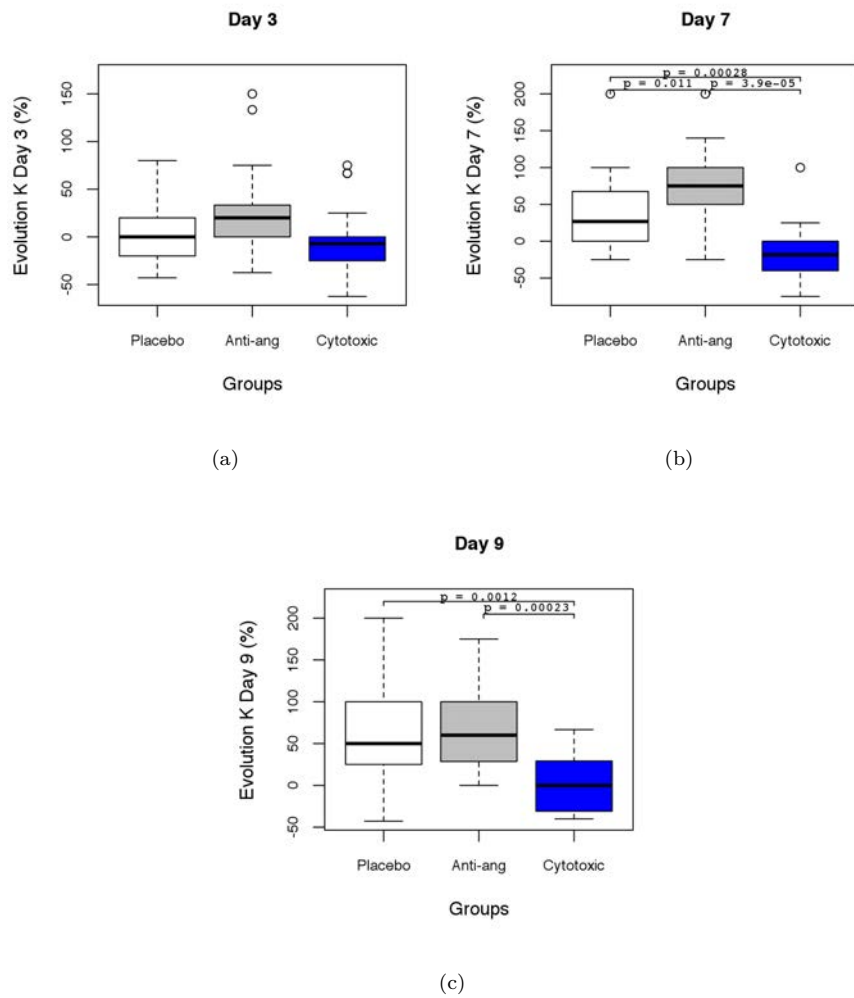


Figure 7.2: Boxplots of the evolution of the number of clusters by group, for days 3, 7 and 9 after therapy

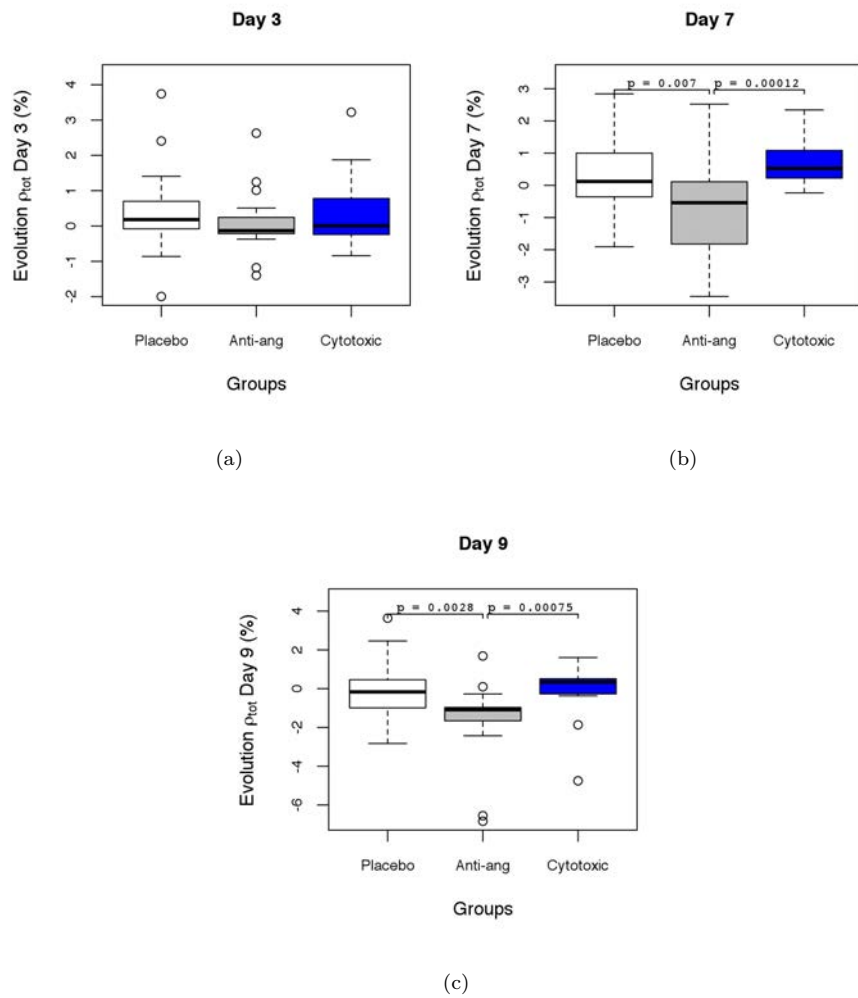


Figure 7.3: Boxplots of the evolution of  $\rho_{ROI}$ , for days 3, 7 and 9 after therapy

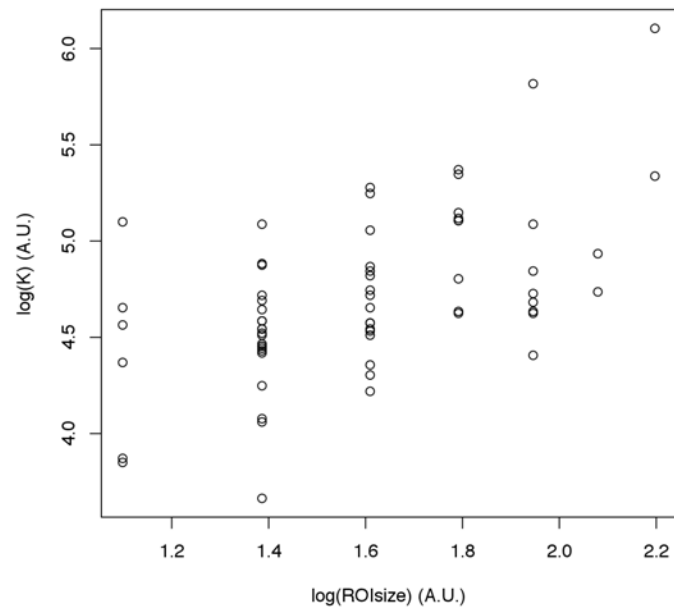


Figure 7.4: Logarithm of the number of label  $K$  as a function of the logarithm of  $|ROI|$ . From this graph, the correlation between these two parameters appears clearly.

# Chapter 8

## Discussion and perspectives

The goal of this thesis was to develop methods to decrease the variability and improve the robustness of post-acquisition processing of DCE-US imaging. These advances are necessary so that DCE-US can meet its full potential for the monitoring of anti-angiogenic therapies. The underlying approach of this work was that improving the characterization of DCE-US signal can significantly improve post-acquisition analysis by enabling the development of better adapted and more specific methods.

### 8.1 Summary and discussion

Several aspects of the quantification process in DCE-US have been addressed, and new methods have been proposed and validated to improve the quantification. The development of these methods has been shown to provide better and more robust quantification of the microvascular network. We have shown that the estimated parameters are relevant for monitoring anti-angiogenic treatment effects on tumor microvascular network.

The regression method proposed in Chapter 3 leads to modifications in the values of estimated flow parameters that may not seem very spectacular, in particular when considering whole tumour ROAs. However, the results presented in Chapter 7 demonstrate that the changes induced by the regression method have consequences on the significance of the differences between the groups. Moreover, when the method is used to fit models to data from small ROAs, estimated flow parameters are significantly ( $p < 0.05$ ) more robust, as presented in Chapter 3. The regression algorithm is easy to implement, it can be used immediately in pre-clinical studies and be transferred rapidly to the clinical setting. Software that is currently used in clinical or pre-clinical studies, such as VueBox<sup>TM</sup> (Bracco Suisse SA, Geneva, Switzerland), or QLAB<sup>TM</sup> (Philips) currently rely on least squares based methods to fit parametric models to the echo-power data [120, 121]. Integration within such software of the regression method presented in Chapter 3 would be relatively straight forward and could have impact on the sensitivity of the DCE-US analysis to angiogenic modifications.

One of the main problems encountered in the validation of processing algorithms, in particular in DCE-US, is the lack of realistic data where ground truth is accessible. The sequence simulation technique presented in Chapter 4 provides a helpful alternative when large, calibrated data sets are not available. Because the simulation of the noise is non-parametric and based on experimental data, it can be considered as an objective dataset. This should be an advantage as compared with sequence simulations made using

parametric methods which require subjective choices for the noise distribution. The main limitation of the technique proposed in Chapter 4 is that to simulate the sequences, the method requires the acquisition of a dose ranging dataset for each ultrasound imaging system, contrast agent and set of imaging-system settings. Moreover, as the simulation is based on a simplified model for the signals, it cannot take into account physical effects such as saturation or attenuation.

Follow-up studies in the pre-clinical or clinical settings can include a large number of DCE-US sequences acquired at different points in time with varied imaging planes. Sequence analysis can be disturbed by physiological motion artefacts. In this context, the possibility to use an automatic algorithm for sequence registration as proposed in Chapter 5 is desirable. One limit of the method is that it does not account for out-of-plane images: it therefore must be used in conjunction with an out-of-plane image-detecting algorithm. Further work could consist in investigating whether out-of-plane images cause variations in the registration metric that can be detected so that these images could potentially be automatically discarded.

Finally, the clustering algorithm proposed in Chapter 6 also has the advantage to be completely automatic. This technique has great potential as shown in Chapter 7 because it is able to capture differences that do not appear with more traditional flow parameters. Moreover, it is a non parametric method that could even be applied to other contrast uptake kinetics such as those exhibited by targeted contrast agent, to differentiate between areas with attached and non-attached microbubbles. In spite of the significant promise shown by the clustering algorithm, it needs to be validated using other modalities such as confocal microscopy capable of precisely assessing the spatial and flow distribution of the microvascular network. Moreover, because the method is strongly effected by motion and in particular by out-of-plane images, its transfer to clinical datasets should be accompanied by the use of efficient motion-compensation algorithms.

## 8.2 Key remaining questions

### 8.2.1 Better characterization of the input function

The work presented in this thesis has focused on reduction of variability in post-acquisition processing. However, as stated in Chapter 2, the variability in DCE-US can also come from factors inherent to the acquisition itself. One major identified cause of variability is the lack of repeatability of the input function  $I(t)$ . This lack of repeatability has two main causes. First the injection cannot be perfectly repeatable, even using an automatically controlled injection system. Second, physiological variations (in terms of temperature, anaesthesia, blood pressure or cardiac frequency) lead to differences in the pathway that the injected contrast agent microbubbles must traverse before reaching the ROA. Therefore, even for successive injections within the same individual, the repeatability of the input function cannot be guaranteed.

Several solutions can be proposed to deal with variability of the input function. One approach is to use non-parametric techniques that do not assume specific behaviour of the echo-power data curves, but rather measure the spatial distribution of echo-power data curves. This is for instance what is proposed in [71] or with the clustering technique presented in Chapters 6 and 7. However, this approach can only provide information about the heterogeneity of the vascular network.

Another approach is to use deconvolution techniques, such as the ones proposed in [122] and [35]. However, these techniques are difficult to use *in vivo* because they require direct evaluation of the input function, for instance, in an afferent artery. Jirik et al. [36] have proposed a variation of this technique that does not require an external measurement of the input function.

In theory, the best possible input function would be a Dirac of contrast agent: in the framework of the linear formalism in Chapter 2, it would lead to a signal linearly related to  $h(t)$ , i.e. of the Transit time cumulative density function. Some preliminary works have been done to assess the feasibility of this approach, using microbubbles destruction to modulate the input function as a Dirac.

### 8.2.2 Acquisition of information from the full tumor volume

All the work performed during this thesis was made using 2D+time sequences. This necessarily implies a certain number of hypotheses and approximations. First, the imaging plane is considered representative of the whole tumour. This hypothesis is not well upheld for heterogeneous tumours. Moreover, the selection of the imaging plane is highly operator-dependant. This also diminishes the technique's reproducibility because it is very difficult to position the probe at exactly the same location for measurements repeated at intervals during therapeutic follow-up in longitudinal studies. Finally, as mentioned in Chapter 2, the mathematical formalism used in DCE-US implies that the ROAs considered are all independent from each other and perfused via a single input and a single output. This hypothesis is necessary because 2D data acquisition does not provide data of the full, volumetric neighbourhood. Three-dimensional data can overcome these limitations. The full tumor volume can be scanned more reproducibly. The imaging plane issue becomes almost irrelevant. Moreover, models taking into account the input/output relationships between adjacent voxels can be developed. Such volumetric approaches would lead to more accurate, non-parametric mapping of a tumour's vascular network.

All the methods we have developed in this thesis can be transferred toward the analysis of volumetric data sets. Because the image formation principle remains similar, the multiplicative model for the noise applies equally well to 3D data and the fitting method developed in Chapter 3 could be directly transferred. The registration method developed in Chapter 5 is even more relevant because 3D data sets supply the information necessary to deal with out-of-plane motion. Gating techniques become irrelevant while efficient registration becomes indispensable. Moreover, 3D acquisitions should allow the use of a non-rigid motion framework for registration, which could strongly improve the quantification. Clustering and simulation methods are also based on algorithms that can be easily implemented in 3D. Cluster identification, in particular, is of critical interest for three-dimensional data sets because manual segmentation is more complex.

The transfer to 3D is, however, costly in terms of data processing. For instance, the number of degrees of freedom is multiplied by two for registration (more if a non-rigid motion framework is used). The clustering method performs computation over neighbourhoods of pixels. The number of pixels in the neighborhood is squared for volumetric data as compared to 2D data. Finally, modelling and solving at the voxel level for parameters describing the flow of microbubbles is a very difficult inverse problem. Transferring techniques toward the analysis of 3D data sets will, therefore, require considerable effort to make algorithms more efficient and/or to parallelize computations.

### 8.2.3 Toward a better modelling of tissues: biophysical models and multi-modality

The regression, simulation, registration and clustering methods proposed in this thesis are based on the model presented and validated in Chapter 3, that accounts for the multiplicative nature of the noise corrupting DCE-US sequences. As mentioned in Chapter 2 in Section 2.6, other physical phenomena affecting microbubble behaviour could also be taken into account. The next step toward a more accurate modelling of DCE-US signal could include development of a biophysical model able to integrate attenuation, microbubble behaviour and tissues properties within a single estimation framework. This would require precise calibration using phantoms and histological reference data to be able to relate measured signal with the nature of tumor tissues. It could also be interesting to consider information from other ultrasonic imaging modes such as B-mode imaging, quantitative ultrasound (QUS) or elastography to obtain complementary information about the tumor.

More generally, a promising approach in medical imaging and, in particular in cancer imaging, has begun to emerge that uses image-based data jointly with biophysical tumour models [123]. Within the last few years, mathematical models of tumour evolution have been developed and validated that model growth of different types of biological territories within the tumor [124]. These models necessitate data concerning the tumor composition for their initialization and calibration. Information about the compartments (e.g. perfused, hypoxic and necrotic) of a tumor assessed with functional medical imaging could be a valuable source of information for such models. In principle, once models have been calibrated and validated, they could provide information about the potential evolution of a tumour and orient therapeutic decisions.

## 8.3 Conclusion

Dynamic contrast enhanced ultrasound is a promising imaging modality for cancer and therapy monitoring. In this work, methods have been developed to improve the robustness of the quantification, by improving post-processing steps of the quantification and modelling more accurately DCE-US noise. By doing so, more accurate and informative indicators are obtained to follow the modifications of microvascular flow. A method to simulate realistic DCE-US sequences has also been developed. Such simulations can be used to test new algorithms on data corrupted with realistic noise. The introduction of 3D acquisitions and the development of tumour growth models offer promising perspectives which could lead to further improvements in the interpretation of ultrasonic data from tumors and, ultimately, a better understanding of tumor development.

# Appendix A

## K-coherence algorithm

### A.1 Detailed description of the $K$ -coherence algorithm

The aim of the analysis phase is to compute, for each pixel of the sample, a set of the  $k$ -most similar pixels in the sample. The analysis can be described in pseudo-code as follow:

```
1 Input:
2  $k$ , the coherence number,
3  $G = \{(x_1, x_2), x_1 \in [1 : N_{sample}], x_2 \in [1 : M_{sample}]\}$  sample grid,
4  $I_{sample} : G \rightarrow \mathbb{R}$  sample image
5 Output:
6  $S : G \rightarrow \underbrace{\{G, \dots, G\}}_k$  similarity set
7 Algorithm:
8  $S$  initialized at undefined at all values of  $G$ . for all  $x \in G$  do
9   for all  $x' \in G, x' \neq x$  do
10    if  $undefined \in S(x)$  then
11      add  $x'$  in  $S(x)$  in place of the first undefined element;
12    else
13      if  $\exists x'' \in S(x), d(I_{sample}(neighborhood(x)), I_{sample}(neighborhood(x''))) <$ 
14         $d(I_{sample}(neighborhood(x)), I_{sample}(neighborhood(x'')))$  then
15        replace  $x''$  by  $x'$  in  $S(x)$ ;
16      end
17    end
18 end
```

**Algorithm 2:** Analysis phase of the  $K$ -coherence algorithm

The analysis phase has two user-selected parameters, the coherence number  $k$  and the sample image. During the analysis phase, for each input pixel of the sample, a similarity set of the  $k$  most similar pixels in the sample is constructed. The squared difference between linear power of the filled neighborhoods of the considered pixels is the distance. After the analysis phase, the synthesis phase, resulting in the

complete construction of the simulated image, can begin:

```

1 Input:
2  $S : G \rightarrow G^k$  similarity set constructed in the analysis phase,
3  $I_{sample} : G \rightarrow \mathbb{R}$  sample image,
4 Output:
5  $G_{simulated} = \{(x_1, x_2), x_1 \in [1 : N_{simulated}], x_2 \in [1 : M_{simulated}]\}$ , simulated image grid,
6  $I_{simulated} : G_{simulated} \rightarrow \mathbb{R}$  simulated image,
7  $P_{simulated} : G_{simulated} \rightarrow G_{sample}$  position in the sample of the selected pixel selected to fill
    $I_{simulated}$ 
8 Algorithm:
9 Selection of an  $m \times m$  seed in the sample;
10 Initialization of the center of  $I_{simulated}$  with the seed and the other points with undefined;
11 Initialization of the center of  $P_{simulated}$  with the positions of the seed pixels in the sample and the
   other points with undefined;
12  $Curr =$  Coordinates of a pixel adjacent to the seed;
13 while there are undefined pixels in  $I_{simulated}$  do
14    $AlreadyFillNeigh = P_{simulated}(x \in neighborhood(Curr) \ \& \ x \ defined)$ ;
15    $Candidates = SelectCandidates(AlreadyFillNeigh, S)$ ;
   // The SelectCandidates() function is illustrated in Figure A.1
16    $Threshold = SetThresh(Candidates)$ ;
17   for  $x \in Candidates$  do
18     if  $d(I_{simulated}(AlreadyFillNeigh), I_{sample}(neighbors(x))) < Threshold$  then
19        $\quad$  add  $x$  to  $ValidCandidates$ ;
20     end
21   end
22    $P_{simulated}(Curr) = randomChoice(ValidCandidates)$  ;
23    $I_{simulated}(Curr) = I_{sample}(P_{simulated}(Curr))$ ;
24    $Curr = NextPixel(Curr)$ ;
25 end

```

**Algorithm 3:** Synthesis phase of the  $K$ -coherence algorithm

In the synthesis phase, the size of the simulated image and of the initial seed are chosen by the user. The initial seed can be selected deterministically or randomly. The construction of the candidate set function is diagramed in Figure A.1 using an example. Several strategies can be employed for the definition of the threshold value: its value is defined as 130% of the minimum distance among the candidate set, which adds randomness in the construction. It would also be possible to have a fixed value, or to set it as 100% of the minimum distance among the candidate set (in this case it is desirable to have a deterministic algorithm). Finally, different strategies can be employed for the selection of the next pixel. Pixels were selected and filled using a helical progression. A random selection of the next pixels in the neighborhood of the filled zone could also be imagined, to introduce another source of randomness.

The similarity measurement used in the analysis and synthesis phases is the sum of squares of the differences of neighborhood contrast echo-powers. The best distribution and correlation results were

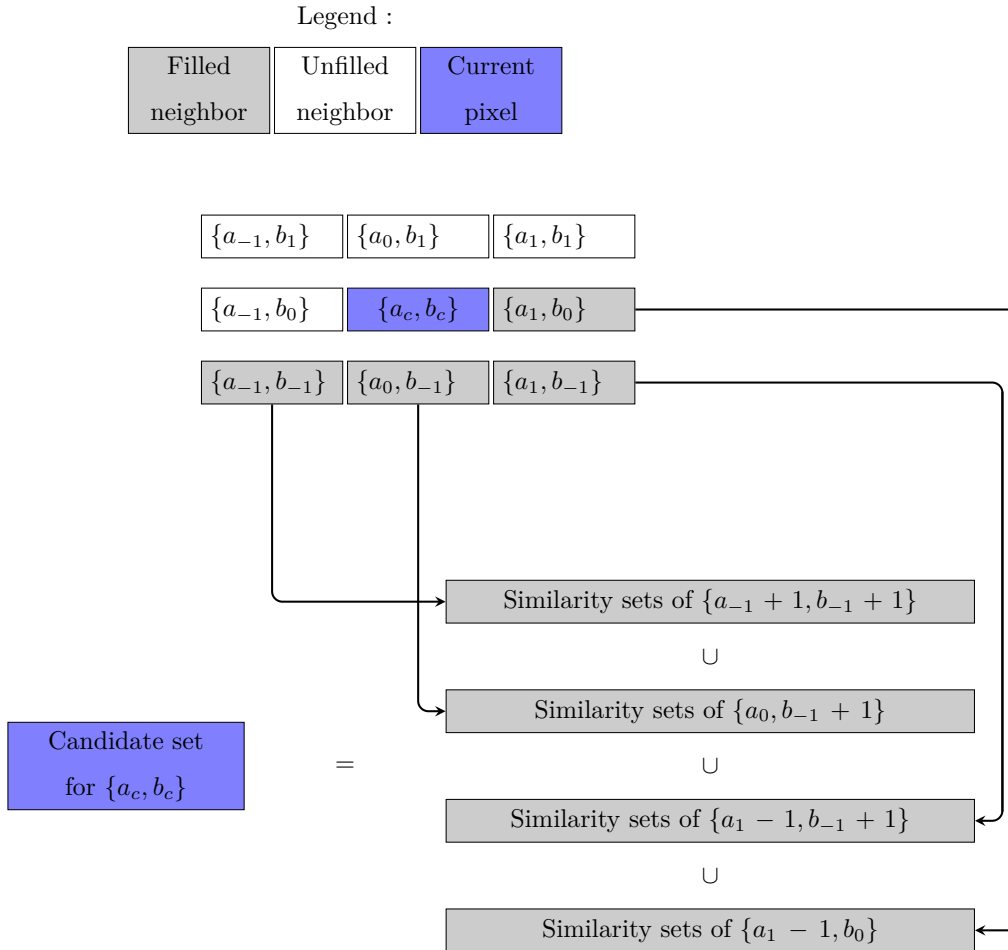


Figure A.1: Schematic diagram of an example of the synthesis phase. For each pixel, the original coordinates of the pixel in the sample are shown in brackets.  $\{a_c, b_c\}$  is unknown and needs to be determined. The candidate set is constituted according to the position of the neighbors in the original sample image. After the end of the synthesis phase for this pixel, the algorithm will go to the next unfilled pixel which, in this case, will be pixel  $\{a_{-1}, b_0\}$ .

obtained for  $k = 3$  and a  $3 \times 3$  neighborhood.

Because the values in the simulated image are only those present in the sample, the choice of the sample image is critical: it needs to be representative of the statistical distribution to be mimicked. The integration of the dose-ranging image in the  $K$ -coherence algorithm is summarized in Figure 4.1.

To generate the baseline noise  $\epsilon$ , the sample is taken from an image acquired under the same conditions as dose-ranging data but without contrast agent. To generate the contrast speckle  $v$  the sample was chosen in an image of the dose-ranging acquisition with an appropriate concentration.

# Bibliography

- [1] Institut national du cancer. La situation du cancer en France en 2012. Technical report, 2012.
- [2] F Binder-Foucard, Aurélien Belot, and Patricia Delafosse. Estimation nationale de l'incidence et de la mortalité par cancer en France entre 1980 et 2012. *Registres des cancers*, 2013.
- [3] Ralph Weissleder. Molecular imaging in cancer. *Science*, 312(5777):1165–8, May 2006.
- [4] Gabriele Bergers and Laura E Benjamin. Tumorigenesis and the angiogenic switch. *Nature reviews. Cancer*, 3(6):401–10, June 2003.
- [5] Benjamin J Vakoc, Ryan M Lanning, James a Tyrrell, Timothy P Padera, Lisa a Bartlett, Triantafyllos Stylianopoulos, Lance L Munn, Guillermo J Tearney, Dai Fukumura, Rakesh K Jain, and Brett E Bouma. Three-dimensional microscopy of the tumor microenvironment in vivo using optical frequency domain imaging. *Nature medicine*, 15(10):1219–23, October 2009.
- [6] IC Davidson, C Sanger, and RH Thomlinson. High-pressure oxygen and radiotherapy. *The Lancet*, pages 1091–1095, 1955.
- [7] J Folkman, K Watson, D Ingber, and D Hanahan. Induction of angiogenesis during the transition from hyperplasia to neoplasia. *Nature*, 1989.
- [8] J Drevs and V Schneider. The use of vascular biomarkers and imaging studies in the early clinical development of anti-tumour agents targeting angiogenesis. *Journal of internal medicine*, 260(6):517–29, December 2006.
- [9] Aymeric Guibal, Laurent Taillade, Sebastien Mulé, and Eva Comperat. Noninvasive Contrast-enhanced US Quantitative Assessment of Tumor Microcirculation in a Murine Model: Effect of Discontinuing Anti-VEGF Therapy<sup>1</sup>. *Radiology*, 254(2), 2010.
- [10] Maria Assunta Zocco, Matteo Garcovich, Andrea Lupascu, Enrico Di Stasio, Davide Roccarina, Brigida Elenora Annicchiarico, Laura Riccardi, Maria Elena Ainora, Francesca Ponziani, Gianluigi Caracciolo, Gian Lodovico Rapaccini, Raffaele Landolfi, Massimo Siciliano, Maurizio Pompili, and Antonio Gasbarrini. Early prediction of response to sorafenib in patients with advanced hepatocellular carcinoma: The role of dynamic contrast enhanced ultrasound. *Journal of hepatology*, 59(5):1014–21, November 2013.
- [11] RK Jain. Understanding Barriers to Drug Delivery : High Resolution in Vivo Imaging Is Key. *Clinical Cancer Research*, pages 1605–1606, 1999.

- [12] RK Jain. Normalization of tumor vasculature: an emerging concept in antiangiogenic therapy. *Science*, 307(5706):58–62, 2005.
- [13] Hans Petter Eikesdal and Raghu Kalluri. Drug resistance associated with antiangiogenesis therapy. *Seminars in cancer biology*, 19(5):310–7, October 2009.
- [14] JA Stanley, WU Shipley, and GG Steel. INFLUENCE OF TUMOUR SIZE ON HYPOXIC FRACTION AND THERAPEUTIC SENSITIVITY OF LEWIS LUNG TUMOUR. *British journal of cancer*, 1951, 1977.
- [15] S Koscielny, M Tubiana, M G Lê, a J Valleron, H Mouriessse, G Contesso, and D Sarrazin. Breast cancer: relationship between the size of the primary tumour and the probability of metastatic dissemination. *British journal of cancer*, 49(6):709–15, June 1984.
- [16] E a Eisenhauer, P Therasse, J Bogaerts, L H Schwartz, D Sargent, R Ford, J Dancey, S Arbuck, S Gwyther, M Mooney, L Rubinstein, L Shankar, L Dodd, R Kaplan, D Lacombe, and J Verweij. New response evaluation criteria in solid tumours: revised RECIST guideline (version 1.1). *European journal of cancer (Oxford, England : 1990)*, 45(2):228–47, January 2009.
- [17] Joseph a Ludwig and John N Weinstein. Biomarkers in cancer staging, prognosis and treatment selection. *Nature reviews. Cancer*, 5(11):845–56, November 2005.
- [18] Vathany Kulasingam and Eleftherios P Diamandis. Strategies for discovering novel cancer biomarkers through utilization of emerging technologies. *Nature clinical practice. Oncology*, 5(10):588–99, October 2008.
- [19] Kim Barrett, Edwin Brooks, Scott Boitano, and Susan Barman. *Ganong's review of medical physiology*. 23rd editi edition, 2010.
- [20] P T Wells, M Halliwell, R Skidmore, a J Webb, and J P Woodcock. Tumour detection by ultrasonic Doppler blood-flow signals. *Ultrasonics*, 15(5):231–2, September 1977.
- [21] J Bercoff and G Montaldo. Ultrafast compound doppler imaging: providing full blood flow characterization. *IEEE Transactions on Ultrasonics, Ferroelectrics and Frequency Control*, 58(1):134–146, 2011.
- [22] Nathalie Lassau, Serge Koscielny, Linda Chami, Mohamed Chebil, Baya Benatsou, Alain Roche, Michel Ducreux, David Malka, and Valerie Boige. Advanced Hepatocellular Carcinoma: Early Evaluation of Response to Bevacizumab Therapy at Dynamic Contrast-enhanced US with Quantification-Preliminary Results. *Radiology*, 258(1):291–300, 2011.
- [23] K a Miles, C Charnsangavej, F T Lee, E K Fishman, K Horton, and T Y Lee. Application of CT in the investigation of angiogenesis in oncology. *Academic radiology*, 7(10):840–50, October 2000.
- [24] M Rijpkema, J H Kaanders, F B Joosten, a J van der Kogel, and a Heerschap. Method for quantitative mapping of dynamic MRI contrast agent uptake in human tumors. *Journal of magnetic resonance imaging : JMRI*, 14(4):457–63, October 2001.

- [25] Telli Faez, Marcia Emmer, Klazina Kooiman, Michel Versluis, Antonius van der Steen, and Nico de Jong. 20 Years of Ultrasound Contrast Agent Modeling. *IEEE transactions on ultrasonics, ferroelectrics, and frequency control*, 60(1):7–20, January 2013.
- [26] a L Klibanov, M S Hughes, F S Villanueva, R J Jankowski, W R Wagner, J K Wojdyla, J H Wible, and G H Brandenburger. Targeting and ultrasound imaging of microbubble-based contrast agents. *Magma (New York, N.Y.)*, 8(3):177–84, August 1999.
- [27] Michael a Ainslie and Timothy G Leighton. Review of scattering and extinction cross-sections, damping factors, and resonance frequencies of a spherical gas bubble. *The Journal of the Acoustical Society of America*, 130(5):3184, November 2011.
- [28] Guillaume Renaud, Johan G Bosch, Antonius F W Van Der Steen, and Nico De Jong. Low-Amplitude Non-linear Volume Vibrations of Single Microbubbles Measured with an "Acoustical Camera". *Ultrasound in medicine & biology*, 40(6):1282–1295, March 2014.
- [29] D H Simpson, C T Chin, and P N Burns. Pulse inversion Doppler: a new method for detecting nonlinear echoes from microbubble contrast agents. *IEEE transactions on ultrasonics, ferroelectrics, and frequency control*, 46(2):372–82, January 1999.
- [30] P.J. Phillips. Contrast pulse sequences (CPS): imaging nonlinear microbubbles. In *2001 IEEE Ultrasonics Symposium*, volume 2, pages 1739–1745. IEEE, 2001.
- [31] John R Eisenbrey, Jaydev K Dave, Daniel a Merton, Juan P Palazzo, Anne L Hall, and Flemming Forsberg. Parametric imaging using subharmonic signals from ultrasound contrast agents in patients with breast lesions. *Journal of ultrasound in medicine : official journal of the American Institute of Ultrasound in Medicine*, 30(1):85–92, January 2011.
- [32] Flemming Forsberg, Ji-Bin Liu, William T Shi, Raymond Ro, Kathryn J Lipcan, Xuedong Deng, and Anne L Hall. In vivo perfusion estimation using subharmonic contrast microbubble signals. *Journal of ultrasound in medicine : official journal of the American Institute of Ultrasound in Medicine*, 25(1):15–21, January 2006.
- [33] Raffi Karshafian, Peter N Burns, and Mark R Henkelman. Transit time kinetics in ordered and disordered vascular trees. *Physics in medicine and biology*, 48(19):3225–37, October 2003.
- [34] Marianne Gauthier, Farid Tabarout, Ingrid Leguerney, Mélanie Polrot, Stéphanie Pitre, Pierre Peronneau, and Nathalie Lassau. Assessment of Quantitative Perfusion Parameters by Dynamic Contrast-Enhanced Sonography Using a Deconvolution Method. *Journal of ultrasound in Medicine*, pages 595–608, 2012.
- [35] Pai-Chi Li and Mei-Ju Yang. Transfer function analysis of ultrasonic time-intensity measurements. *Ultrasound in Medicine & Biology*, 29(10):1493–1500, October 2003.
- [36] Radovan Jirik, Kim Nylund, Odd H Gilja, Martin Mezl, Vratislav Harabis, Radim Kolar, Michal Standara, and Torfinn Taxt. Ultrasound perfusion analysis combining bolus-tracking and burst-replenishment. *IEEE transactions on ultrasonics, ferroelectrics, and frequency control*, 60(2):310–9, February 2013.

- [37] Stéphane Mallat. *A Wavelet Tour of Signal Processing, Third Edition: The Sparse Way*. Academic Press, 3rd edition, 2008.
- [38] N de Jong and L Hoff. Ultrasound scattering properties of Albunex microspheres. *Ultrasonics*, 31(3):175–181, May 1993.
- [39] Marios Lampaskis and Michalakis Averkiou. Investigation of the relationship of nonlinear backscattered ultrasound intensity with microbubble concentration at low MI. *Ultrasound in medicine biology*, 36(2):306–312, 2010.
- [40] Alexandre Dizeux, Thomas Payen, Gisela Lechuga, and S. Lori Bridal. Implementation of a controlled injection system for dynamic contrast-enhanced ultrasonography. In *2012 IEEE International Ultrasonics Symposium*, pages 1–4. IEEE, October 2012.
- [41] Kevin Wei, Ananda R Jayaweera, Soroosh Firoozan, Andre Linka, Danny M Skyba, and S. Kaul. Quantification of Myocardial Blood Flow With Ultrasound-Induced Destruction of Microbubbles Administered as a Constant Venous Infusion. *Circulation*, 97(5):473–483, February 1998.
- [42] Marcel Arditi, Peter J A Frinking, Xiang Zhou, and Nicolas G Rognin. A new formalism for the quantification of tissue perfusion by the destruction-replenishment method in contrast ultrasound imaging. *IEEE transactions on ultrasonics, ferroelectrics, and frequency control*, 53(6):1118–29, June 2006.
- [43] P J Colon, D R Richards, C a Moreno, J P Murgo, and J Cheirif. Benefits of reducing the cardiac cycle-triggering frequency of ultrasound imaging to increase myocardial opacification with FSO69 during fundamental and second harmonic imaging. *Journal of the American Society of Echocardiography : official publication of the American Society of Echocardiography*, 10(6):602–7, 1997.
- [44] Dilantha B Ellegala, Howard Leong-Poi, Joan E Carpenter, Alexander L Klibanov, Sanjiv Kaul, Mark E Shaffrey, Jiri Sklenar, and Jonathan R Lindner. Imaging tumor angiogenesis with contrast ultrasound and microbubbles targeted to alpha(v)beta3. *Circulation*, 108(3):336–41, July 2003.
- [45] J. Eyding. Contrast Burst Depletion Imaging (CODIM): A New Imaging Procedure and Analysis Method for Semiquantitative Ultrasonic Perfusion Imaging. *Stroke*, 34(1):77–83, December 2002.
- [46] Thomas P Gauthier, Mohamed Chebil, Pierre Peronneau, and Nathalie Lassau. In vitro evaluation of the impact of ultrasound scanner settings and contrast bolus volume on time-intensity curves. *Ultrasonics*, 52(1):12–9, January 2012.
- [47] E. Stride, M-X. Tang, and R.J. Eckersley. Physical phenomena affecting quantitative imaging of ultrasound contrast agents. *Applied Acoustics*, 70(10):1352–1362, October 2009.
- [48] Thomas P Gauthier, Michalakis Averkiou, and Edward L S Leen. Perfusion quantification using dynamic contrast-enhanced ultrasound: the impact of dynamic range and gain on time-intensity curves. *Ultrasonics*, 51(1):102–6, January 2011.

- [49] Nathalie Lassau, Linda Chami, Baya Benatsou, Pierre Peronneau, and Alain Roche. Dynamic contrast-enhanced ultrasonography (DCE-US) with quantification of tumor perfusion: a new diagnostic tool to evaluate the early effects of antiangiogenic treatment. *European Radiology*, 17 Suppl 6(S6):F89–F98, 2007.
- [50] Thomas Payen, Alain Coron, Michele Lamuraglia, Delphine Le Guillou-Buffello, Emmanuel Gaud, Marcel Arditi, Olivier Lucidarme, and S Lori Bridal. Echo-power estimation from log-compressed video data in dynamic contrast-enhanced ultrasound imaging. *Ultrasound in medicine & biology*, 39(10):1826–37, October 2013.
- [51] Meng-Xing Tang, Jean-Martial Mari, Peter N T Wells, and Robert J Eckersley. Attenuation correction in ultrasound contrast agent imaging: elementary theory and preliminary experimental evaluation. *Ultrasound in medicine & biology*, 34(12):1998–2008, December 2008.
- [52] Sébastien Mulé, Alain De Cesare, Olivier Lucidarme, Frédérique Frouin, and Alain Herment. Regularized estimation of contrast agent attenuation to improve the imaging of microbubbles in small animal studies. *Ultrasound in medicine & biology*, 34(6):938–48, June 2008.
- [53] Sébastien Mulé, Nadja Kachenoura, Olivier Lucidarme, A De Oliveira, Claire Pellot-Barakat, A Herment, and F Frouin. An automatic respiratory gating method for the improvement of microcirculation evaluation: application to contrast-enhanced ultrasound studies of focal liver lesions. *Physics in medicine and biology*, 56(16):5153–65, August 2011.
- [54] Damianos Christofides, Student Member, and Edward Leen. Automatic Respiratory Gating for Contrast Ultrasound Evaluation of Liver Lesions. *IEEE transactions on ultrasonics, ferroelectrics, and frequency control*, 61(1):25–32, 2014.
- [55] Nicolas Rognin, R Campos, J P Thiran, T Messenger, A Broillet, P Frinking, L Mercier, and Marcel Arditi. A new approach for automatic motion compensation for improved estimation of perfusion quantification parameters in ultrasound imaging. In *Proc 8th French Conf Acoustics*, pages 61–65. Société Française d’Acoustique, 2006.
- [56] Ji Zhang, Mingyue Ding, Fan Meng, and Xuming Zhang. Quantitative evaluation of two-factor analysis applied to hepatic perfusion study using contrast-enhanced ultrasound. *IEEE transactions on bio-medical engineering*, 60(2):259–67, February 2013.
- [57] Nizar Bouhleb, Alain Coron, Guillaume Barrois, Olivier Lucidarme, and S. Lori Bridal. Dual-mode registration of dynamic contrast-enhanced ultrasound combining tissue and contrast sequences. *Ultrasonics*, pages 1–11, January 2014.
- [58] Paul Kogan, Kennita a Johnson, Steven Feingold, Nicholas Garrett, Ismayil Guracar, William J Arendshorst, and Paul a Dayton. Validation of dynamic contrast-enhanced ultrasound in rodent kidneys as an absolute quantitative method for measuring blood perfusion. *Ultrasound in medicine & biology*, 37(6):900–8, June 2011.
- [59] Aymeric Guibal, Thibaud Lefort, Laurence Chardon, Noura Benslama, Sébastien Mulé, Franck Pilleul, Catherine Lombard-Bohas, Lori Bridal, Jean Alain Chayvialle, Olivier Lucidarme, Alban

- Denys, and Thomas Walter. Contrast-enhanced ultrasound after devascularisation of neuroendocrine liver metastases: functional and morphological evaluation. *European radiology*, 23(3):805–15, March 2013.
- [60] Martin E Eichhorn, Laura V Klotz, Siiri Luedemann, Sebastian Strieth, Axel Kleespies, Gerhard Preissler, Michael Lindner, Karl-walter Jauch, Maximilian F Reiser, and Dirk-aandre Clevert. Non-invasive contrast enhanced ultrasound for quantitative assessment of tumor microcirculation Vascular targeting tumor therapy. 9(10):794–802, 2010.
- [61] M Mischi, J a den Boer, and H H M Korsten. On the physical and stochastic representation of an indicator dilution curve as a gamma variate. *Physiological measurement*, 29(3):281–94, March 2008.
- [62] SCHLOSSM.EJ, WEINSTEI.H, S LOCHAYA, and A B SHAFFER. PERFECT MIXERS IN SERIES MODEL FOR FITTING VENOARTERIAL INDICATOR-DILUTION CURVES. *JOURNAL OF APPLIED PHYSIOLOGY*, 22(2):327–&, 1967.
- [63] Johan M Thijssen and Chris L de Korte. Modeling ultrasound contrast measurement of blood flow and perfusion in biological tissue. *Ultrasound in medicine & biology*, 31(2):279–85, February 2005.
- [64] Martin Krix, Fabian Kiessling, Nabeel Farhan, Kerstin Schmidt, Johannes Hoffend, and Stefan Delorme. A multivessel model describing replenishment kinetics of ultrasound contrast agent for quantification of tissue perfusion. *Ultrasound in Medicine & Biology*, 29(10):1421–1430, October 2003.
- [65] John M Hudson, Raffi Karshafian, and Peter N Burns. Quantification of flow using ultrasound and microbubbles: a disruption replenishment model based on physical principles. *Ultrasound in Medicine & Biology*, 35(12):2007–20, December 2009.
- [66] John M Hudson, Ross Williams, Brendan Lloyd, Mostafa Atri, Tae Kyoung Kim, Georg Bjarnason, and Peter N Burns. Improved flow measurement using microbubble contrast agents and disruption-replenishment: clinical application to tumour monitoring. *Ultrasound in medicine & biology*, 37(8):1210–21, August 2011.
- [67] Michalakis Averkiou, Marios Lampaskis, Konstantina Kyriakopoulou, Dimosthenis Skarlos, Georgios Klouvas, Costas Strouthos, and Edward Leen. Quantification of tumor microvasculature with respiratory gated contrast enhanced ultrasound for monitoring therapy. *Ultrasound in medicine & biology*, 36(1):68–77, January 2010.
- [68] Guillaume Barrois, Alain Coron, Thomas Payen, Alexandre Dizeux, and Lori Bridal. A multiplicative model for improving microvascular flow estimation in dynamic contrast-enhanced ultrasound (DCE-US): theory and experimental validation. *IEEE transactions on ultrasonics, ferroelectrics, and frequency control*, 60(11):2284–94, November 2013.
- [69] Nicolas G. Rognin, Marcel Arditi, Laurent Mercier, Peter J A Frinking, Michel Schneider, Geneviève Perrenoud, Anass Anaye, Jean-Yves Meuwly, and François Tranquart. Parametric imaging for characterizing focal liver lesions in contrast-enhanced ultrasound. *IEEE transactions on ultrasonics, ferroelectrics, and frequency control*, 57(11):2503–11, November 2010.

- [70] Massimo Mischi, Ton a Kalker, and Erik H Korsten. Contrast echocardiography for pulmonary blood volume quantification. *IEEE transactions on ultrasonics, ferroelectrics, and frequency control*, 51(9):1137–47, September 2004.
- [71] Massimo Mischi, Maarten P J Kuenen, and Hessel Wijkstra. Angiogenesis imaging by spatiotemporal analysis of ultrasound contrast agent dispersion kinetics. *IEEE transactions on ultrasonics, ferroelectrics, and frequency control*, 59(4):621–9, April 2012.
- [72] Rachel E Pollard, Paul a Dayton, Katherine D Watson, Xiaowen Hu, Ismayil M Guracar, and Katherine W Ferrara. Motion corrected cadence CPS ultrasound for quantifying response to vasoactive drugs in a rat kidney model. *Urology*, 74(3):675–81, September 2009.
- [73] Moritz Palmowski, Wiltrud Lederle, Jessica Gaetjens, Michaela Socher, Peter Hauff, Jessica Bzyl, Wolfhard Semmler, Rolf W Günther, and Fabian Kiessling. Comparison of conventional time-intensity curves vs. maximum intensity over time for post-processing of dynamic contrast-enhanced ultrasound. *European journal of radiology*, 75(1):e149–53, July 2010.
- [74] John R Eisenbrey, Christian C Wilson, Raymond J Ro, Traci B Fox, Ji-Bin Liu, See-Ying Chiou, and Flemming Forsberg. Correlation of ultrasound contrast agent derived blood flow parameters with immunohistochemical angiogenesis markers in murine xenograft tumor models. *Ultrasonics*, 53(7):1384–91, September 2013.
- [75] Robert J Eckersley, J P Michiel Sedelaar, Martin J K Blomley, Hessel Wijkstra, Nandita M DeSouza, David O Cosgrove, and Jean J M C H de la Rosette. Quantitative microbubble enhanced transrectal ultrasound as a tool for monitoring hormonal treatment of prostate carcinoma. *The Prostate*, 51(4):256–67, June 2002.
- [76] Casey N Ta, Yuko Kono, Christopher V Barback, Robert F Mattrey, and Andrew C Kummel. Automating tumor classification with pixel-by-pixel contrast-enhanced ultrasound perfusion kinetics. *Journal of vacuum science and technology. B, Nanotechnology & microelectronics : materials, processing, measurement, & phenomena : JVST B*, 30(2):2C103, March 2012.
- [77] Maarten P J Kuenen, Tamerlan a Saidov, Hessel Wijkstra, Jean J M C H de la Rosette, and Massimo Mischi. Spatiotemporal correlation of ultrasound contrast agent dilution curves for angiogenesis localization by dispersion imaging. *IEEE transactions on ultrasonics, ferroelectrics, and frequency control*, 60(12):2665–9, December 2013.
- [78] Stephan Kersting, Ralf Konopke, Florina Kersting, Andreas Volk, Marius Distler, Hendrik Bergert, Hans-Detlev Saeger, Robert Grützmann, and Alfred Bunk. Quantitative perfusion analysis of transabdominal contrast-enhanced ultrasonography of pancreatic masses and carcinomas. *Gastroenterology*, 137(6):1903–11, December 2009.
- [79] Ross Williams, JM Hudson, and BA Lloyd. Dynamic Microbubble Contrast-enhanced US to measure tumor response to targeted therapy: a proposed clinical protocol with results from renal cell carcinoma patients receiving antiangiogenic therapy. *Radiology*, 260(2), 2011.
- [80] Michele Lamuraglia, S Lori Bridal, Mathieu Santin, Gianni Izzi, Olivier Rixe, Angelo Paradiso, and Olivier Lucidarme. Clinical relevance of contrast-enhanced ultrasound in monitoring anti-angiogenic

- therapy of cancer: current status and perspectives. *Critical reviews in oncology/hematology*, 73(3):202–12, March 2010.
- [81] AR Broumas and RE Pollard. Contrast-Enhanced Computed Tomography and Ultrasound for the Evaluation of Tumor Blood Flow. *Investigative radiology*, 40(3):134–147, 2005.
- [82] Costas Strouthos, Marios Lampaskis, Vassilis Sboros, Alan McNeilly, and Michalakis Averkiou. Indicator dilution models for the quantification of microvascular blood flow with bolus administration of ultrasound contrast agents. *IEEE transactions on ultrasonics, ferroelectrics, and frequency control*, 57(6):1296–310, June 2010.
- [83] Maarten Kuenen, Ingeborg Herold, Hendrikus Korsten, Jean de la Rosette, H Wijkstra, and Massimo Mischi. Maximum-likelihood estimation for indicator dilution analysis. *IEEE transactions on bio-medical engineering*, (c):1–11, November 2013.
- [84] G N Stewart. Reasearches on the circulation time and on the influences which affect it. *The Journal of physiology*, 22(3):159–83, November 1897.
- [85] WF Hamilton, JW Moore, and JM Kinsman. Studies on the Circulation. *American Journal of Physiology*, pages 534–551, 1932.
- [86] John M Hudson, Kogee Leung, and Peter N Burns. The Lognormal Perfusion Model for Disruption Replenishment Measurements of Blood Flow: In Vivo Validation. *Ultrasound in medicine & biology*, 37(10):1571–1578, August 2011.
- [87] Jonathan Casey, Charles Sennoga, Helen Mulvana, Jo V Hajnal, Meng-Xing Tang, and Robert J Eckersley. Single bubble acoustic characterization and stability measurement of adherent microbubbles. *Ultrasound in medicine & biology*, 39(5):903–14, May 2013.
- [88] Trevor Hastie, Robert Tibshirani, and Friedman Jerome. *The Elements of Statistical Learning*. Springer Series in Statistics. Springer New York, New York, NY, 2009.
- [89] Christoph B. Burekhardt. Speckle in ultrasound B-mode scans. *IEEE transactions on Sonics and Ultrasonics*, 25(1):1–6, January 1978.
- [90] R.F. Wagner, S.W. Smith, J.M. Sandrik, and H. Lopez. Statistics of Speckle in Ultrasound B-Scans. *IEEE transactions on Sonics and Ultrasonics*, 30(3):156–163, 1983.
- [91] François Destrempes and Guy Cloutier. A critical review and uniformized representation of statistical distributions modeling the ultrasound echo envelope. *Ultrasound in medicine & biology*, 36(7):1037–51, July 2010.
- [92] Maarten P J Kuenen, Massimo Mischi, and Hessel Wijkstra. Contrast-ultrasound diffusion imaging for localization of prostate cancer. *IEEE transactions on medical imaging*, 30(8):1493–502, August 2011.
- [93] L. Devroye. *Non-uniform random variate generation*. Springer-Verlag, 1986.

- [94] N. Lassau, V. Vilgrain, M. Kind, J. Lacroix, M. Cuinet, R. Aziza, S. Taieb, a. Sarran, C. Labbe, and S. Koscielny. 805 ORAL Evaluation of Anti-angiogenic Treatments With DCE-US in 539 Patients – Results After 2 Years Median Follow-up. *European Journal of Cancer*, 47:S96, September 2011.
- [95] K Q Schwarz, X Chen, G P Bezante, D Phillips, and R Schlief. The Doppler kinetics of microbubble echo contrast. *Ultrasound in medicine & biology*, 22(4):453–62, January 1996.
- [96] Guillaume Barrois, Alain Coron, and Lori Bridal. Simulation of dynamic contrast-enhanced ultrasound sequences using example-based texture generation. *Irbm*, 2014.
- [97] JA Jensen and NB Svendsen. Calculation of Pressure Fields from Arbitrarily Shaped, Apodized and Excited Ultrasound Transducers. *IEEE transactions on ultrasonics, ferroelectrics, and frequency control*, 39(2):262–267, 1992.
- [98] François Varray, Olivier Basset, Piero Tortoli, and Christian Cachard. CREANUIS: A Non-linear Radiofrequency Ultrasound Image Simulator. *Ultrasound in medicine & biology*, 39(10):1915–24, October 2013.
- [99] Xinguo Liu, Yaohua Hu, Jingdan Zhang, Xin Tong, Baining Guo, and Heung-Yeung Shum. Synthesis and rendering of bidirectional texture functions on arbitrary surfaces. *IEEE transactions on visualization and computer graphics*, 10(3):278–89, 2002.
- [100] G Renault, F Tranquart, V Perlberg, a Bleuzen, a Herment, and F Frouin. A posteriori respiratory gating in contrast ultrasound for assessment of hepatic perfusion. *Physics in medicine and biology*, 50(19):4465–80, October 2005.
- [101] Anirban DasGupta. *Probability for Statistics and Machine Learning*. Springer Texts in Statistics. Springer New York, New York, NY, 2011.
- [102] LY Wei, S Lefebvre, V Kwatra, and Greg Turk. State of the art in example-based texture synthesis. *Eurographics 2009*, (Section 2), 2009.
- [103] François Varray, Alessandro Ramalli, Christian Cachard, Piero Tortoli, and Olivier Basset. Fundamental and second-harmonic ultrasound field computation of inhomogeneous nonlinear medium with a generalized angular spectrum method. *IEEE transactions on ultrasonics, ferroelectrics, and frequency control*, 58(7):1366–76, July 2011.
- [104] Manav Bhushan, Julia a Schnabel, Laurent Risser, Mattias P Heinrich, J Michael Brady, and Mark Jenkinson. Motion correction and parameter estimation in dceMRI sequences: application to colorectal cancer. *Medical image computing and computer-assisted intervention : MICCAI ... International Conference on Medical Image Computing and Computer-Assisted Intervention*, 14(Pt 1):476–83, January 2011.
- [105] Ganesh Adluru, Edward V R DiBella, and Matthias C Schabel. Model-based registration for dynamic cardiac perfusion MRI. *Journal of magnetic resonance imaging : JMRI*, 24(5):1062–70, November 2006.

- [106] Giovanni a Buonaccorsi, James P B O'Connor, Angela Caunce, Caleb Roberts, Sue Cheung, Yvonne Watson, Karen Davies, Lynn Hope, Alan Jackson, Gordon C Jayson, and Geoffrey J M Parker. Tracer kinetic model-driven registration for dynamic contrast-enhanced MRI time-series data. *Magnetic resonance in medicine : official journal of the Society of Magnetic Resonance in Medicine / Society of Magnetic Resonance in Medicine*, 58(5):1010–9, November 2007.
- [107] Josien P W Pluim, J B Antoine Maintz, and Max A Viergever. Mutual-Information-Based Registration of Medical Images : A Survey. *IEEE transactions on medical imaging*, 22(8):986–1004, 2003.
- [108] MPJ Kuenen, TA Saidov, Hessel Wijkstra, and Massimo Mischi. Contrast-Ultrasound Dispersion Imaging for Prostate Cancer Localization by Improved Spatiotemporal Similarity Analysis. *Ultrasound in Medicine & ...*, pages 1–11, 2013.
- [109] Stefan Klein, Marius Staring, Keelin Murphy, Max A Viergever, and Josien P W Pluim. elastix : A Toolbox for Intensity-Based Medical Image Registration. *Framework*, 29(1):196–205, 2010.
- [110] F Maes, a Collignon, D Vandermeulen, G Marchal, and P Suetens. Multimodality image registration by maximization of mutual information. *IEEE transactions on medical imaging*, 16(2):187–98, April 1997.
- [111] Kyrre E Emblem, Kim Mouridsen, Atle Bjornerud, Christian T Farrar, Dominique Jennings, Ronald J H Borra, Patrick Y Wen, Percy Ivy, Tracy T Batchelor, Bruce R Rosen, Rakesh K Jain, and a Gregory Sorensen. Vessel architectural imaging identifies cancer patient responders to anti-angiogenic therapy. *Nature medicine*, 19(9):1178–1183, August 2013.
- [112] Nathalie Lassau, Mohamed Chebil, Linda Chami, Sophie Bidault, Elizabeth Girard, and Alain Roche. Dynamic contrast-enhanced ultrasonography (DCE-US): a new tool for the early evaluation of antiangiogenic treatment. *Targeted oncology*, 5(1):53–8, March 2010.
- [113] Susanne M Stieger, Susannah H Bloch, Oded Foreman, Erik R Wisner, Katherine W Ferrara, and Paul a Dayton. Ultrasound assessment of angiogenesis in a matrigel model in rats. *Ultrasound in medicine & biology*, 32(5):673–81, May 2006.
- [114] H.P. Ng, S.H. Ong, K.W.C. Foong, P.S. Goh, and W.L. Nowinski. Medical Image Segmentation Using K-Means Clustering and Improved Watershed Algorithm. *2006 IEEE Southwest Symposium on Image Analysis and Interpretation*, pages 61–65, 2006.
- [115] G J Lueck, T K Kim, P N Burns, and a L Martel. Hepatic perfusion imaging using factor analysis of contrast enhanced ultrasound. *IEEE transactions on medical imaging*, 27(10):1449–57, October 2008.
- [116] S H Lee, J H Kim, K G Kim, J S Park, S J Park, and W K Moon. Optimal clustering of kinetic patterns on malignant breast lesions: comparison between K-means clustering and three-time-points method in dynamic contrast-enhanced MRI. *Conference proceedings : ... Annual International Conference of the IEEE Engineering in Medicine and Biology Society. IEEE Engineering in Medicine and Biology Society. Conference*, 2007:2089–93, January 2007.

- [117] VG Spokoiny. Adaptive hypothesis testing using wavelets. *The Annals of Statistics*, (April):2477–2498, 1996.
- [118] Y Baraud, S Huet, and B Laurent. Adaptive tests of Linear Hypotheses by Model Selection. *Annals of statistics*, 31(1):225–251, 2003.
- [119] C Durot and Y Iner. An adaptive test for zero mean. *Mathematical Methods of . . .*, 15(1):26–60, 2006.
- [120] P. Frinking, M. Arditì, and N. Rognin. System for extracting morphological information through a perfusion assessment process, June 28 2006. EP Patent App. EP20,040,106,952.
- [121] M. Bruce, J. Powers, R. Garg, D. Skyba, and M. Averkiou. Ultrasonic diagnostic imaging system and method for detecting lesions of the liver, August 31 2006. WO Patent App. PCT/IB2006/050,512.
- [122] Marianne Gauthier, Farid Tabarout, Ingrid Leguerney, Mélanie Polrot, Stéphanie Pitre, Pierre Peronneau, and Nathalie Lassau. Assessment of Quantitative Perfusion Parameters by Dynamic Contrast-Enhanced Sonography Using a Deconvolution Method. *Journal of ultrasound in medicine : official journal of the American Institute of Ultrasound in Medicine*, pages 595–608, 2012.
- [123] Olivier Clatz, Maxime Sermesant, Pierre-yves Bondiau, Hervé Delingette, Simon K Warfield, Grégoire Malandain, and Nicholas Ayache. Realistic simulation of the 3-D growth of brain tumors in MR images coupling diffusion with biomechanical deformation. *IEEE transactions on medical imaging*, 24(10):1334–46, October 2005.
- [124] Benjamin Ribba, Emmanuel Watkin, Michel Tod, and Pascal Girard. A model of vascular tumour growth in mice combining longitudinal tumour size data with histological biomarkers. . . . *Journal of Cancer*, 7, 2011.